

JADES Data Release 3 – NIRSpec/MSA spectroscopy for 4,000 galaxies in the GOODS fields

FRANCESCO D'EUGENIO,^{1,2,*} ALEX J. CAMERON,^{3,*} JAN SCHOLTZ,^{1,2,*} STEFANO CARNIANI,^{4,*} CHRIS J. WILLOTT,^{5,*}
EMMA CURTIS-LAKE,⁶ ANDREW J. BUNKER,³ ELEONORA PARLANTI,⁴ ROBERTO MAIOLINO,^{1,2,7}
CHRISTOPHER N. A. WILLMER,⁸ PETER JAKOBSEN,⁹ BRANT E. ROBERTSON,¹⁰ BENJAMIN D. JOHNSON,¹¹
SANDRO TACCHELLA,^{1,2} PHILLIP A. CARGILE,¹¹ TIM RAWLE,¹² SANTIAGO ARRIBAS,¹³ JACOPO CHEVALLARD,³
MIRKO CURTI,¹⁴ EIICHI EGAMI,⁸ DANIEL J. EISENSTEIN,¹¹ NIMISHA KUMARI,¹⁵ TOBIAS J. LOOSER,^{1,2} MARCIA J. RIEKE,⁸
BRUNO RODRÍGUEZ DEL PINO,¹³ AAYUSH SAXENA,^{3,7} HANNAH ÜBLER,^{1,2} GIACOMO VENTURI,⁴ JORIS WITSTOK,^{1,2}
WILLIAM M. BAKER,^{1,2} RACHANA BHATAWDEKAR,¹⁶ NINA BONAVENTURA,¹⁷ KRISTAN BOYETT,^{18,19} STEPHANE CHARLOT,²⁰
A. LOLA DANHAIVE,^{1,2} KEVIN N. HAINLINE,⁸ RYAN HAUSEN,²¹ JAKOB M. HELTON,⁸ XIHAN JI,^{1,2} ZHIYUAN JI,⁸
GARETH C. JONES,³ IGNAS JOUDŽBALIS,^{1,2} MICHAEL V. MASEDA,²² PABLO G. PÉREZ-GONZÁLEZ,¹³ MICHELE PERNA,¹³
DÁVID PUSKÁS,^{1,2} IRENE SHIVAEI,¹³ MADDIE S. SILCOCK,⁶ CHARLOTTE SIMMONDS,^{1,2} RENSKÉ SMIT,²³ FENGWU SUN,⁸
NATALIA C. VILLANUEVA,^{1,2} CHRISTINA C. WILLIAMS,^{24,8} AND YONGDA ZHU⁸

¹*Kavli Institute for Cosmology, University of Cambridge, Madingley Road, Cambridge CB3 0HA, UK*

²*Cavendish Laboratory, University of Cambridge, 19 JJ Thomson Avenue, Cambridge CB3 0HE, UK*

³*Department of Physics, University of Oxford, Denys Wilkinson Building, Keble Road, Oxford OX1 3RH, UK*

⁴*Scuola Normale Superiore, Piazza dei Cavalieri 7, I-56126 Pisa, Italy*

⁵*NRC Herzberg, 5071 West Saanich Rd, Victoria, BC V9E 2E7, Canada*

⁶*Centre for Astrophysics Research, Department of Physics, Astronomy and Mathematics, University of Hertfordshire, Hatfield AL10 9AB, UK*

⁷*Department of Physics and Astronomy, University College London, Gower Street, London WC1E 6BT, UK*

⁸*Steward Observatory, University of Arizona, 933 North Cherry Avenue, Tucson, AZ 85721, USA*

⁹*Cosmic Dawn Center (DAWN), Copenhagen, Denmark 2. Niels Bohr Institute, University of Copenhagen, Jagtvej 128, DK-2200, Copenhagen, Denmark*

¹⁰*Department of Astronomy and Astrophysics, University of California, Santa Cruz, 1156 High Street, Santa Cruz, CA 95064, USA*

¹¹*Center for Astrophysics | Harvard & Smithsonian, 60 Garden St., Cambridge MA 02138 USA*

¹²*European Space Agency (ESA), European Space Astronomy Centre (ESAC), Camino Bajo del Castillo s/n, 28692 Villafranca del Castillo, Madrid, Spain*

¹³*Centro de Astrobiología (CAB), CSIC-INTA, Cra. de Ajalvir Km. 4, 28850- Torrejón de Ardoz, Madrid, Spain*

¹⁴*European Southern Observatory, Karl-Schwarzschild-Strasse 2, 85748 Garching, Germany*

¹⁵*AURA for European Space Agency, Space Telescope Science Institute, 3700 San Martin Drive. Baltimore, MD, 21210*

¹⁶*European Space Agency (ESA), European Space Astronomy Centre (ESAC), Camino Bajo del Castillo s/n, 28692 Villanueva de la Cañada, Madrid, Spain*

¹⁷*Steward Observatory University of Arizona 933 N. Cherry Avenue Tucson AZ 85721, USA*

¹⁸*School of Physics, University of Melbourne, Parkville 3010, VIC, Australia*

¹⁹*ARC Centre of Excellence for All Sky Astrophysics in 3 Dimensions (ASTRO 3D), Australia*

²⁰*Sorbonne Université, CNRS, UMR 7095, Institut d'Astrophysique de Paris, 98 bis bd Arago, 75014 Paris, France*

²¹*Department of Physics and Astronomy, The Johns Hopkins University, 3400 N. Charles St., Baltimore, MD 21218*

²²*Department of Astronomy, University of Wisconsin-Madison, 475 N. Charter St., Madison, WI 53706 USA*

²³*Astrophysics Research Institute, Liverpool John Moores University, 146 Brownlow Hill, Liverpool L3 5RF, UK*

²⁴*NSF's National Optical-Infrared Astronomy Research Laboratory, 950 North Cherry Avenue, Tucson, AZ 85719, USA*

Submitted to ApJS

ABSTRACT

We present the third data release of JADES, the *JWST* Advanced Deep Extragalactic Survey, providing both imaging and spectroscopy in the two GOODS fields. Spectroscopy consists of medium-depth and deep NIRSpec/MSA spectra of 4,000 targets, covering the spectral range 0.6–5.3 μm and observed with both the low-dispersion prism ($R = 30\text{--}300$) and all three medium-resolution gratings

($R = 500\text{--}1,500$). We describe the observations, data reduction, sample selection, and target allocation. We measured 2,375 redshifts (2,053 from multiple emission lines); our targets span the range from $z = 0.5$ up to $z = 13$, including 404 at $z > 5$. The data release includes 2-d and 1-d fully reduced spectra, with slit-loss corrections and background subtraction optimized for point sources. We also provide redshifts and $S/N > 5$ emission-line flux catalogs for the prism and grating spectra, and concise guidelines on how to use these data products. Alongside spectroscopy, we are also publishing fully calibrated NIRC*am* imaging, which enables studying the JADES sample with the combined power of imaging and spectroscopy. Together, these data provide the largest statistical sample to date to characterize the properties of galaxy populations in the first billion years after the Big Bang.

1. INTRODUCTION

The long-awaited launch of *JWST* has revolutionized our ability to observe the early universe. Already in the first two years of operations, *JWST* enabled an amazing number of discoveries and studies. Many of these breakthroughs have been made possible by the unprecedented sensitivity and wavelength coverage of the NIRSpec instrument (Jakobsen et al. 2022). These include the spectroscopic confirmation of galaxies beyond redshift $z = 10$ (Curtis-Lake et al. 2023; Arrabal Haro et al. 2023; Wang et al. 2023) – including through emission lines (Bunker et al. 2023a); the discovery of substantial neutral-gas absorption in galaxies at $z = 9\text{--}11$ (e.g., Heintz et al. 2023; Umeda et al. 2023); the first studies of metallicity and chemical abundances using well-known optical lines (e.g., Curti et al. 2023a; Nakajima et al. 2023); the discovery of massive, quiescent and old galaxies at $z = 3\text{--}5$ (e.g., Carnall et al. 2023; Glazebrook et al. 2023); the first ‘mini-quenched’ galaxies (Looser et al. 2023a; Strait et al. 2023); neutral-phase outflows in massive quiescent galaxies (Belli et al. 2023; D’Eugenio et al. 2023a; Davies et al. 2024); the discovery of bright, metal-poor active galactic nuclei (e.g., Kocevski et al. 2023; Übler et al. 2023); the most distant active galactic nuclei (AGN; Maiolino et al. 2023a; Goulding et al. 2023); and even tentative evidence of the first generation of stars (Maiolino et al. 2023b).

However, for spectroscopy, sample sizes are still small, of the order of tens to one hundred objects (Looser et al. 2023b; Curti et al. 2023b; Nakajima et al. 2023). The availability of large samples is key to characterizing the properties of galaxy populations, studying their cosmic evolution, and disentangling the intricate pattern of cause and effect between the observed properties of galaxies. Studies of galaxies at redshifts $z < 1$ rely on thousands or even hundreds of thousands of spectroscopic targets (e.g., Abazajian et al. 2009; Driver et al. 2018; DESI Collaboration et al. 2016). By studying several physical properties at a time (e.g., Kauff-

mann et al. 2003a,b; Peng et al. 2010; Graves & Faber 2010), or by using machine-learning techniques (e.g., Bluck et al. 2022; Baker et al. 2022; Barsanti et al. 2023; Walmsley et al. 2023), these studies have made tremendous progress in understanding the links between many galaxy properties like morphology, star-formation rate, age, gas fraction, star-formation efficiency, super-massive black-hole mass, local and global environment, and metallicity. In the last decades, large spectroscopic surveys in the near-infrared have enabled the study of hundreds of galaxies at redshifts $z = 1\text{--}4$ (e.g., Wisnioski et al. 2015; Stott et al. 2016; Kriek et al. 2015). In the near future, new surveys will observe even more galaxies at redshifts $z \lesssim 4$ (Dalton et al. 2012; Tamura et al. 2016; de Jong et al. 2019; Maiolino et al. 2020). However – at least for the next decade – nothing other than *JWST* and, in particular, NIRSpec will be able to obtain deep rest-frame optical spectroscopy for large samples of galaxies at redshifts 3–10, the crucial early phases of galaxy formation.

The NIRSpec Micro Shutter Assembly (MSA, Ferruit et al. 2022) was designed to observe more than one hundred targets simultaneously, and is now the highest-multiplicity slit-based spectrograph in the near-infrared. In the NIRSpec/MSA, this high multiplicity marries an unprecedented combination of large collecting area, low background, and long wavelength coverage, which all together enable us, for the first time, to efficiently observe large samples of galaxies at redshifts $z > 4$, covering their strongest rest-frame optical features (e.g., Treu et al. 2022, Bezanson et al. 2022, Fujimoto et al. 2023, Oesch et al. 2023a, Bunker et al. 2023b, hereafter: B23).

One of the goals of JADES, the *JWST* Advanced Deep Extragalactic Survey (Eisenstein et al. 2023a), is to observe a statistical sample of galaxies at redshifts $z > 3$, thus enabling spectroscopic studies to move from the ‘discovery’ stage to a more quantitative understanding of galaxy populations. To enable this progress, JADES – a collaboration between the *JWST* NIRC*am* and NIRSpec GTO teams – was designed to fully exploit the synergy between photometry and spectroscopy. The JADES strategy divides the survey time between two

* These authors contributed equally to this work

tiers: medium-depth and deep observations (for the least deep and widest tier of the NIRSpec GTO see [Maseda et al. 2024](#)). All observations are in the two GOODS fields (Great Observatories Origins Deep Survey; [Giavalisco et al. 2004](#)), but the medium tier is divided between the GOODS South and North fields (hereafter, GOODS-S and GOODS-N), whereas the deep tier is in GOODS-S only.

In this article, we present NIRSpec observations of the deep tier from the JADES Origins Field ([Eisenstein et al. 2023b](#)), as well as medium-depth spectra from both GOODS-S and GOODS-N. We provide fully reduced and calibrated 1-d and 2-d spectra, as well as measurements of redshift and emission-line fluxes¹. The NIRSpec data presented here cover all JADES observations up to October 2023; spectroscopic data collected from November 2023 will be the subject of a future data release. In support of this spectroscopy, we also present previously unpublished NIRCам imaging in GOODS-N, including photometric catalogs and photometric redshifts. After presenting the new NIRCам data (Section 2), we move to spectroscopy with a summary of the NIRSpec observations and sample selection (Sections 3 and 4) and of the data reduction (Section 5). We then outline the measurements of spectroscopic redshifts and line fluxes (Sections 6–8). In Sections 9 and 10 we present an assessment of the data products and guidelines for their use, and in Section 11 we showcase exciting highlights from the current data. We conclude with a short summary and brief outlook (Section 12).

Note that the current data release employs the same data reduction as the previous NIRSpec data release (DR1; [B23](#)), with the only difference being a different algorithm for the measurement of emission-line fluxes. This is the third JADES data release (hereafter: DR3), but only the second data release for spectroscopy; JADES DR2 included only NIRCам imaging. Throughout this work, we use the AB magnitude system ([Oke & Gunn 1983](#)).

2. RELEASE OF NIRCAM IMAGING IN GOODS-N

GOODS-N is a very important deep field, as it includes the iconic Hubble Deep Field (HDF; [Williams et al. 1996](#)) and the many other programs that followed in and around it. Of particular note are the substantial HST optical and near-infrared imaging from GOODS ([Giavalisco et al. 2004](#)) and CANDELS ([Grogin et al. 2011](#); [Koekemoer et al. 2011](#)), very deep X-ray imaging from Chandra ([Alexander et al. 2003](#); [Xue et al.](#)

[2016](#)), sub/millimeter observations ([Chapin et al. 2009](#); [Mullaney et al. 2012](#); [Magnelli et al. 2013](#); [Cowie et al. 2017](#)), and broad-band radio coverage ([Morrison et al. 2010](#); [Murphy et al. 2017](#)). This region also has extensive ground-based spectroscopy (e.g., [Wirth et al. 2004](#); [Treu et al. 2005](#); [Newman et al. 2013](#); [Kriek et al. 2015](#)), HST grism spectroscopy ([Momcheva et al. 2016](#)), and hosts other JWST NIRSpec programs such as AURORA (Program ID, PID 1914; [Shapley et al. 2021](#)).

As a part of JADES DR3, we are including images and catalogs from the NIRCам imaging in GOODS-N, observed as the Medium Prime part of JWST program 1181 (PI: Eisenstein). These data were observed in February 2023 and include 7 overlapping medium-deep pointings, each with 8-9 separate filters. Four of the pointings are mildly deeper than the other three; details are in [Eisenstein et al. \(2023a\)](#). The imaging data are supplemented with F182M, F210M, and shallow F444W imaging from the FRESCO survey ([Oesch et al. 2023b](#)).

The reduction of these images follows closely the processing used for JADES DR1 ([Rieke et al. 2023a](#)) and DR2 ([Eisenstein et al. 2023b](#)). For the photometric catalog release, we follow the methods described in [Rieke et al. \(2023a\)](#), [Eisenstein et al. \(2023b\)](#), and [Robertson et al. \(2023a\)](#). These methods were engineered on the deeper JADES GOODS-S imaging. To remove some spurious extended low surface brightness sources, we conservatively remove objects with an average surface brightness of $SB < 0.045$ nJy per pixel within the detection segmentation. Beyond this revision, the techniques follow exactly [Robertson et al. \(2023a\)](#) and will be described in more detail in Robertson et al. (in prep.). As before, the JADES GOODS-N release includes mosaic imaging in all bands, object detection and photometric catalogs from the JADES reduction pipelines, and photometric redshifts determined using EAZY ([Brammer et al. 2008](#)). An interactive FITSMAP ([Hausen & Robertson 2022](#)) website displaying the images, catalogs, and NIRSpec slit overlays and extracted spectra is available via <https://jades-survey.github.io/viewer/>. Figure 1 shows the extent of the JADES NIRCам imaging in the release, visualized as a red-green-blue false-color image using F444W, F200W, and F090W, respectively. To provide a sense of the depth of the image, which reaches ~ 30 mag in some JADES filters, we show in Figure 2 the JADES NIRCам F444W/F200W/F090W image of the Hubble Deep Field footprint. This image highlights the advance of JWST in sensitivity and resolution, providing a deep near-infrared view of the iconic Hubble Deep Field.

In total, this JADES release covers 56 arcmin² of NIRCам imaging in GOODS-N, detecting 85709 distinct

¹ Available on the JADES website <https://jades-survey.github.io/scientists/data.html>.

objects. A summary of the area, median depths, and median exposure times in each filter are provided in Table 1. Maps of the local $5\text{-}\sigma$ point-source, aperture-corrected depths measured in circular apertures of radius $r = 0.15$ arcsec are shown for each filter in Figure 3, along with the location of the HDF footprint for reference.

In releasing the JADES NIRSpec spectroscopic and NIRCcam imaging data jointly, we note the unique synergy between these JWST datasets. Beyond the scientific synergies, the NIRCcam data complement the NIRSpec data by providing targets, enabling consistency checks on the flux calibration of NIRSpec spectral modes, improved slit-loss corrections by providing information on source morphologies, and providing important checks on possible slit contamination by faint sources proximate to the primary NIRSpec targets. The design and execution of the NIRSpec spectroscopic surveys benefit from deep NIRCcam imaging, and co-spatial NIRCcam imaging data enhance the science return of complex NIRSpec MSA campaigns.

3. NIRSPEC/MSA OBSERVATIONS

All observations used NIRSpec in Multi-Object Spectroscopy mode, with the NIRSpec/MSA (Ferruit et al. 2022). The MSA configurations were planned as described in Section 4 using the strategy detailed in Eisenstein et al. (2023a). For each visit, a set of target acquisition (TA) objects (stars and compact galaxies) were identified on the same images as those used for measuring the positions of the science targets. All TA objects were visually inspected to ensure they were compact, symmetric, and did not have color gradients or nearby sources. All TAs used the NIRSpec CLEAR filter and longest readout time (mode NRSRAPIDD6) because the GOODS fields only contain faint TA objects. Further details on the TA setups are provided in Eisenstein et al. (2023a). All 35 TAs performed for JADES so far have been successful.

There were some technical issues with JADES NIRSpec observations that resulted in visits being skipped or having only partial data collection. The two sources of these issues are guide-star acquisition or re-acquisition failures from the Fine Guidance Sensor and ‘shorts’ (electrical short circuits with the NIRSpec MSA; Rawle et al. 2022). For cases where observations of a MSA configuration were partially successful, our strategy is to return with the same MSA configuration one year later to complete the data acquisition on the same targets. For cases where no data were obtained for a MSA

configuration, we have replanned at either the same or at a different orientation.

Table 2 gives a summary of all JADES NIRSpec observations, including the typical integration time (we provide the minimum, mean and maximum integration time for each spectral configuration). In the following subsections, we provide an outline of the observations that are the subject of this data release. The DR3 electronic files provide more details such as observation date and actual integration times per target. We generally describe the observations with a label structured as ‘depth/selection’, where depth is either ‘Medium’, ‘Deep’, or ‘Ultradeep’, and selection is either ‘HST’ or ‘JWST’, depending on how the majority of targets was selected; these labels are then ‘translated’ into the TIER column in the published tables, and are part of the file names for the published spectra.

3.1. 1210: GOODS-S Deep/HST (+JWST)

Observations from the first deep tier of JADES were already presented and extensively described in B23. We refer the reader to that article for all information concerning the observations in program 1210.

3.2. 1180: GOODS-S Medium/HST (+JWST)

The intent of this program was to observe galaxies mainly selected from HST imaging, before any JWST NIRCcam images were available. Six observations were planned, each consisting of two pointings offset by ≈ 7 arcsec to dither over the short-wave detector gap in the parallel NIRCcam observations. Unfortunately, these observations in October 2022 were heavily impacted by MSA shorts (see also Eisenstein et al. 2023a for the specific case of shorts in program 1180). As a result, only four of the 12 target sets were successfully observed in 2022, with three more completed in October 2023. Even though these failed observations were compensated with replanned observations (as described below), they can still be used to measure redshifts for sufficiently bright galaxies. For this reason, we provide reduced data also for the shorts-affected observations. Examples of shorts-contaminated data are provided in Appendix A; a ‘data-reduction flag’ signals spectra affected by data-reduction problems; this includes all spectra from shorts-affected observations, including when the data quality was not severely affected (`DR_flag`). The time for the five remaining pointings was replanned as two observations targeted from NIRCcam imaging, with target selection criteria closely matching that of GOODS-S Medium/JWST program 1286. These are referred to as 1180 GOODS-S Medium/JWST.

The seven completed GOODS-S Medium/HST pointings were observed in a single 3-point nodding pattern



Figure 1. Mosaic of JADES JWST/NIRCam data in the GOODS-N field acquired in February 2023. The F444W, F200W, and F090W mosaics are shown as the red, green, and blue channels in this multicolor image. The scale bar indicates 1 arcmin.

with each of the PRISM, G140M, G235M and G395M dispersers yielding total integration times of 3.8, 3.1, 3.1 and 3.1 ksec, respectively. The highest priority targets were observed in more than one pointing when possible, so some targets have longer integration times.

The two replanned observations in 1180 are known as 1180 GOODS-S Medium/JWST. Due to the amount of time available, observation 134 has two sub-pointings

whereas observation 135 has three. Each sub-pointing has the same dispersers and integration times as in Medium/HST above. The pointings were no longer constrained to be offset by 7 arcsec, and we adopted a strategy to maximize the exposure times of different objects. These observations were executed in January 2023.

3.3. 1181: GOODS-N Medium/HST



Figure 2. Mosaic of JADES JWST/NIRCam data covering the Hubble Deep Field region. Shown are the F444W, F200W, and F090W mosaics as the red-green-blue channels of this multicolor image. The iconic Hubble Deep Field ([Williams et al. 1996](#)) footprint is shown as a silver line. We note the linear diffuse green feature in the center of the image results from local noise in the F200W image and is not an astrophysical object.

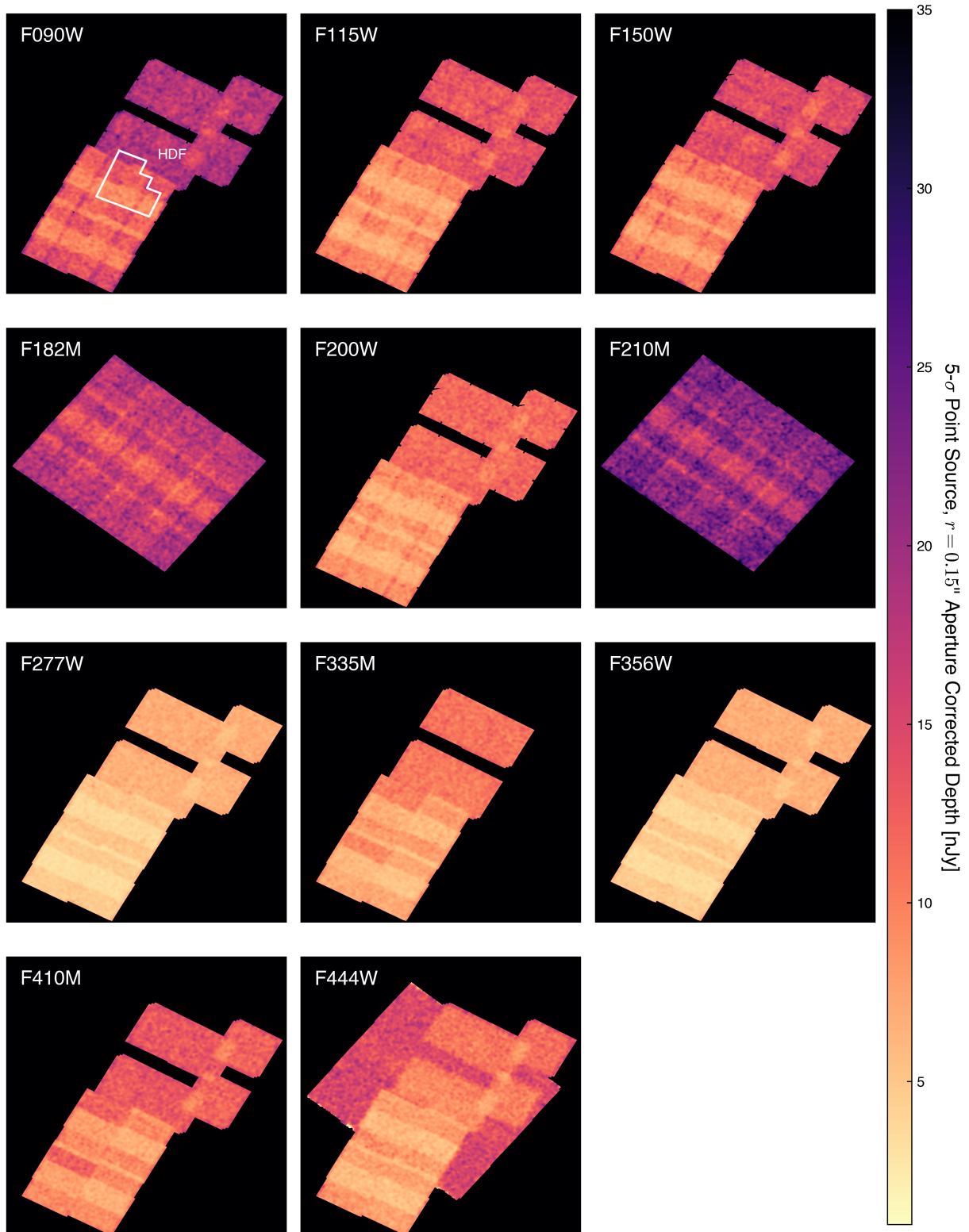


Figure 3. Depth maps of the JWST/NIRCam imaging in the GOODS-N field. Shown are the local, aperture-corrected $5\text{-}\sigma$ point source depths measured in circular apertures with radii $r = 0.3$ arcsec. The F090W, F115W, F150W, F200W, F277W, F335M, F356W, and F410M images use data from the JADES Program. The F182M and F210M data were acquired by the FRESCO survey (Oesch et al. 2023b). The deep F444W data are from the JADES Program, and the shallow/wide F444W tier is from FRESCO. The aperture correction is performed using the model point spread functions from Ji et al. (2023). The color bar indicates the local depth in each filter, as measured in nJy. For reference, the outline of the Hubble Deep Field (Williams et al. 1996) is shown in white on the F090W depth map.

Table 1. GOODS-N JWST/NIRCam Depths

Band	Area	Median Exposure Time	Median Depth ^a	Median Depth
	[arcmin ²]	[s]	[nJy]	[AB]
JADES F090W	56.4	11338	9.8	29.92
JADES F115W	56.4	22676	6.9	29.30
JADES F150W	56.4	11338	7.6	29.19
FRESCO F182M ^b	63.0	12211	11.3	28.77
JADES F200W	56.4	11338	6.4	29.38
FRESCO F210M ^b	60.6	10558	14.4	28.50
JADES F277W	55.5	11338	3.8	29.95
JADES F335M	47.1	8503	6.0	29.45
JADES F356W	55.5	11338	3.7	29.97
JADES F410M	55.5	8503	7.7	29.19
JADES+FRESCO ^b F444W	83.0	10393	6.4	29.38

NOTE—^a Median $r = 0.15$ arcsec aperture corrected 5σ point-source depth. ^b This filter uses data from the FRESCO Program (Oesch et al. 2023b).**Table 2.** Summary of JADES NIRSpec/MSA observations. Under each disperser we report the (minimum/mean/maximum) exposure times; the minimum exposure time can be 0, due to disobedient shutters (for PRISM) and for protecting high-priority targets from overlap (for the gratings).

PID	Field	Depth	Selection	Tier name	PRISM	G140M	G235M	G395M	Targets	Release
					[h]	[h]	[h]	[h]		
1210	GOODS-S	Deep	HST/JWST	goods-s-deepst	(7.8/16.5/28.0)	(2.3/ 4.1/ 7.0)	(2.3/ 4.1/ 7.0)	(2.3/ 4.1/ 7.0)	253	B23
1180 ^a	GOODS-S	Medium	HST	goods-s-mediumst	(0.9/ 1.0/ 4.3)	(0.9/ 1.0/ 4.3)	(0.9/ 1.0/ 4.3)	(0.9/ 1.0/ 4.3)	1342	This work
1180	GOODS-S	Medium	JWST	goods-s-mediumjst1180	(0.3/ 2.1/ 5.2)	(0.9/ 1.8/ 4.3)	(0.9/ 1.8/ 4.3)	(0.9/ 1.8/ 4.3)	533	"
1181	GOODS-N	Medium	HST	goods-n-mediumst	(0.6/ 2.0/ 6.9)	(0.9/ 1.0/ 3.5)	(0.9/ 1.0/ 3.5)	(0.9/ 1.0/ 3.5)	853	"
1181	GOODS-N	Medium	JWST	goods-n-mediumjst	(0.3/ 1.6/ 5.2)	(0.9/ 1.7/ 5.2)	(0.9/ 1.7/ 5.2)	(0.9/ 1.7/ 5.2)	709	"
1286	GOODS-S	Medium	JWST	goods-s-mediumjst	(0.5/ 2.1/ 2.2)	(0.7/ 2.1/ 2.2)	(0.9/ 2.4/ 2.6)	(0.9/ 2.4/ 2.6)	169	"
3215	GOODS-S	Deep	HST	goods-s-ultradeep	(2.8/32.4/61.6)	(2.8/ 7.7/11.2)	—	(11.2/23.0/33.6)	228	"
1286 ^b	GOODS-S	Medium	JWST	—	—	—	—	—	—	2025
1287	GOODS-S	Deep	JWST	—	—	—	—	—	—	"

^a Two-thirds of these observations were affected by 'shorts'. See 3.2 and Appendix A for more details. ^b This data release includes only 1 of 8 observations from PID 1286; the remaining 7 observations were obtained in December 2023 and will be part of a future data release.

This program consists of four observations planned similarly to the six of GOODS-S Medium/HST, with each observation comprising two pointings offset by ≈ 7 arcsec. However, for GOODS-N, the total time used with the PRISM per pointing was increased to 6.3 ksec, using two sets of the 3-point nodding pattern. All but one observations were successfully completed in February 2023.

3.4. 1181: GOODS-N Medium/JWST

This program was planned using JWST NIRCam imaging for target selection. Four observations were planned, each with three sub-pointings offset by ≈ 1 arcsec. Three of the observations were completed between April and May 2023. The fourth was delayed until late May by a guide-star acquisition failure and then partially impacted by MSA shorts. It is scheduled to be completed in May 2024. Each sub-pointing uses the PRISM, G140M, G235M, G395M and G395H dispersers

with total integration times of 3.1 ksec each. The MSA configurations are designed to maximize commonality of the targets in each of the three sub-pointings to yield total integration times of 9.3 ksec per disperser.

3.5. 1286: GOODS-S Medium/JWST

Program ID 1286 is the main GOODS-S Medium/JWST program. These observations were planned the same way as those of GOODS-N Medium/JWST above, each with three sub-pointings separated by ≈ 1 arcsec. Only one of the eight observations was executed during Cycle 1 in January 2023. The remaining seven were observed in October and December 2023. Only the visit from January 2023 is included in this data release. For this visit the integration times per sub-pointing in some dispersers were reduced from 3.1 to 2.7 ksec to fit within the available allocation.

3.6. 3215: GOODS-S Ultra-Deep/JWST

Program ID 3215 is a Cycle 2 GO program that builds on the parallel NIRSpec and NIRCам JADES observations in program 1210 (Eisenstein et al. 2023b). The NIRSpec MSA observation consists of five sub-pointings within 2 arcsec, close to the three sub-pointings of Deep/HST. For each sub-pointing the total integration time is 33 ksec in each of PRISM and G395M and 8.3 ksec in G140M. Four sub-pointings were successfully executed in October 2023. The fifth suffered from a bright MSA short. All of the grating and 25% of the PRISM exposures in visit 5 were unusable. These are scheduled to be re-observed in October 2024.

A subset of the observed spectra is shown in Figure 4, where the targets are in order of increasing redshift from the bottom to the top row. The varying noise level reflects the combination of exposures of different depth.

4. SAMPLE SELECTION

As described in our first JADES NIRSpec data release paper (B23), we employ a priority class system to most efficiently use the micro shutter array of NIRSpec (see Ferruit et al. 2022). The highest priority classes are reserved for objects that are few in number (i.e. having low sky density), typically targeting very high redshift candidates. We use these galaxies to optimize each pointing of NIRSpec (see Section 4.5). Lower-priority classes contain many more galaxies, only a fraction of which actually get placed on shutters. With this, we aim to achieve a statistical sample, and JADES aims to span galaxy evolution from Cosmic Noon to within the Epoch of Reionization. As outlined in Eisenstein et al. (2023c), the JADES spectroscopy has a tiered ‘wedding cake’ survey design, where a smaller number of deep pointings (with long exposure times) are supplemented with medium-depth pointings covering a larger area. As JADES spans a range of science cases, there is not a single selection function for the spectroscopic sample. Instead, each tier has its own prioritization scheme (Tables 3–5). However, each of these schemes is structured in broadly the same way, with the exact criteria changing to reflect the differing input catalogs and differing sensitivity of the observations in each tier.

B23 presented deep spectroscopic observations around the Hubble Ultra Deep Field, including details of the prioritization scheme used for target selection. The data release presented in this paper predominantly introduces the medium tiers of JADES, and the new deep pointing from Program ID 3215.

Some spectroscopic observations were obtained before having JWST/NIRCам imaging. For these, we had to rely on targets selected from existing imaging, predominantly HST, augmented by data from other facilities -

hereafter, we refer to observations planned in this way as ‘Medium/HST’ (Section 4.2).

Later observations benefited from JWST/NIRCам imaging, and targets were selected from these new datasets where possible. This is called Medium/JWST (Section 4.3). However, we note that in some Medium/JWST observations, the MSA footprint extended beyond the NIRCам coverage. These areas of the MSA had to be filled by HST-based catalogs with selection criteria detailed in Column 4 of Table 4, which was designed to mimic the Medium/JWST criteria as best as possible.

We note that Medium/JWST observations were typically deeper than Medium/HST, so although the overall aims of the two tiers are similar, the exact magnitude cuts are different. This is discussed in more detail below.

4.1. Deep/HST

The sample selection for program 1210 is described in B23.

4.2. Medium/HST

Our observations span the two well studied fields GOODS-S and GOODS-N, meaning that our HST-based input target catalogs for our initial spectroscopic observations already had a high target density.

GOODS-S: As described in B23, we assembled a HST-based catalog in GOODS-S by compiling $z > 5.7$ candidates from multiple literature sources that had used a combination of Lyman break dropout criteria and/or photometric redshifts (Bunker et al. 2004; Yan & Windhorst 2004; Oesch et al. 2010, 2013; Lorenzoni et al. 2011, 2013; Yan et al. 2010; Ellis et al. 2013; McLure et al. 2013; Schenker et al. 2013; Bouwens et al. 2015, 2021; Finkelstein et al. 2015; Harikane et al. 2016). These were supplemented by targets of any redshift from large photometric catalog releases, including Skelton et al. (2014), Whitaker et al. (2019), Rafelski et al. (2015), Guo et al. (2013), Caldwell et al. (2008), and Coe et al. (2006). Critical to assembling our HST-based catalog was ensuring the astrometry of these literature sources was accurate relative to the GAIA DR2 astrometric frame used in target acquisition. The details of how this was achieved, by relating catalogs to the Complete Hubble Archive for Galaxy Evolution (CHArGE) re-reduction of the HST imaging (Kokorev et al. 2022; Brammer 2023)², are given in Appendix A of B23.

To establish photometry and a redshift for target prioritization, we cross-matched targets across each of these catalogs. HST broad-band magnitudes were

² <https://s3.amazonaws.com/grizli-stsci/Mosaics/index.html>

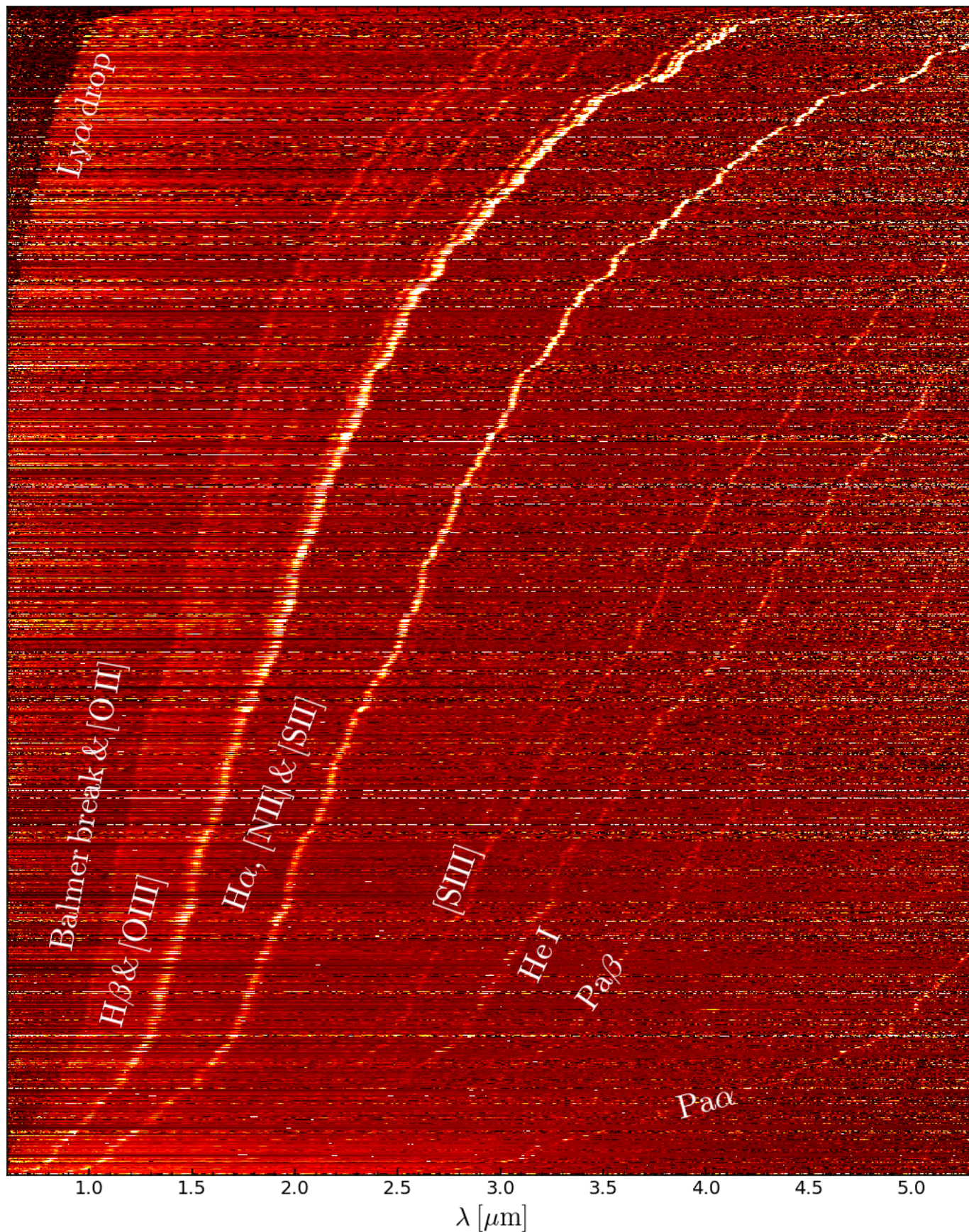


Figure 4. A subset of the observed spectra with multiple emission lines, sorted from bottom to top by increasing redshift. A number of continuum and line features is apparent, illustrating the simultaneous coverage of the rest-frame UV and optical ranges before cosmic noon.

adopted from the latest available catalog in which the target appeared out of Whitaker et al. (2019), Skelton et al. (2014), Rafelski et al. (2015), and Guo et al. (2013), or the discovery paper for targets not appearing in any of these catalogs. If the target did not have a reported magnitude, we remeasured the aperture photometry at the given coordinates. For $z > 5.7$ candidates, we adopt the photometric redshifts of the discovery paper. Other targets are assigned a photometric redshift according to the most recent catalog that reports one. We also cross-matched targets with literature spectroscopic redshift catalogs in GOODS-S (Tasca et al. 2017; Garilli et al. 2008; Kurk et al. 2013; Stark et al. 2013; Kriek et al. 2015; Morris et al. 2015; Momcheva et al. 2016; Inami et al. 2017; Herenz et al. 2017; Pentericci et al. 2018a,b; Maseda et al. 2018). Where we identify matches, these redshifts supersede any photometric redshifts, provided the quality flagging from those catalogs indicated that the redshift was based on either multiple high S/N emission lines, or a high S/N detection of an asymmetric Ly α emission profile.

GOODS-N: The GOODS-N HST-based catalog was assembled in largely the same way. Many of the $z > 5.7$ selection papers listed above also extend their samples to GOODS-N (Oesch et al. 2014; Bouwens et al. 2015, 2021; Finkelstein et al. 2015; Harikane et al. 2016). Again, these were supplemented by targets from large HST photometric releases. Skelton et al. (2014) also covers GOODS-N and was included in our catalog, while we also add in targets from the Barro et al. (2019) catalog. Astrometry was corrected following exactly the same procedure as in GOODS-S.

Photometry was taken from the most recent catalogs of Barro et al. (2019) and Skelton et al. (2014) if available, otherwise from the discovery paper, or, failing that, from our own remeasured aperture magnitudes. Photometric redshifts were established in the same way as above, and these were again superseded by spectroscopic redshifts if a positional match was identified with a target in a literature catalog, as described above (Reddy et al. 2006; Barger et al. 2008; Stark et al. 2011, 2013; Kriek et al. 2015; U et al. 2015; Momcheva et al. 2016; Maseda et al. 2018).

Additionally, for a small number of our Medium/HST observations in GOODS-N, one of the MSA quadrants partially extended beyond the main GOODS-N CANDELS footprint (see Figure 4 in Eisenstein et al. 2023c). CANDELS imaging only extended into this area in one band (F814W) of HST/WFC3 imaging (Grogan et al. 2011). Thus, this MSA real estate could not be populated with targets with robust photometric redshifts in this region. We identified eight objects in this area with

X-ray counterparts from the Chandra Deep Field North X-ray survey (Xue et al. 2016), and these were included in class 3.0 (see Table 3). We then populated the input catalog in this region with targets from more extended imaging, either from Spitzer/IRAC (Ashby et al. 2013) or ground-based imaging from Subaru (Capak et al. 2004). The astrometry of these catalogs is less reliable, and thus, all of these targets were placed only in class 8, although ~ 60 were observed since there was very little competition for shutter real estate in this part of the MSA, and these formed the vast majority of targets from this class that were observed.

Medium/HST target prioritization: For each of GOODS-S and GOODS-N, these catalogs were then divided into priority classes for Medium/HST observations following the scheme outlined in Table 3. The highest priority targets in Medium/HST comprised high-redshift galaxies with photometric redshifts $z > 5.7$, with the lower redshift cut corresponding to the ‘i-band drop-out’ galaxies with the Lyman-break in the HST/ACS F775W filter (see Bunker et al. 2004). These targets were subdivided based on an F160W magnitude cut, prioritizing the brightest sources. Additionally, we performed a visual inspection of the HST imaging, placing the most robust candidates in our highest class. More marginal targets we retained in Class 2, and unconvincing targets were removed.

The next priority classes comprised targets with low surface density, including very bright ($m_{F160W} < 23.5$) $z > 2$ objects (to obtain exceptionally high S/N spectra of a small subset), and any targets considered likely to be AGN, quiescent, or Lyman-continuum leakers at $1.5 < z < 5.7$.

To include more typical star-forming galaxies over this redshift range, we sub-divide our input catalog into four photometric redshift slices ($4.5 \leq z < 5.7$; $3.5 \leq z < 4.5$; $2.5 \leq z < 3.5$ and $1.5 \leq z < 2.5$), with the higher redshift slices having higher priority given that the surface density of these targets is typically lower.

Each redshift slice is then subdivided into three priority classes, the first two based on the HST F160W magnitude (which is the reddest available band in HST, and the best single-band approximation to a stellar-mass selection). This is then supplemented by a star-formation-rate based selection (using SFRs from the 3DHST catalog of Skelton et al. 2014). We converted the SFRs to H α line fluxes, and then to expected S/N for the H α line accounting for typical slit losses of the MSA. Those predicted to have $S/N(\text{H}\alpha) > 15$ in the NIRSpec prism were included in this priority class.

Class 7 then comprised any other literature source with coordinates that could be robustly tied to the

Table 3. Target prioritisation categories for Medium/HST

Priority	Redshift	Criteria	Targets observed
1	$z > 5.7$	$F160W < 27.5$; V.I. Class ¹ 0	68
2.0	$z > 5.7$	$F160W < 27.5$; V.I. Class 1 $27.5 < F160W < 29$; V.I. Classes 0, 1	93
3.0	$1.5 < z < 5.7$	Rare target (e.g., Quiescent, AGN, ALMA...)	27
3.5	$1.5 < z < 5.7$	$F160W < 23.5$	43
4.1	$4.5 < z < 5.7$	$F160W < 25.5$	14
5.1	$4.5 < z < 5.7$	$F160W < 27$	87
6.1	$4.5 < z < 5.7$	$S/N(H\alpha) > 15$	44
4.2	$3.5 < z < 4.5$	$F160W < 25.5$	45
5.2	$3.5 < z < 4.5$	$F160W < 27$	148
6.2	$3.5 < z < 4.5$	$S/N(H\alpha) > 15$	63
4.3	$2.5 < z < 3.5$	$F160W < 25.5$	122
5.3	$2.5 < z < 3.5$	$F160W < 27$	171
6.3	$2.5 < z < 3.5$	$S/N(H\alpha) > 15$	59
4.4	$1.5 < z < 2.5$	$F160W < 25.5$	176
5.4	$1.5 < z < 2.5$	$F160W < 27$	219
6.4	$1.5 < z < 2.5$	$S/N(H\alpha) > 15$	54
7	$z > 1.5$	Has GAIA2 coords and $F160W > 23.5$	265
7.5	$z < 1.5$	Has GAIA2 coords $23.5 < F160W < 27$	317
7.6	$z < 1.5$	Has GAIA2 coords $F160W > 27$	87
8	any z	Anything else with $F160W > 23.5$	115

¹Targets were assigned one of the following visual inspection (V.I.) classes: (0) Most compelling, (1) Plausible $z > 5.7$, but less compelling, (2) Real object but likely $z < 5.7$, (-1) Reject.

GAIA-DR2 astrometric frame (as described in B23) with a photometric redshift $z > 1.5$, and sources at lower redshift (also with GAIA-DR2) subject to F160W magnitude cuts. Finally, we included anything else that was not at risk of saturating exposures in Class 8.

4.3. Medium/JWST

For Medium/JWST, our primary target list came from the recent NIRC*am* images, which extends to longer wavelengths (and in many cases greater depth) than the HST images, and hence revealed more targets with more robust photometric redshifts at high redshift. The target selection criteria are detailed in Table 4

The JADES team produced photometric catalogs (see e.g. Rieke et al. 2023b) and we performed SED fitting with BEAGLE and EAZY (see e.g. Hainline et al. 2023) to determine photometric redshift probability distributions for each target. In addition to the SED-fitting-based

photometric redshifts, we also used color cuts to identify Lyman-break candidates at $z \gtrsim 5.7$. We note that the photometric catalog was being frequently updated as imaging depth was added and NIRC*am* data reduction was improved. Target selection was always performed with the latest catalog available to us at the time of designing the observations. For this reason, in general, the input catalogs differ from catalogs associated with later public data releases of the imaging.

Throughout this section, where we refer to magnitudes, these are usually the ‘CIRC2’ apertures from the photometric catalogs, which was selected to approximate the open area of a NIRS*pec* micro-shutter. However, for Class ≥ 7.0 where we move to $F444W$ -based selections, we switch to using larger apertures, to better approximate a stellar-mass-based selection. For GOODS-S, we used the Kron apertures, while for GOODS-N we used the CIRC4 aperture because the

Kron aperture photometry was not available in GOODS-N at the time of target selection.

We placed galaxies with photometric redshifts higher than 8 in the top priorities, with those brighter than $m_{AB} = 28$ mag in the rest-frame UV ranked top, followed by those with $28 < m_{AB} < 28.5$ mag.

Priority class 4 covers galaxies with $5.7 < z < 8$ with a magnitude cut on the filter which best approximates to the rest-frame UV around 1500 Å. As with the Deep/HST Class 4 in B23 we set a relatively bright magnitude cut such that we would expect the rest-optical emission lines to be well detected to facilitate line ratio diagnostics (with $S/N(\text{H}\alpha) > 25$ in the prism). For Medium/JWST, this rest-UV cut corresponds to $m_{AB} < 26.5$ mag, following the methodology in Section 2.1 of B23. We supplemented this class with some emission-line selected objects with fluxes $> 10^{-17.3} \text{ erg cm}^{-2} \text{ s}^{-1}$ drawn from the FRESCO survey (Oesch et al. 2023b, using a custom data reduction; Sun et al. 2023), from MUSE (Inami et al. 2017; Herenz et al. 2017) and galaxies exhibiting flux excesses in the F410M NIRCcam filter consistent with strong line emission.

Following this, the next class was a small number of very bright ($m_{AB} < 22$ mag) $1.5 < z < 5.7$ targets to enable continuum science. We then targeted more galaxies in the range $5.7 < z < 8$ but fainter than Class 4, split into two rest-UV magnitude bins ($26.5 < m_{AB} < 28$ mag and $m_{AB} > 28$ mag). We supplemented this class with emission-line selected objects with fluxes below $< 10^{-17.3} \text{ erg cm}^{-2} \text{ s}^{-1}$. In the very first epoch of Medium/JWST observations, taken in January 2023, we had sub-prioritised these line emitters as Class 6.0, slightly ahead of the $26.5 < m_{AB} < 28$ mag magnitude cut (Class 6.1). But in all subsequent epochs, these were folded in together as Class 6.1.

For lower-redshift galaxies ($1.5 < z < 5.7$) we used the same 4 redshift slices as for Medium/HST. We created a class of upweighted sources with low target density comprising candidate passive galaxies (selected through the UVJ color criterion, Williams et al. 2009; Leja et al. 2019, and with $F444W < 27$ mag), along with X-ray selected sources (Luo et al. 2017), and these were allocated in descending order of redshift slice. We then turned to the remainder of the galaxies in each redshift bin, where we used the reddest NIRCcam wide filter F444W as a proxy for a stellar-mass-selected sample (selecting on $F444W < 27$ mag), placing each redshift slice in turn as before. We note that this differs from our Medium/HST selection (which is F160W based), as we take advantage of the availability of the redder filter to better approximate to a stellar-mass-limited sample.

Any unused MSA real estate was filled with fainter targets as described in Table 4, Classes 8.0–8.3 & 9. The exact criteria defining Classes ≥ 8.0 were not fixed across all epochs of the Medium/JWST survey. We note that these lower classes were never constructed with a view toward being able to conduct well-defined sample-based studies, and were rather aimed at potentially capturing a few extra worthwhile spectra with what is otherwise spare MSA real estate. For our first Medium/JWST pointings in GOODS-S, Class 8.0 was made up of leftover targets for which, based on the UV magnitude, we predicted $S/N(\text{H}\alpha) > 20$ based on the SFR, and Class 8.1 was remaining candidates with $F444W < 28$ mag. However, it turned out that many of the targets in this Class 8.0 were pushing below the noise threshold such that this did not end up being a very successful selection, and in later iterations we did not keep this delineation. As a result, we advise caution when considering Class ≥ 8.0 objects in the context of sample-based analyses.

4.4. Ultra-deep 3215

Our primary input catalogs for the ultra-deep NIRSpec MSA observations came from the work of Endsley et al. (2023) at $6 \lesssim z < 9$ and Hainline et al. (2023) at $z > 8$, both based on the JADES NIRCcam imaging. These were supplemented with photometric redshifts fits on all galaxies in NIRCcam JADES catalog (down to a flux limit) using the BEAGLE and EAZY codes. These photometric redshifts were combined using a permissive consensus criterion to avoid missing good high redshift candidates.

The ultra-deep spectroscopy in this tier has long exposure times, and, based on our experience with the Deep/HST NIRSpec observation (B23), redshifts could be obtained for galaxies as faint as $AB < 30$ mag. Our highest priority was $z > 11$ galaxies with confident photometric redshifts and magnitudes $AB < 30$ mag, followed by those with less confident redshift solutions. The next class was galaxies at $10 < z < 11$ and $AB < 30$ mag, followed by $8 < z < 10$ (again split into those with convincing photometric redshifts followed by those which had lower confidence).

The next class comprised galaxies with unusual properties, such as extremely blue rest-UV spectral slopes (2 targets), evidence for quiescence (2 targets), high-redshift AGN (2 targets), an object with a large flux excess in the F410M medium-band filter consistent with strong $[\text{O III}]\lambda 5007$ emission at $z \approx 7$, and FRESCO strong line emitters (2 targets).

We then considered the standard sample of objects, moving down in the redshift range. Class 4 includes

Table 4. Target prioritization categories for Medium/JWST

Priority	Redshift	Criteria (if JWST-based)	Criteria (if HST-based)	Targets
1	$z > 8$	$m_{UV} < 28.0$ (V.I. Class = 0) ²		20
2	$z > 8$	$m_{UV} < 28.0$	$z > 8.5, F160W < 28.0$	7
3	$z > 8$	$28.0 < m_{UV} < 28.5$	$z > 8.5, 28.5 < F160W < 28.0$	11
4	$5.7 < z < 8$	$m_{UV} < 26.5$ or L.E. ¹ ($F_{line} \geq 10^{-17.3}$)		19
5	$z > 2$	$m_{AB} < 22$	$2 < z < 5.7 F160W < 22$	5
6.0 & 6.1	$5.7 < z < 9$	$26.5 < m_{UV} < 28$ or L.E. ¹ $10^{-17.8} < F_{line} < 10^{-17.3}$,	$F160W < 28$	78
6.2	$5.7 < z < 8.5$	$28 < m_{UV} < 28.5$	$F160W > 28$	10
7.1	$4.5 < z < 5.7$	UVJ & $F444W < 27$; X-ray sources	$F160W < 28$	3
7.2	$3.5 < z < 4.5$	UVJ & $F444W < 27$; X-ray sources	$F160W < 28$	6
7.3	$2.5 < z < 3.5$	UVJ & $F444W < 27$; X-ray sources	$F160W < 27.5$	14
7.4	$1.5 < z < 2.5$	UVJ & $F444W < 27$; X-ray sources	$F160W < 27.5$	19
7.5	$4.5 < z < 5.7$	$F444W < 27$	$F160W < 28$	65
7.6	$3.5 < z < 4.5$	$F444W < 27$	$F160W < 28$	108
7.7	$2.5 < z < 3.5$	$F444W < 27$	$F160W < 27.5$	177
7.8	$1.5 < z < 2.5$	$F444W < 26$	$F160W < 27.5$	155
7.9	$1.5 < z < 2.5$ $z < 5.7$	$26 < F444W < 27$; or L.E. ¹ $10^{-17.9} < F_{line} < 10^{-17.3}$		50
8.0 & 8.1	$z > 1.5$	$F444W < 28$ mag or $S/N(H\alpha) > 20$	$F160W > 28.5$ & has GAIA2 coords	352
8.2	$z < 1.5$	$F444W < 28$ mag	$24.5 < F160W < 29$ & has GAIA2 coords	171
8.3	no redshift cut	$F444W < 29$	$F160W > 29$ & has GAIA2 coords	99
9	—		$F160W > 24.5$	46

¹Strong line emitters (L.E., units $\text{erg cm}^{-2} \text{s}^{-1}$) were selected based on measurements from FRESCO or MUSE, or targets with a F410M excess. ²Visual inspection (V.I.) Class=0 are the most robust candidates.

targets in the range $5.7 < z < 8$ from the [Endsley et al. \(2023\)](#) catalog, subdividing these into sub-classes 4.1 and 4.2, based on a redshift cut of 7. These objects went down to our $m_{AB} < 30$ mag cut. We supplemented sub-class 4.1 with $5.7 < z < 8$ targets from the full JADES catalog, for which we impose a brighter magnitude cut of $m_{AB} < 28.5$ mag since objects fainter than this had less reliable photometric redshifts.

We then descend in redshift to $4 < z < 5.7$ from our JADES photometric catalog, prioritizing $m_{AB} < 28$ mag (sub-class 5.1) and then $28 < m_{AB} < 29$ mag (sub-class 5.2). Then in class 6, we place leftover objects down to $m_{AB} < 30$ mag in these $5.7 < z < 8$ and $4 < z < 5.7$ slices (as sub-classes 6.1 and 6.2).

We then move to Class 7 which places objects in redshift slices of $2.5 < z < 4$ and $1.5 < z < 2.5$, with each slice subdivided into two classes based on $m_{AB} <$

28 mag and $28 < m_{AB} < 29$ mag. Class 7.5 then places all remaining $z > 1.5$ objects with $m_{AB} < 30$ mag.

Class 8 then places $z < 1.5$ objects divided into three magnitude slices ($m_{AB} < 28$ mag, $28 < m_{AB} < 29$ mag, $29 < m_{AB} < 30$ mag). Finally, Class 9 contains filler objects from the HST-based catalogs described above.

4.5. Target assignment with eMPT and visual inspection

Target placement was performed using the eMPT software ([Bonaventura et al. 2023](#)) and proceeded using the same method as described in [B23](#). Pointing centers are driven by the highest priority class in each tier; Class 1 for Medium/HST and Medium/JWST, and Class 1.1 for Ultra-deep 3215. For all candidates with $z > 5.7$, we visually inspected the individual images and quality of the photometric fits before running the

Table 5. Target prioritization categories for 3215 ‘UltraDeep’

Priority	Redshift	Criteria	Targets
1.1	$z > 11$	$m_{AB} < 30$	4
1.2	$z > 11$	$m_{AB} < 30$ and less reliable phot- z	0
2.1	$10 < z < 11$	$m_{AB} < 30$	0
2.3	$8 < z < 10$	$m_{AB} < 30$	6
2.4	$8 < z < 10$	$m_{AB} < 30$ and less reliable phot- z	2
3.1		rare objects ¹	5
3.2		rare objects ²	4
4.1	$7 < z < 8$	$m_{AB} < 30$ from Endsley et al.	
	$5.7 < z < 8$	$m_{AB} < 28.5$ from other phot- z	3
4.2	$5.7 < z < 7$	$m_{AB} < 30$ from Endsley et al.	8
5.1	$4 < z < 5.7$	$m_{AB} < 28$	15
5.2	$4 < z < 5.7$	$m_{AB} < 29$	23
6.1	$5.7 < z < 8$	$28.5 < m_{AB} < 30$	14
6.2	$4 < z < 5.7$	$m_{AB} < 30$	29
7.1	$2.5 < z < 4$	$25 < m_{AB} < 28$	15
7.2	$2.5 < z < 4$	$28 < m_{AB} < 29$	12
7.3	$1.5 < z < 2.5$	$25 < m_{AB} < 28$	14
7.4	$1.5 < z < 2.5$	$28 < m_{AB} < 29$	15
7.5	$z > 1.5$	$29 < m_{AB} < 30$	17
8.1	$z < 1.5$	$25 < m_{AB} < 28$	21
8.2	$z < 1.5$	$28 < m_{AB} < 29$	7
8.3	$z < 1.5$	$29 < m_{AB} < 30$	5
9		class 9 objects in Deep/HST	9

¹Rare objects includes: blue UV slopes, AGN $7 < z < 12$, MIRI $z > 7$, X-ray $z > 4$, medium-band $\log(\text{line flux}/\text{erg cm}^{-2} \text{s}^{-1}) > -18.3$

²Rare objects includes: ALMA, MIRI $z < 7$, AGN $4 < z < 7$, medium-band $\log(\text{line flux}/\text{erg cm}^{-2} \text{s}^{-1}) < -18.3$

EMPT to ensure they had good redshift fidelity. An inspection of the full input catalog of many tens of thousands of galaxies was not practical, but we did inspect everything that the EMPT had allocated shutters to when designing trial MSA configurations. Sources that were badly contaminated by neighboring objects were removed, and the EMPT re-run at the same location to assign new targets in place of those rejected (this was typically less than 10 objects per MSA pointing). In allocating shutters, we require the centroid of the object to fall within an ‘admittance zone’ as described in B23. For the low-dispersion prism, we do not allow the spectra of any target to overlap. As with our Deep/HST observations, we keep the same MSA configuration for the grating spectra as for the prism, which means that the higher-dispersion spectra (which are more extended on the array) do overlap, and we use the prism spectra to avoid confusion in line identifications. The grat-

ing spectra of a small number of sources (the highest priority sources, and very bright objects) are protected against overlap by closing the shutters of lower-priority targets in nearby rows. This means that a small number of objects are observed in the prism alone.

5. NIRSPEC/MSA DATA REDUCTION

The data reduction pipeline for this release is the same as in B23. However, the larger dataset enables us to discuss more in detail some of the calibration issues highlighted in DR1.

The pipeline is developed by the ESA NIRSPEC Science Operations Team (SOT) and Guaranteed Time Observations (GTO) NIRSPEC teams (Alves de Oliveira et al. 2018; Ferruit et al. 2022). Most of the processing steps are similar to those adopted by the STScI pipeline used to generate the MAST archive products, but the background subtraction, rectification, 1D ex-

traction, and spectra combination steps have been optimized for the targets observed in JADES programs (see details in B23). In particular, we apply a wavelength correction to compensate for the wavelength bias of non-centered compact sources. This bias arises for sources that are smaller than the slit width, when they are spatially offset within the shutter along the dispersion axis. The issue is discussed in Ferruit et al. (2022), and we apply the correction they propose (cf. their Figure 9).

During the quality assessment of NIRSpec observations, we noted that some shutters failed to open when the MSA was configured at each pointing. These unexpected disobedient shutters might corrupt both the estimate of the background emission and the science spectrum during the data processing workflow. The impact of disobedient shutters is evident in the PRISM/CLEAR observations where the background and target emission are prominent. Therefore, we initially analyzed the presence of these failed shutters by processing the data without background subtraction and identifying those shutters in which the signal is consistent with no emission. We removed such disobedient shutters from the MSA mask and re-processed the data following the standard procedure. Only 3 per cent of the targets are affected by disobedient shutters, reducing the total exposure time dedicated to the selected galaxy. In most cases, we just removed only one of the 3 shutters forming the target slitlet, but for a few targets, the number of disobedient shutters for the slitlet was 2 and even 3.

In Figure 5 we illustrate our current flux and wavelength calibration issues using 199773 (panel c), a massive quiescent galaxy at redshift $z = 2.8$, where we detect several stellar absorption lines in the medium-resolution gratings. In panel (a) we show the prism spectrum (solid black) and the combined G140M and G395M spectra (blue; no G235M observations are present in PID 3215). The yellow line is the grating spectrum re-binned to the prism wavelength grid, the red line shows the grating spectrum after matching the resolution of the prism (using a Gaussian kernel) and then rebinning. In principle, the red and black lines should overlap, but we can see substantial mismatches in both flux level and wavelength; this is illustrated in panel (b), where we show the ratio between the flux densities of the gratings and prism (after rebinning, yellow, and after smoothing and rebinning, red). At wavelengths $\lambda < 1.3 \mu\text{m}$ the flux levels agree to within 5 per cent, but at $1.3\text{--}1.5 \mu\text{m}$ the G140M flux increases reaching a ratio of 10–15 per cent, before going down again from $1.5 \mu\text{m}$. Being part of PID 3215, this object has no G235M data, but the G395M data show instead a higher flux mismatch of 15 per cent on average with respect to the prism, though with tapering

both at the blue and red ends of the grating spectrum (see also Figure 16 in Section 11, illustrating another source with continuum detected in the medium gratings).

At the same time, we confirm that overall the medium gratings require a lower redshift solution than the prism (Section 9 and B23).

6. PRELIMINARY REDSHIFT IDENTIFICATION

Prior to running the flux measurement software, we measure an initial redshift estimate using a two-step process. In the first step, we run the spectral modeling software BAGPIPES (Carnall et al. 2019) on the prism data. Our setup is optimized for time-efficient redshift measurement, by using a parametric star-formation history which may not fit well the stellar continuum. This step returns both a redshift estimate and a fiducial model spectrum. A detailed description of this procedure is available in B23; an example BAGPIPES model fit is reported in Figure 6 (orange line). Each galaxy is then visually inspected by at least two team members, who use a rudimentary graphics interface to compare the BAGPIPES model to all the available data, including the grating spectra, if available. To assist in the decision, the interface displays a set of strong spectral features (Section 6.1). In this step, the astronomers can change the redshift and assign a quality flag.

6.1. Visual redshift determination

The visual inspection is performed using a program which presents the user simultaneously with all the available information in a compact interface. The console is shown in Figure 6, open on target ID 5591 (GN-z11; Oesch et al. 2016; Bunker et al. 2023a; Maiolino et al. 2023a) from medium/*JWST* GN. The top panel shows the 1-d prism spectrum, with overlaid the BAGPIPES model, and a set of reference spectral features (vertical dashed lines). Various buttons enable the user to display the 1-d S/N, the 1-d uncertainty, additional lines and, crucially, data from other dispersers. The bottom panel shows the 2-d S/N map. Finally, the console automatically opens FITSMAP (Hausen & Robertson 2022) centered on the current target; FITSMAP gives the user access to the panchromatic *JWST*/NIRCam and *HST* photometry (Rieke et al. 2023a), including the photometric redshifts based on EAZY (Brammer et al. 2008; Hainline et al. 2023).

The user is able to change interactively the redshift and judge different solutions. The outcome of this inspection is a user-validated redshift (or no redshift) and a set of flags (Table 6). Users can optionally enter comments; the only mandatory comment is to specify when

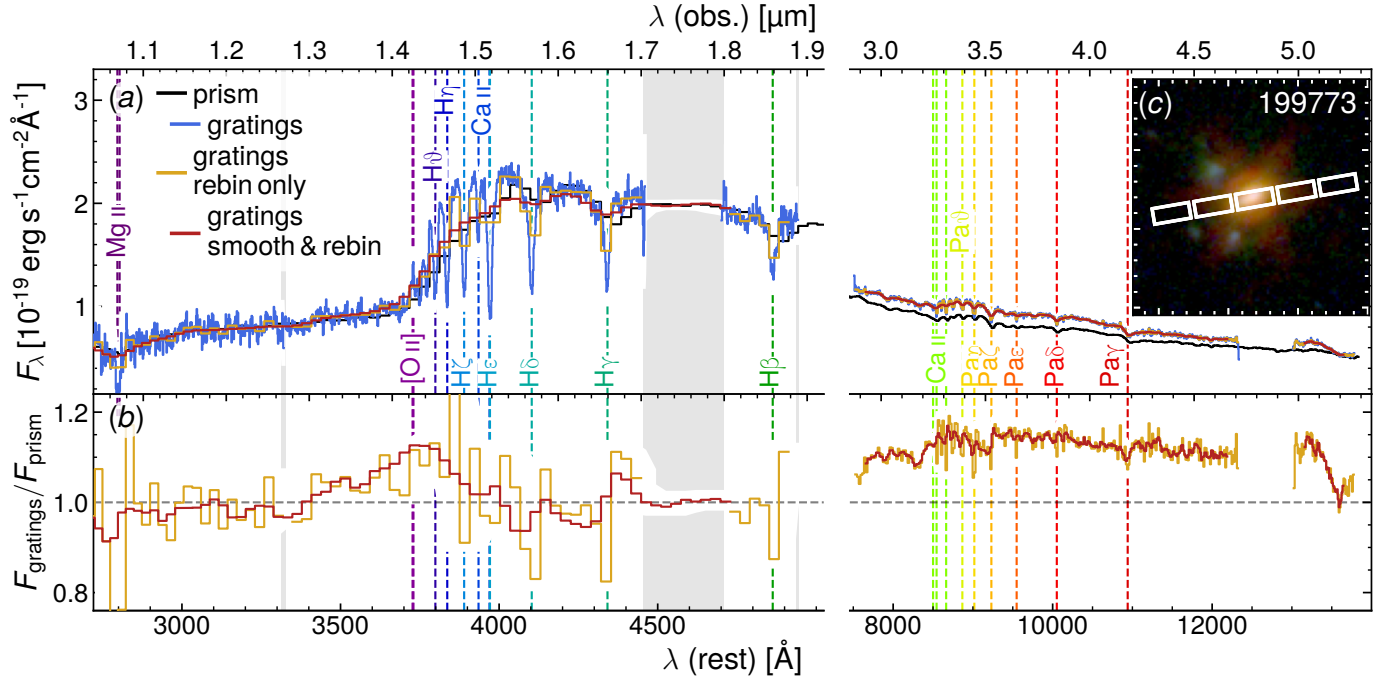


Figure 5. Target ID 199773 from PID 3215, illustrating remaining calibration problems. Panel (a) shows the prism and gratings data (black and blue, G140M to the left and G395M to the right), and the gratings data after rebinning to the prism grid (yellow) and after matching the nominal resolution of the prism and then rebinning (red; vertical gray areas highlight spectral regions where we interpolated over missing grating data, due to bad pixels or the detector gap; the red line is clipped at the edges of the wavelength range due to the size of the convolution kernel). Panel (b) shows the ratio between the rebinned and smoothed-then-rebinned grating spectrum and the prism spectrum (same line colors as panel a). The flux calibration mismatch between prism and gratings is wavelength dependent, and is most severe in G395M. The galaxy image is shown in panel (c), with the MSA shutters overlaid. From Z. Ji et al. (in prep.)

there is a serendipitous source in the shutter. Typical comments include prominent or peculiar morphologies and doubt about alternative possibilities.

Each galaxy has been inspected by at least two people and by up to four. When the sample is fully inspected, the user sends the resulting catalog of redshifts and flags for merging. The catalogs are compared based on their redshift value. Redshifts that agree to within a tolerance of a spectral pixel are averaged; targets that have different redshifts or redshift flags are re-inspected and a final decision is taken. The resulting redshifts are then used as input in various analysis steps, ranging from emission-line measurements (as described in this article), to Bayesian spectral modeling (e.g., BEAGLE, PROSPECTOR).

The distribution of visual redshift flags from this procedure is illustrated in Figure 7.

7. PRISM EMISSION-LINE FLUXES

We use the spectral fitting software PPXF (Cappellari 2023), to model the data as a linear combination of spectral templates. As input templates, we use a set of simple stellar-population spectra from FSPS (SSP; Conroy et al. 2009). The spectra were calculated using

Table 6. Flag values and meanings used in the visual inspection. These can be thought of as bit flags, hence in general a target has multiple flags.

Value	Description
0 ^a	Not inspected
1 ^b	Impossible to determine
2	Tentative
3	Peculiar ^c
4	From continuum
5	Single prism line
6	Multiple prism lines
7	Multiple medium-grating lines
8	Multiple high-resolution grating lines
9	Prism data corrupted
10	Medium-resolution data corrupted
11	High-resolution data corrupted

^a Cannot be combined with other flags. ^b Cannot be combined with other flags, except 9, 10 and 11. ^c Usually a serendipitous source in the shutter. User must enter a comment.

MIST isochrones (Choi et al. 2016), the C3K model atmospheres (Conroy et al. 2019), and a Salpeter initial

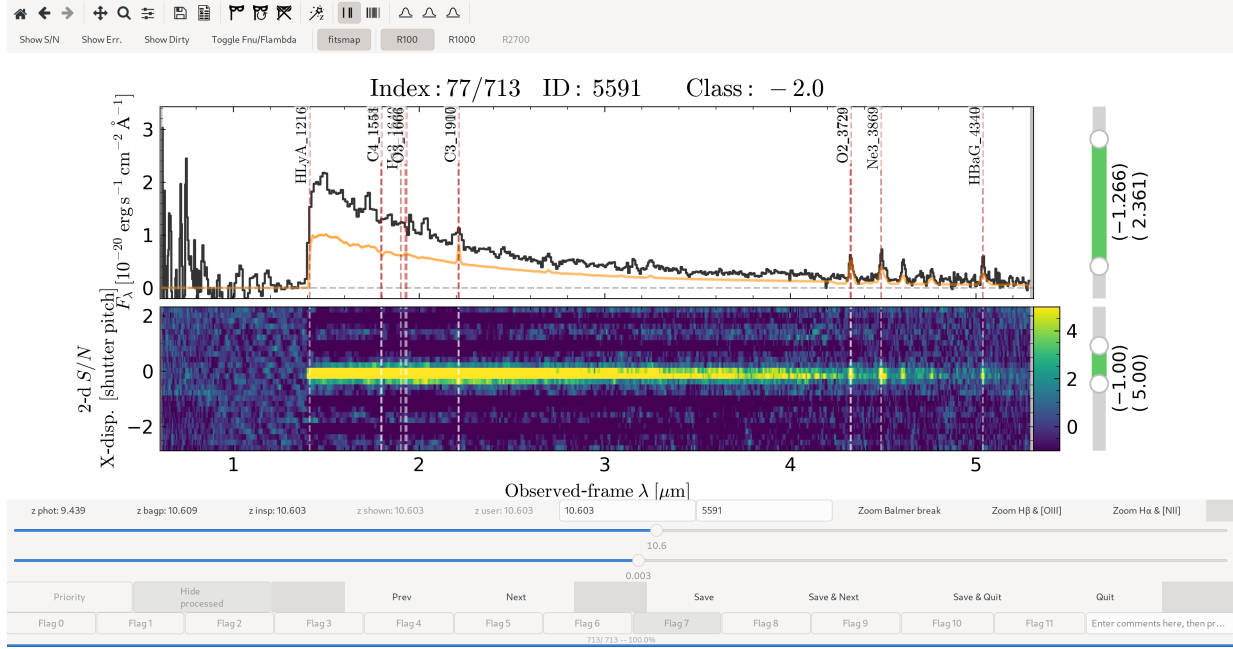


Figure 6. The interface used to visually inspect NIRSpect data, showing GN-z11 (ID 5591 in medium/*JWST* GN; Oesch et al. 2016; Bunker et al. 2023a; Maiolino et al. 2023a). The console displays simultaneously the 1-d spectrum and 2-d S/N map. The user is able to move a set of bright spectral features to be used as reference (vertical dashed lines). The bottom row of console is the set of flags the user can assign.

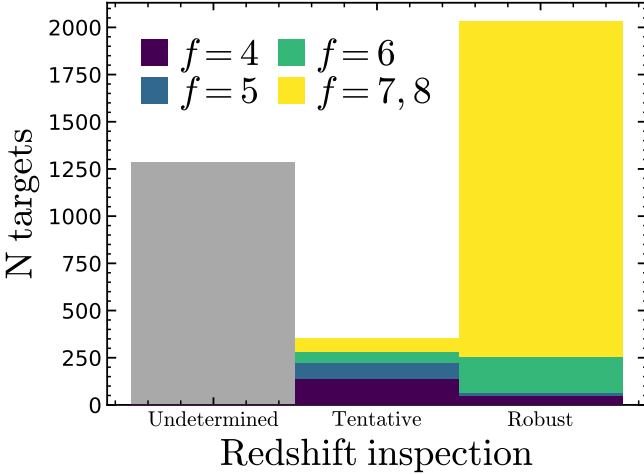


Figure 7. Summary of the visual inspection; the left column shows targets for which a redshift could not be determined (flag 1). Galaxies with uncertain redshifts (center) and with secure redshifts (right) are split by the highest-confidence redshift flag, colored as labeled. Overall, the current success rate of JADES redshifts is 65 per cent.

mass function (Salpeter 1955). The spectral resolution is $R=10,000$ between $0.1 < \lambda < 3 \mu\text{m}$; these templates are available from C. Conroy upon reasonable request. We consider a subset of the templates grid spanning logarithmically ages 0.03–20 Gyr and metallicities $[Z/H] -2.5-0$. We adjust the age grid to each target, ensuring that the oldest available SSP is consistent with the

age of the universe at the redshift of the target (see e.g., Looser et al. 2023b).

In addition to these stellar templates, we use a set of Gaussian templates to represent nebular emission lines. The gas templates are of three kinds; single Gaussians that represent individual emission lines that are spectrally isolated at any redshift (e.g., $\text{He I}\lambda 5787$, $\text{Pa}\beta$), single Gaussians that represent multiple, spectrally blended lines (e.g., $\text{H}\alpha + [\text{N II}]\lambda\lambda 6549, 6584$, $\text{H}\gamma + [\text{O III}]\lambda 4363$), and doublet Gaussians representing doublets with fixed ratios (e.g., $[\text{O III}]\lambda\lambda 4959, 5007$, $[\text{S III}]\lambda\lambda 9069, 9532$). A summary of emission-line templates and their redshift range is shown in Table 7. Note that the exact set of templates used depends on the source initial redshift; this is because the spectral resolution of the prism is a strong function of wavelength (Jakobsen et al. 2022), causing emission-line groups to be spectrally resolved or unresolved at different redshifts. Moreover, we include a step function that is meant to capture very strong Balmer jumps (e.g., Cameron et al. 2023). All these templates are bound to have non-negative coefficients in the linear combination. Finally, we use a 10th-order multiplicative Legendre polynomial to adapt the shape of the continuum to the data; this can be thought of as a combination of physical effects (e.g., dust reddening) and flux calibration (e.g., incorrect slit-loss corrections, for extended objects and for objects with strongly wavelength-

dependent morphology). Before running PPXF, each input template is smoothed to twice the spectral resolution of the data, the templates are truncated to match the approximate rest-frame wavelength range of the data, and stellar flux blue-ward of Ly α is set to 0. The templates are additionally convolved with a velocity distribution, modeled as a Gaussian. We run PPXF two times for each galaxy; in the first instance, we ‘tie’ the templates in kinematic subsets, constrained to have the same velocity and velocity dispersion. The kinematic groups are: Balmer lines and stellar templates, rest-frame UV lines, rest-frame optical lines and rest-frame NIR lines. After this first pass, all lines detected to at least 5σ are kept, whereas the others are discarded. In the second run, we fix the kinematics of the stellar continuum absorption, use only previously detected emission line templates, and remove almost all kinematic groups. Exceptions to the latter rule are: the blend group formed by [S II] $\lambda\lambda$ 6717,6730 and the blend H α + [N II] $\lambda\lambda$ 6549,6584; the group formed by H β and [O III] $\lambda\lambda$ 4959,5007; the group formed by H γ and [O III] λ 4363; and the group of He I λ 10830 and Pa γ , whose kinematics are always tied together. We note that He I λ 10830 is resonant, therefore this emission-line tends to be redshifted relative to the systemic velocity; however, leaving the line kinematics free relative to Pa γ tended to produce bad fits due to low spectral resolution. Therefore, we opted to keep these lines tied. These conditions track the setup of B23, and are necessary due to the limited spectral resolution of the prism, particularly in the range 1–2 μm . A difference with respect to B23 is that we fix the flux ratio between the emission lines of the [O III] $\lambda\lambda$ 4959,5007 and [S III] $\lambda\lambda$ 9069,9532 doublets. Other doublets with fixed line ratios are not enforced due to being unresolved (e.g., O II] $\lambda\lambda$ 1661,1666) or blended with other lines (e.g., [Ne III] $\lambda\lambda$ 3869,3968).

After each fit, we post-process the line fluxes as follows. Below redshift $z < 2$, we combine H β and [O III] $\lambda\lambda$ 4959,5007 and H α + [N II] $\lambda\lambda$ 6549,6584 and [S II] $\lambda\lambda$ 6717,6730; the line uncertainties are added in quadrature. Between $2 \leq z < 5.3$, we combine the flux from the [O III] $\lambda\lambda$ 4959,5007 doublet. Unlike for DR1, the flux of Ly α is never provided, due to the difficulty of modeling the source continuum in the vicinity of this line. We refer the reader to G. Jones (in prep.) for Ly α emitters.

The resulting best-fit spectra were visually inspected for artifacts and bad fits. The most common of these are low equivalent width emission lines near the Balmer break, emission lines due to contaminants, and outliers, especially in shorts-affected observations. The low equivalent width emission lines near the Balmer

break arise when the shape of the break is not fit correctly, and the algorithm may use [O III] $\lambda\lambda$ 4959,5007, [Ne III] $\lambda\lambda$ 3869,3968 and H δ to add to the continuum. Contaminants and artifacts may escape the sigma-clipping in PPXF when they fall close to strong emission lines in the intended target. All these instances were masked in the data table, and are flagged with a dedicated flag PRISM_flux_flag.

8. MEDIUM-RESOLUTION GRATINGS EMISSION-LINE FLUXES

We fitted the medium-resolution spectra using QubeSpec’s³ fitting module. Each emission line was fitted using a single Gaussian component and the continuum was fitted as a power law. This simplistic approach is sufficient for describing a narrow range of the continuum around an emission line of interest ($\pm 100 \text{ \AA}$), because usually the continuum is poorly detected. The majority of the emission lines are fitted in isolation except for a group of emission lines that are close to each other. We show the full list of emission lines fitted in this work and the groups fitted together in Table 9.

To estimate the model parameters we use QubeSpec, a Bayesian modeling code implemented with the Markov-Chain Monte-Carlo (MCMC) integrator emcee (Foreman-Mackey et al. 2013). To measure the emission-line fluxes, we need to set prior probabilities for each of the variables. The peaks of the Gaussian profiles and the continuum normalization are given a log-uniform prior, while the FWHMs are set to a uniform distribution spanning from the minimum spectral resolution of the NIRSpec/MSA ($\sim 200 \text{ km s}^{-1}$) up to a maximum of 800 km s^{-1} . The prior on the redshift was a truncated normal distribution centered on the redshift from the visual inspection and with a standard deviation of 300 km s^{-1} and with a maximum allowed deviation of $1,000 \text{ km s}^{-1}$.

For emission lines that lie in the overlap of the gratings, we fit both sets of the data and report the properties of the fit with the highest SNR. We do not attempt to stack these spectral overlaps due to different line spread function and potential flux calibration offsets between the gratings. This will be further investigated in a future data release.

We fit only a single Gaussian per emission line in the medium-resolution grating. We note that there are some objects with detected outflows or broad line regions. These fits will be further investigate in I. Juodžbalis et al. (in prep.) and S. Carniani et al. (in prep.).

³ <https://github.com/honzascholtz/Qubespec>

Table 7. List of the emission lines fit in the prism spectra. All wavelengths are in vacuum.

Line(s)	λ [Å]	z range	Column name	Notes
C IV $\lambda\lambda$ 1549,1551	1549.48	—	C4_1549	
He II λ 1640 + O III] $\lambda\lambda$ 1661,1666	1650.00	—	Blnd_He2_03_1650	
C III] $\lambda\lambda$ 1907,1909	1907.71	—	C3_1907	
Mg II $\lambda\lambda$ 2796,2803	2799.94	—	Mg2_2796	
[O II] $\lambda\lambda$ 3726,3729	3728.49	—	O2_3727	
[Ne III] $\lambda\lambda$ 3869,3968	3869.86,3968.59	$0 < z < 5.3$	Ne3_3869,Ne3_3968	
[Ne III] λ 3869	3869.86	$z \geq 5.3$	Ne3_3869	
[Ne III] λ 3968 + He	3968.59	$z \geq 5.3$	Ne3_3968	
H δ	3728.49	—	HD_4102	
H γ + [O III] λ 4363	4341.65	$0 < z < 5.3$	Blnd_HG_03	
{ H γ	4341.65	$z \geq 5.3$	HG_4341	
	[O III] λ 4363	$z \geq 5.3$	O3_4363	
{ H β	4862.64	$0 < z < 2$	Blnd_HB_035007d	
	[O III] $\lambda\lambda$ 4959,5007	$0 < z < 2$		
{ H β	4862.64	$2 \leq z < 5.3$	HB_4861	
	[O III] $\lambda\lambda$ 4959,5007	$2 \leq z < 5.3$	O3_5007d	
{ H β	4862.64	$z \geq 5.3$	HB_4861	
	[O III] $\lambda\lambda$ 4959,5007	$z \geq 5.3$	O3_4959,O3_5007	
He I λ 5875	5877.25	—	He1_5875	
[O I] $\lambda\lambda$ 6300,6363	6302.05,6363.67	—	O1_6300	
{ H α + [N II] $\lambda\lambda$ 6549,6584	6564.52	$0 < z < 2$	Blnd_HA_N2_S2	
	[S II] $\lambda\lambda$ 6717,6730	$0 < z < 2$		
{ H α + [N II] $\lambda\lambda$ 6549,6584	6564.52	$z \geq 2$	HA_6563	
	[S II] $\lambda\lambda$ 6717,6730	$z \geq 2$	S2_6725	
He I λ 7065	7067.14	—	He1_7065	
[S III] $\lambda\lambda$ 9069,9532	9071.10,9533.20	—	S3_9069,S3_9532	
Pa δ	10052.12	—	PaD_10049	
{ He I λ 10829	10832.06	—	He1_10829	
	Pa γ	10940.98	—	PaG_10938
Pa β	12821.43	—	PaB_12818	
Pa α	18755.80	—	PaA_18751	

The set of templates used to fit any given galaxy depends on its initial redshift guess; this is because the spectral resolution of the prism is a strong function of wavelength (Jakobsen et al. 2022), causing emission-line groups to be spectrally resolved or unresolved at different redshifts. Empty redshift ranges indicate the template is used at all redshifts. Rows connected by curly braces indicate emission-line pairs/groups that have tied velocity and velocity dispersion.

After the initial fitting run, we visually inspect every model for any incorrect fits or spurious line detection that are caused by unflagged outliers. These flagged fits are then refitted and re-inspected. The fluxes are calculated using the MCMC chains (after discarding the burn-in chains) and the final reported values and their uncertainties are the median value and standard deviation from the chains. We only report detections at $\text{SNR} > 5$; for non-detections we report the $1\text{-}\sigma$ uncertainties for the user to define their own upper limits. The final redshift from the medium-resolution spectra is the redshift inferred from the best detected emission line.

The structure of the gratings emission line catalog is presented in Table 10 in units of $\times 10^{-18}$ erg s $^{-1}$ cm $^{-2}$. The names of the individual emission lines column are the same as reported in Table 9. For the emission line doublets with fixed line ratios (such as [N II] $\lambda\lambda$ 6549,6584 and [O III] $\lambda\lambda$ 4959,5007) we only report the flux of the stronger emission line. Alongside the fluxes and their uncertainties, the initial rows are the same as for the prism table.

9. QUALITY ASSESSMENT

Table 8. Structure of the prism flux table. The full list of emission lines is reported in Table 7; all fluxes are in units of $\times 10^{-18}$ erg s $^{-1}$ cm $^{-2}$.

Column name	Description
NIRSpec_ID	ID of the target in eMPT ‡
TIER	Name of subset †
PID	Program ID
RA_TARG	Target right ascension [degrees]
Dec_TARG	Target declination [degrees]
Field	Name of field (GS or GN)
NIRCam_ID	ID of matched NIRCam source †
RA_NIRCam	NIRCam right ascension [degree]
Dec_NIRCam	NIRCam declination [degree]
x_offset	Intra-shutter target offset [arcsec]
y_offset	Intra-shutter target offset [arcsec]
ObsDate	Date of observations
Priority	Target Priority
assigned_Prism	True if has prism observations
...	...
assigned_G395H	True if has G395H observations
nDither_Pr	Number of dithers for prism
nDither_Gr	Number of dithers for gratings
nInt_Prism	Number of integrations for prism
...	...
nInt_G395H	Number of integrations for G395H
tExp_PRISM	Exposure time for prism [s]
...	...
tExp_G395H	Exposure time for F290LP/G395H [s]
DR_flag	True if problem in reduction or shorts
PRISM_flux_flag	True if at least one line flagged
z_Spec	Redshift (both prism and gratings)
z_Spec_flag	Redshift flag (both prism and gratings)
z_PRISM	Prism-based redshift
C4_1549_flux	C IV $\lambda\lambda 1549, 1551$ flux
C4_1549_err	C IV $\lambda\lambda 1549, 1551$ flux uncertainty
...	...
PaA_18751_flux	Pa α flux
PaA_18751_err	Pa α flux uncertainty

‡ NIRSpec_ID are not unique in the table, but the combination of NIRSpec_ID and TIER is unique. † NIRCam_IDs are unique, but whether they match the NIRSpec_IDs depends on target selection (*HST* vs *JWST* selection), as well as on whether the NIRCam catalog was revised after the NIRSpec observation (which may result in sources being lost to blending and to crossing the non-detection threshold).

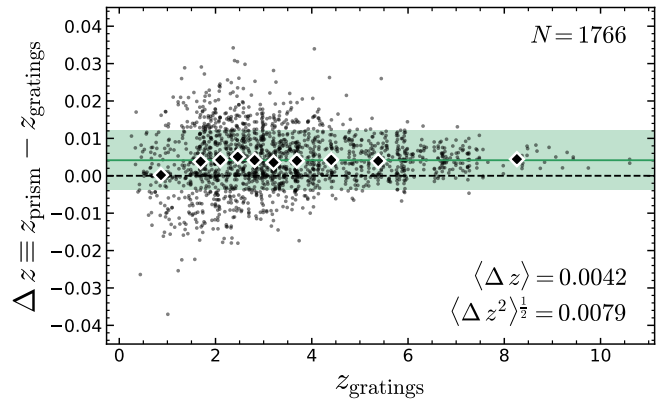


Figure 8. Comparison of redshifts between the prism and the medium-resolution gratings. We find a redshift-independent offset $\Delta z = 0.0042$ (blue line), consistent with B23; the shaded region is the standard deviation. The increased dispersion at low redshifts is expected from the strong dependence of the prism spectral resolution with wavelength. The black diamonds are the moving median; there is some evidence for a reduced bias around $z < 1$.

9.1. Redshift combination and comparison: prism vs medium gratings

In Figure 8 we compare the redshift measurements from the prism and from the medium gratings, where both are available. Having defined $\Delta z \equiv z_{\text{prism}} - z_{\text{gratings}}$, we find a mean of 0.0042 ± 0.0002 and a standard deviation of 0.079, consistent with the findings of B23. This statistically significant offset points to a residual wavelength calibration problem in the prism or medium gratings. We find the offset to be redshift independent; a line fit with the robust least trimmed squares algorithm (using the python implementation `ltsfit`; Rousseeuw & Driessen 2006; Cappellari et al. 2013) is consistent with a flat slope of 0.0002 ± 0.0001 . The increased scatter at low redshift is a consequence of the rapid increase of the prism spectral resolution with wavelength; multiplying Δz by $R/(1+z)$ the scatter becomes approximately uniform with z (where R is the prism spectral resolution of the [O III] $\lambda 5007$ line at redshift z , and z is the redshift of each source).

Whenever we have a strong line detection (5σ) in the medium gratings, we adopt the redshift of this line as the object redshift (flag A). Using a single emission line is warranted because medium-resolution fits are made only for galaxies with a visual-inspection flag of 7 (Section 6). We checked that there are no cases where the grating and prism spectra disagree by more than $\Delta z = 0.05$, so we can rule out any mis-identified lines. Large offsets ($|\Delta z - \langle \Delta z \rangle| > 0.015$ (Figure 8) were visually inspected, and are mostly due to uncertainties in the H β -[O III] $\lambda\lambda 4959, 5007$ blend and to low signal-to-noise data.

Table 9. List of the emission lines fit in the medium-resolution grating spectra. All wavelengths are in vacuum. Rows connected by curly braces indicate emission lines that were fitted using the same redshift and FWHM during the same fit because they are sufficiently close in wavelength that the continuum can be modeled simultaneously.

Line(s)	λ [Å]	Column name
{ C IV $\lambda\lambda$ 1549,1551 He II λ 1640 O III $\lambda\lambda$ 1661,1666	1549.48	C4_1549
	1640.00	He2_1640
	1663.00	O3_1663
C III $\lambda\lambda$ 1907,1909	1907.71	C3_1907
{ [O II] $\lambda\lambda$ 3726,3729 [Ne III] λ 3869 H δ	3728.49	O2_3727
	3869.86	Ne3_3869
	3728.49	HD_4102
{ H γ [O III] λ 4363 H β	4341.65	HG_4341
	4363.44	O3_4363
	4862.64	HB_4861
[O III] $\lambda\lambda$ 4959,5007	4960.30,5008.24	O3_5007
He I λ 5875	5877.25	He1_5875
[O I] $\lambda\lambda$ 6300,6363	6302.05	O1_6300
{ H α [N II] $\lambda\lambda$ 6549,6584 [S II] $\lambda\lambda$ 6717,6730	6564.52	HA_6563
	6585.27, 6549.86	N2_6584
	6718.29, 6732.67	S2_6718, S2_6732
He I λ 7065	7067.14	He1_7065
[S III] $\lambda\lambda$ 9069,9532	9071.10,9533.20	S3_9069,S3_9532
Pa δ	10052.12	PaD_10049
He I λ 10829	10832.06	He1_10829
Pa γ	10940.98	PaG_10938
Pa β	12821.43	PaB_12818
Pa α	18755.80	PaA_18751

Table 10. Structure of the gratings flux table. The initial rows are the same as for the prism (between NIRSpec_ID and z_PRISM; cf. Table 8); all fluxes are in units of $\times 10^{-18}$ erg s $^{-1}$ cm $^{-2}$.

Column name	Description
NIRSpec_ID	ID of the target in eMPT ‡
TIER	Name of subset ‡
...	...
tExp_G395H	Exposure time for F290LP/G395H [s]
z_Spec	Redshift (both prism and gratings)
z_Spec_flag	Redshift flag (both prism and gratings)
z_PRISM	Prism-based redshift
C4_1549_flux	C IV $\lambda\lambda$ 1549,1551 flux
C4_1549_err	C IV $\lambda\lambda$ 1549,1551 flux uncertainty
...	...
PaA_18751_flux	Pa α flux
PaA_18751_err	Pa α flux uncertainty

‡ NIRSpec_ID are not unique in the table, but the combination of NIRSpec_ID and TIER is unique.

If no lines have been detected in the medium gratings, we use the prism redshift, requiring at least two emission lines for a secure redshift (flag B), or the combination of a line and/or a strong continuum break (for a less secure or less precise redshift, flag C). An even lower class is reserved for redshifts identified as tentative in the visual inspection; in this case, we report the visual-inspection redshift (flag D). All other redshifts are assigned -1 (flag E). To summarize, the final redshift flags are:

- A Redshift from at least one emission line in the medium-resolution grating.
- B Redshift from two or more prism emission lines.
- C Redshift from the continuum, or from the continuum and a single prism emission line.
- D Tentative, from visual inspection.
- E No redshift.

Note that the first three flags are the same as in B23.

The combined redshift distribution of the sample is shown in Figure 9, color-coded by flag. There is a drop in the distribution at $z_{\text{Spec}} \sim 7.5$, which reflects at least in part a similar dearth of targets in the distribution of photometric redshifts of the targets selected for observation. The overall distribution of the spectroscopic

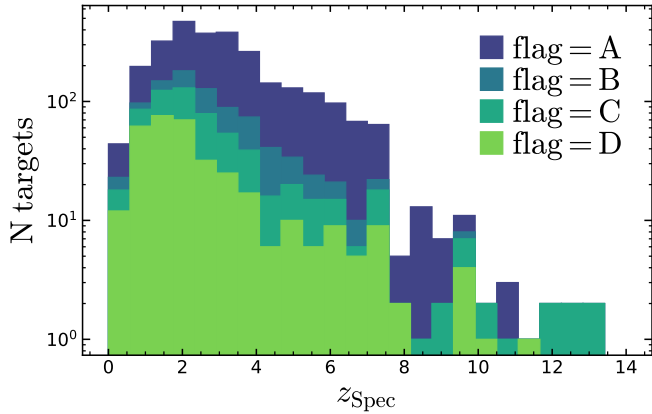


Figure 9. Redshift distribution of the sample, color-coded by the final redshift flag (Section 9). We note a drop in redshift distribution at $z_{\text{Spec}} \sim 7.5$; this reflects a similar drop in the distribution of photometric redshifts of the targets selected for observation.

sample vs magnitude is displayed in Figure 10 (we show only targets with flag A–C, and with a secure match in NIRCcam). The effect of the cosmic evolution of the luminosity function is clearly visible. There is a lack of galaxies fainter than 29 mag at redshifts lower than $z_{\text{Spec}} \lesssim 2$ and higher than $z_{\text{Spec}} \gtrsim 9.5$; this is caused by both sample selection and sensitivity as follows. At low redshifts, NIRCcam photometry becomes less able to clearly distinguish line excesses, because the spacing of strong emission lines reduces as $1+z$; the lower sensitivity of NIRSspec at wavelengths $\lambda < 1 \mu\text{m}$ compounds the problem. At redshifts higher than $z_{\text{Spec}} \approx 9.5$, instead, the strongest emission lines ($[\text{O III}]\lambda\lambda 4959, 5007$) are redshifted out of the NIRSspec coverage, so redshifts measurements rest solely on the Ly α drop and on less prominent lines – both of which are harder to detect in faint targets.

In Figure 11 we show M_{UV} vs redshift, for the sample where magnitudes could be measured directly from the NIRSspec data; to this end, we used a nominal top-hat filter between rest-frame 1,400 and 1,600 Å. The resulting magnitudes were corrected for aperture effects upscaling by the ratio between the observed and synthetic magnitude in the NIRCcam band nearest in wavelength. The color coding is the equivalent width of $\text{H}\alpha + [\text{N II}]\lambda\lambda 6549, 6584$, measured directly on the prism data. There are clear trends of EW with both M_{UV} at fixed redshift and with redshift at fixed M_{UV} ; the first trend arises from the sub-linear slope of the star-forming main sequence, where galaxies have lower specific star-formation rate with increasing stellar mass. The second trend follows the decreasing normalization of the star-forming sequence with increasing cosmic time.

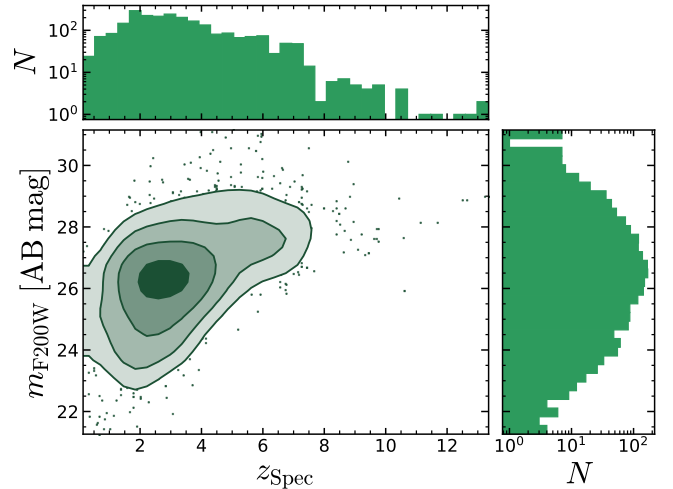


Figure 10. Redshift vs magnitude distribution of the sample; NIRSspec deep spectroscopy can measure redshifts for targets fainter than 30 mag.

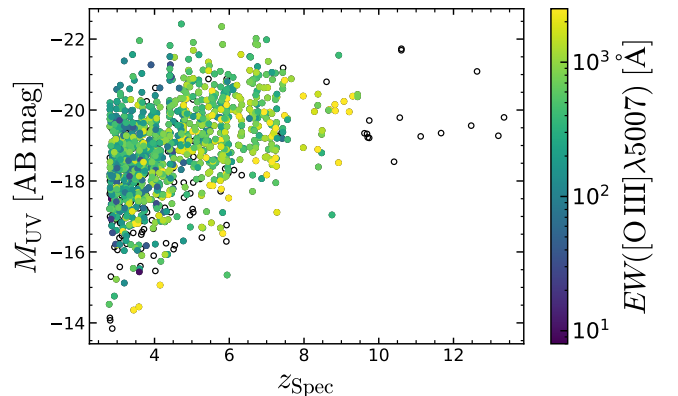


Figure 11. Redshift vs UV magnitude distribution of the sample, color-coded by the equivalent width of $[\text{O III}]\lambda 5007$. Magnitudes were calculated directly from the prism spectra, using aperture corrections estimated by comparing the prism magnitude to the 0.35-arcsec NIRCcam magnitude in the filter nearest to rest-frame 1,500 Å. $[\text{O III}]\lambda 5007$ falls outside of the NIRSspec wavelength range at $z \gtrsim 9.5$.

9.2. Flux comparison: prism vs medium gratings

In Figure 12 we compare the flux measurements from the medium gratings to the corresponding measurements from the prism; the top, middle and bottom rows show respectively $[\text{O II}]\lambda\lambda 3726, 3729$, $[\text{O III}]\lambda\lambda 4959, 5007$ and $\text{H}\alpha + [\text{N II}]\lambda\lambda 6549, 6584$. For $[\text{O III}]\lambda\lambda 4959, 5007$, we consider only galaxies at $z > 2$, wherein the prism catalog the doublet is clearly separated from $\text{H}\beta$; for $\text{H}\alpha + [\text{N II}]\lambda\lambda 6549, 6584$, we take the grating measurements of $\text{H}\alpha$ and $[\text{N II}]\lambda 6584$ and add them, upscaling $[\text{N II}]\lambda 6584$ by 1.34 to take into account $[\text{N II}]\lambda 6548$. For each set of emission lines, we consider the ratio $f_{\text{rat}} \equiv F_{\text{gratings}}/F_{\text{prism}}$, and study this value as a func-

tion of F_{prism} (left column) and redshift; due to the requirement to have both prism and medium-grating measurements, redshift is always z_{gratings} .

For [O II] $\lambda\lambda$ 3726,3729, we find that the grating fluxes are 17 per cent higher than the prism values, with large scatter (25 per cent) and a significant decreasing trend with redshift. We interpret this discrepancy as due to how the continuum is modeled in the prism; in particular, using an incorrect value of the spectral resolution can significantly affect the recovered [O II] $\lambda\lambda$ 3726,3729 flux in the low-resolution regimes found at low redshift.

For [O III] $\lambda\lambda$ 4959,5007, we find good agreement (median ratio 1.01) but a large scatter (albeit smaller than for [O II] $\lambda\lambda$ 3726,3729, 14 per cent). We believe the better agreement is due to the fact that the galaxy continuum around 5,000 Å is relatively featureless, compared to the region of [O II] $\lambda\lambda$ 3726,3729. We find a decreasing trend with F_{prism} (panel b) and an increasing trend with z_{grating} (panel d). A partial-correlation analysis confirms that the redshift correlation is the main one, and that the flux correlation arises from the anti-correlation between flux and redshift. The fact that the ratio increases with redshift is in agreement with the findings of Figure 5, where it seems that the flux discrepancy between the prism and medium-resolution gratings is smallest in G140M and highest in G395M.

Finally, panels c and f show H α + [N II] $\lambda\lambda$ 6549,6584; the results here are consistent with what found for [O III] $\lambda\lambda$ 4959,5007. The significant correlation between f_{rat} and flux is driven by the outliers at $F_{\text{prism}} > 60 \times 10^{-18} \text{ erg s}^{-1} \text{ cm}^{-2}$; removing these points also removes the correlation.

Figure 12 shows jumps in f_{rat} at certain values of z_{grating} ; for example, in Figure 12e these jumps happen at $z_{\text{grating}} \approx 2.5$ and 4.7, which correspond to when the observed wavelength of [O III] $\lambda\lambda$ 4959,5007 moves respectively from G140M into G235M, and from G235M into G395M. To estimate the average flux calibration offset in our data, we divide the sample in three redshift bins, determined by when [O III] $\lambda\lambda$ 4959,5007 (our brightest line on average) is observed with G140M, G235M or G395M (respectively, $0 < z_{\text{grating}} < 2.5$, $2.5 < z_{\text{grating}} < 4.7$ and $z_{\text{grating}} > 4.7$). In these bins, we find an *average* value of f_{rat} of 0.90 ± 0.03 , 1.00 ± 0.01 , and 1.10 ± 0.02 . However, the scatter is large, and galaxies with a clearly detected continuum (e.g., Figs. 5 and 16) show that the flux-calibration mismatch is wavelength dependent. We did not find statistical evidence for a dependence of f_{rat} on the target location on the MSA.

To further investigate this discrepancy between the medium gratings and prism we compared the fluxes of emission lines that are observed in two different grat-

ings. This occurs for lines in the region of the spectrum probed by two configurations simultaneously; i.e. $1.6 \lesssim \lambda \lesssim 1.8 \mu\text{m}$ for G140M/F070LP and G235M/F170LP, and $2.9 \lesssim \lambda \lesssim 3.1 \mu\text{m}$ for G235M/F170LP and G395M/F290LP. We find that the average flux ratios are $f_{\text{G140M/G235M}} = 1.07 \pm 0.01$ and $f_{\text{G395M/G235M}} = 1.01 \pm 0.01$. These results seem to contradict the findings from comparing the emission-line fluxes from the gratings to the prism (where G140M is lower than the prism, G235M is consistent, and G395M is higher than the prism; Figure 12). However, this analysis focuses on a specific region of the wavelength range, where two gratings overlap, whereas the emission-line comparison spans the entire wavelength range of NIRSspec. As shown in Figure 5, the flux-calibration bias between the prism and G395M seems to be wavelength-dependent.

9.3. Accuracy of the wavelength calibration

To assess the accuracy of the wavelength calibration, we use the metric Δv ; for each target, $\Delta v \equiv v(1 < \lambda < 2 \mu\text{m}) - v(\lambda > 3 \mu\text{m})$, where $v(1 < \lambda < 2 \mu\text{m})$ is the mean velocity of emission lines with observed wavelengths between 1 and 2 μm , and $v(\lambda > 3 \mu\text{m})$ is the mean velocity of emission lines with observed wavelengths between 3 μm and the maximum wavelength. For this test, we consider only galaxies with more than three independent emission lines having $S/N > 7$. In Figure 13 we show Δv as a function of the intra-shutter source positions, δx (closely aligned along the dispersion direction) and δy ; the gray dots are individual galaxies, the green line with bands is a robust least-squares fit (Cappellari et al. 2013). For an unbiased solution, both the zero-point and slope of the best-fit line should be zero. In contrast, we find an average zero-point offset of 300 km s^{-1} (for the prism) and 30 km s^{-1} (for the gratings); these values correspond to 0.1–1 pixels (prism) to 0.1–0.3 pixels (medium gratings). These offsets indicate an overall bias of the wavelength solution. In addition to this zero-point offset, there is also a clear negative correlation between Δv and δx for both prism and gratings. The correlation for the prism is both stronger and more statistically significant, reaching an excursion of 0.5–3 pixels. Before interpreting these correlations, we remark that the coordinates of the MSA are opposite to the pixel coordinates of the detector on the focal plane assembly (see Ferruit et al. 2022, their Figure 4; and Jakobsen et al. 2022, their Figure 4); this means that positive δx are offset toward bluer wavelength values. With this in mind, the anti-correlation we find means that the correction to the wavelength solution due to intra-shutter offsets of compact sources (Section 5 and Ferruit et al. 2022) is insufficient. A solution to these remaining calibration

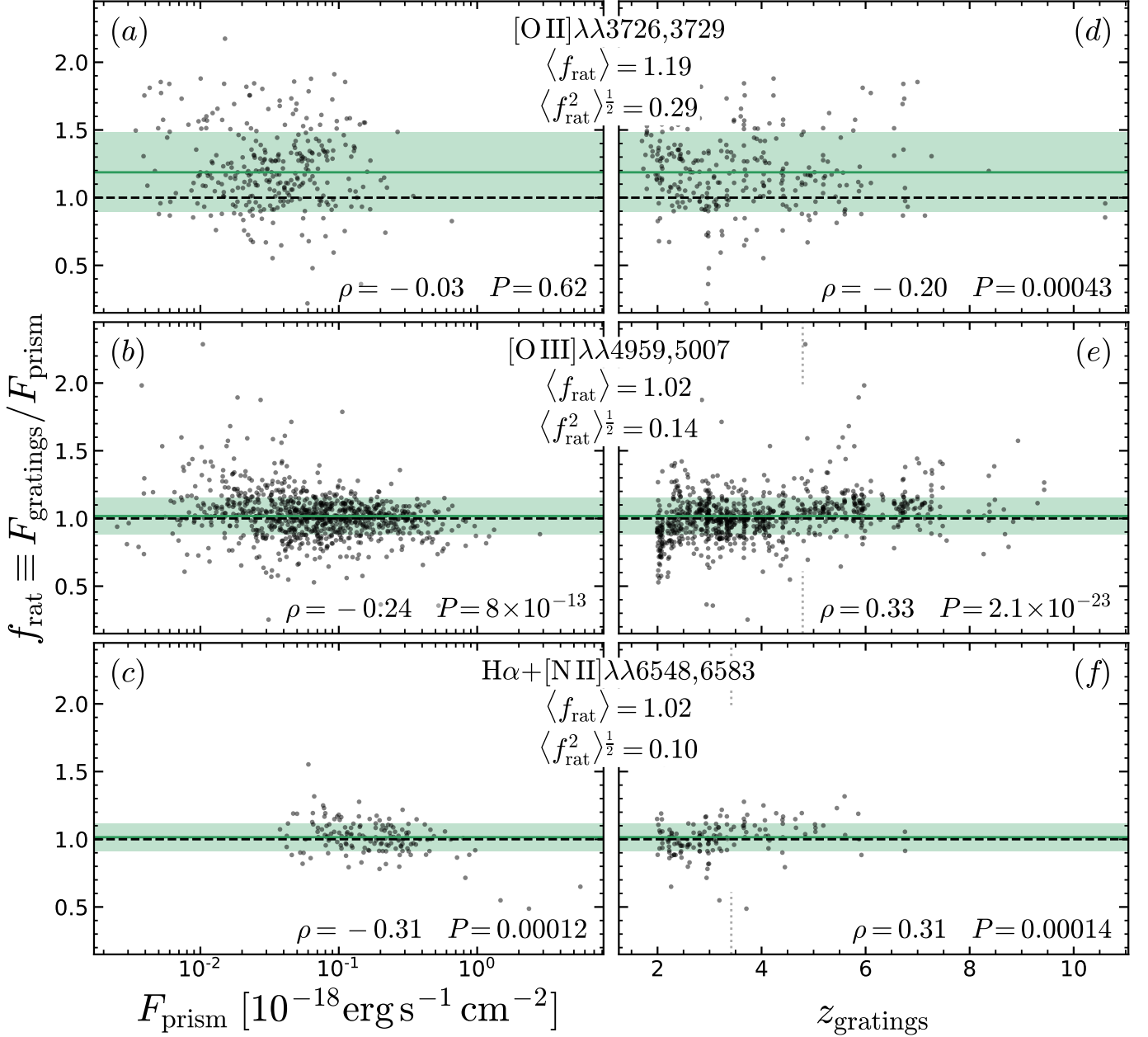


Figure 12. Comparison of the emission-line fluxes measured from the prism and from the medium-resolution gratings, as a function of prism flux (left column) and redshift (right column). The central inset between the columns are the median and standard deviation for each emission-line complex (also displayed as green horizontal lines and shaded regions), while the bottom right corner of each panel reports the Spearman rank correlation coefficient and associated p-value. [O II] $\lambda\lambda 3726, 3729$ (panels a and d) shows the regime where the gratings-to-prism flux ratio f_{rat} is dominated by systematics in the continuum model; [O III] $\lambda\lambda 4959, 5007$ (panels b and e) illustrates with high significance the strong correlation between f_{rat} and redshift, which indicates the flux-calibration mismatch between prism and gratings is most severe in G395M. The dotted vertical lines in panels (e) and (f) show the redshift where [O III] $\lambda 5007$ and H α are observed at $2.9 \mu\text{m}$ —the bluest wavelength captured by the G395M/F290LP disperser/filter combination. Finally, H α + [N II] $\lambda\lambda 6549, 6584$ shows that the total fluxes measured in the prism (where we do not separate H α from [N II] $\lambda\lambda 6549, 6584$) match well the fluxes measured in the gratings (where the emission-line complex is well resolved); the trends with flux and redshift are consistent with what we see for [O III] $\lambda\lambda 4959, 5007$.

issues is beyond the time constraints of this data release, and will be presented in a future work. In Appendix C we further show that on average the wavelength bias of the prism depends on the global position of the source in the MSA.

10. USING THE NIRSPEC DATA PRODUCTS

In this section, we provide a concise summary on how to use the data products, and a list of the limitations of the current data release. The prospective user of the data provided in this release is encouraged to consider these limitations carefully.

- **Data reduction problems and short circuits.**

Spectra with data reduction problems are flagged with `DR_flag=True`; if a redshift was given, it is guaranteed to be accurate from visual inspection. However, for any purpose other than redshift, these data should be visually inspected to assess whether they are suitable. Under this flag we also collect observations affected by MSA short circuits, which may present abnormally bright background, including steep background gradients across the detector. In all cases, this results in lower signal-to-noise spectra than one would expect given the source magnitudes and integration time. In the most severe cases, shorts cause incorrect background subtraction and no useful observations (Section 3, Appendix A).

- **Aperture correction.**

Aperture corrections assume the target has point-source geometry; for extended sources, this implies both the total flux and the color of the spectrum are inaccurate. For calculating emission-line ratios over long wavelength separations (e.g., $H\alpha/H\beta$, $[O III]\lambda 5007/[O II]\lambda\lambda 3726, 3729$, $Pa\alpha/H\alpha$), we recommend using aperture corrections derived from the photometry. Sources more extended than one shutter should be considered with particular care, or even excluded (see Background subtraction).

- **Background subtraction.**

The background subtraction strategy is optimized for compact sources; while shutters affected by contaminants are pre-identified and not considered in the subtraction, shutters affected by the same source cause self subtraction. Depending on the source size and spatial gradients, this may bias the shape of the spectrum and the total flux.

- **Noise spectrum.**

The noise spectrum is based on variance-conserving resampling, to mitigate the effect of correlated noise (Dorner 2012). A full analysis of correlated noise in NIRSpec will be presented in a future work (P. Jakobsen, in prep.)

- **Wavelength calibration.** There is a discrepancy between the wavelength calibration of the prism and gratings (causing a typical $\Delta z = 0.0042$; Figure 8). In addition, we find an overall offset in the wavelength calibration of both the prism (mean value 300 km s^{-1}) and for the gratings (mean value 30 km s^{-1}). We apply a correction for the wavelength offset due to the intra-shutter position of each source, but there is still a residual bias. After correcting empirically for this bias, we show that the prism wavelength offset depends on the spatial location in the MSA (Section 9.3 and Appendix C); for the medium gratings the residual wavelength dependence on the intra-shutter position is milder, and we find no detectable trend with spatial location on the MSA.
- **Flux calibration.** The relative flux calibration between the prism and gratings is accurate to within 15 per cent, and depends on the wavelength (e.g., figures 5, 16, 12). The user is encouraged to consider this problem when measuring flux ratios, particularly when comparing between different dispersers and wavelengths.

11. HIGHLIGHTS

The diversity of the JADES DR3 spectroscopic sample is illustrated by comparing some highlights (Figs. 14–20). In Figure 14 we show 200733, an example of a low-redshift quiescent galaxy at $z = 2.86$. NIRC*am* photometry (panel a) indicates a smooth, peaked light profile with an extended halo, suggesting a high ($n \gtrsim 2$) Sérsic index and, therefore, a dynamically evolved system. The 1-d spectrum (panel c) displays the signatures of an evolved stellar population, with a distinct 4000-Å break – typical of old (> 1.5 Gyr), metal-rich stellar populations, accompanied by a possible, fainter Balmer break (≈ 3750 Å), indicating a younger (0.5–1 Gyr old) stellar population. The galaxy displays a number of stellar absorption features with high equivalent width; the Balmer series, $Mg \text{ i}\lambda\lambda 5167\text{--}5184$, and the ‘calcium triplet’, $Ca \text{ II}\lambda\lambda 8498\text{--}8662$.

At slightly higher redshift ($z = 2.95$) we find 1000721 (Figure 15), an AGN-host galaxy with type-1 AGN and high-velocity outflows, a secure signature of an active supermassive black hole. The host galaxy is clearly seen in NIRC*am*; the lack of flux in F090W (cf. Figure 14a) indicates high dust reddening, which is indeed seen in the NIRSpec data (panel c). Emission from the $[O III]\lambda\lambda 4959, 5007$ and $H\alpha + [N II]\lambda\lambda 6549, 6584$ complexes is spatially extended (panel b), indicating a resolved disc or narrow-line region. In the medium-resolution grating spectra (blue line in panel c) the presence of

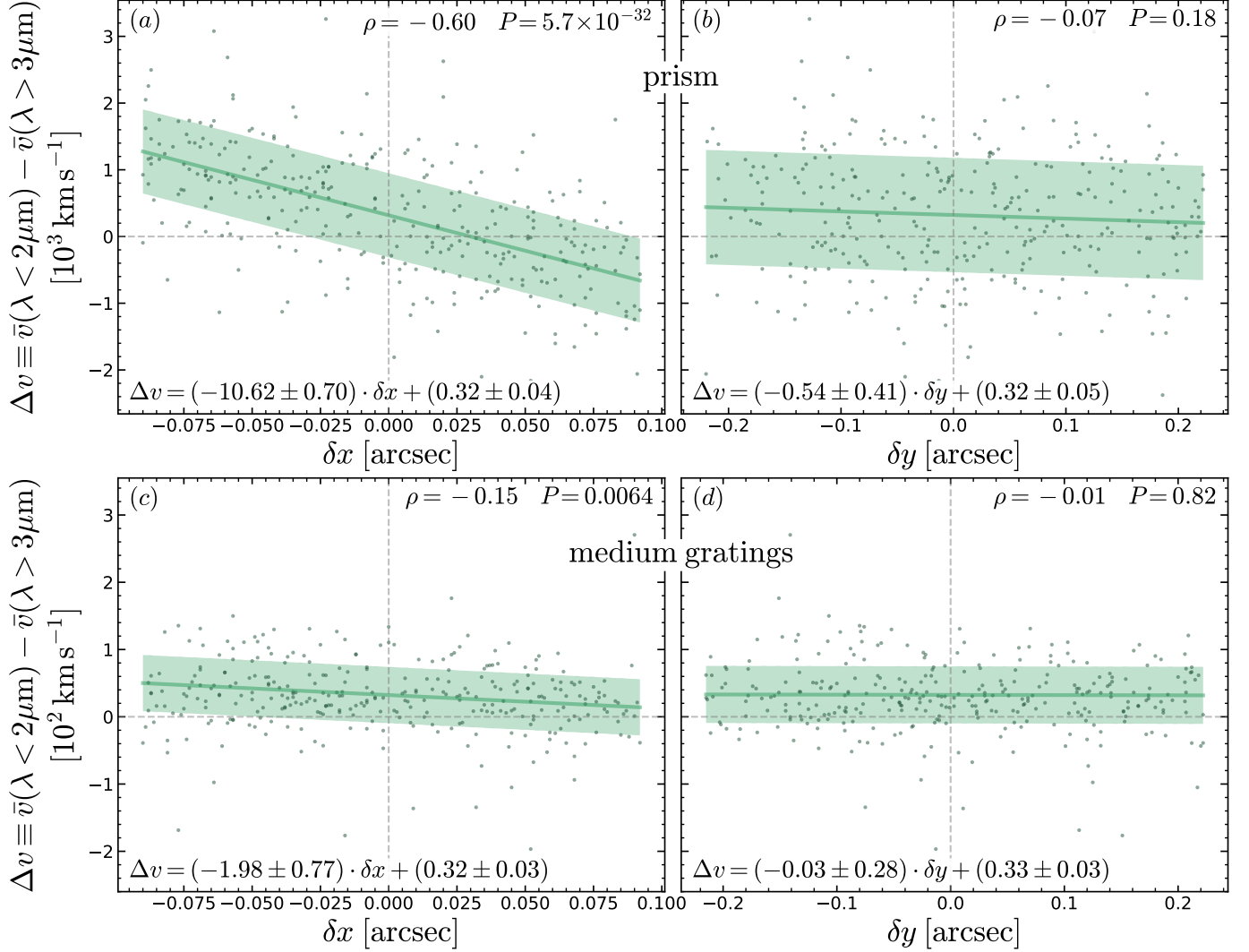


Figure 13. Wavelength calibration bias as a function of intra-shutter source position; for both the prism (top) and medium gratings (bottom). δx is the spatial offset of the target with respect to the center of the micro shutter, measured along the dispersion direction. For an unbiased wavelength solution, we would expect $\Delta v = 0$ at $\delta x = 0$ and $\delta y = 0$, and no correlation. The observed correlation with δx means that the correction we adopted for the intra-shutter source position is insufficient (see Section 5 and Ferruit et al. 2022); δx increases toward bluer wavelengths. Neglecting intra-shutter source position entirely would result in an even larger bias than what reported here.

an outflow can be clearly seen in $[\text{O III}]\lambda\lambda 4959, 5007$ and $[\text{S II}]\lambda\lambda 6717, 6730$, while $\text{H}\alpha$ shows evidence of both ionized gas outflows and a broad line region. The prism spectrum (black line) reveals a Balmer break, indicating that the continuum emission is dominated by stars; a number of auroral lines is readily detected in rest-frame r - and Y -bands.

‘Pablo’s Galaxy’ (197911, GS-10578; Fig 16) is a marvelous massive galaxy at $z = 3.06$, identified as quiescent via the UVJ color-color diagram (Williams et al. 2009). This extraordinary galaxy displays stellar rotation (D’Eugenio et al. 2023a), an X-ray and MIR-detected type-2 AGN (Circosta et al. 2019), fast ionized-gas outflows in $[\text{O III}]\lambda 5007$, and neutral-gas outflows

with high mass loading ($\text{Na I}\lambda\lambda 5890, 5896$ absorption in panel c; D’Eugenio et al. 2023a). Medium-resolution observations spanning the entire NIRSpect wavelength enable the study of $\text{Mg II}\lambda\lambda 2796, 2803$ emission and absorption, high-ionization species ($[\text{Ne V}]\lambda\lambda 3346, 3426$), electron densities ($[\text{O II}]\lambda\lambda 3726, 3729$ and $[\text{S II}]\lambda\lambda 6717, 6730$), and stellar α -elements abundance ($\text{Mg I}\lambda\lambda 5167\text{--}5184$, $\text{Ca I}\lambda\lambda 8498\text{--}8662$). Stringent upper limits on $\text{Pa}\beta$ disfavor a dust-obscured starburst.

1080660 is an example of a higher-redshift quiescent galaxy at $z = 4.4$ (Figure 17), among the highest-redshift quiescent galaxies known (cf. Carnall et al. 2023; Nanayakkara et al. 2022). NIRCam (panel a) shows two interlopers (north west; photometric red-

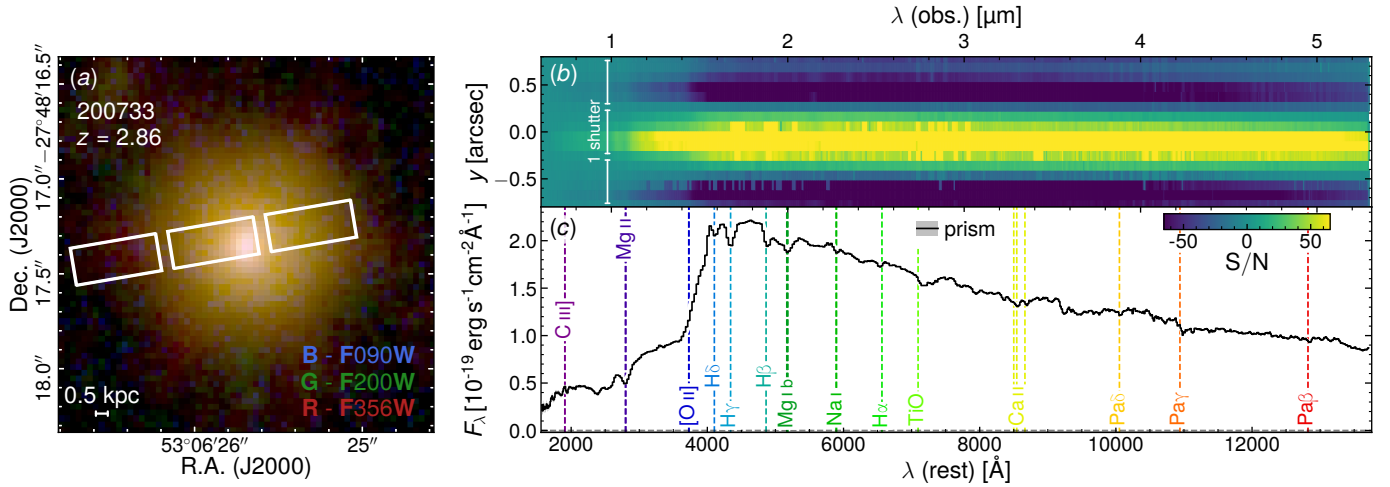


Figure 14. A low-redshift quiescent galaxy, displaying a smooth, peaked light distribution and an evolved stellar population. Panel (a) shows a false-color NIRCcam image, with the adopted filters in the bottom right corner. Panel (b) is the NIRSpc/MSA 2-d signal-to-noise map of the prism spectrum; three shutters are indicated. Here and in all other 2-d maps (Figs. 15b–20b), negative signal-to-noise is caused by the nod-and-subtract strategy for removing the background. Panel (c) is the 1-d, 5-pixel box-car extracted spectrum. Besides the strong 4000-Å break, several stellar and ISM absorption features are detected. Notice that the aperture correction applied in this data reduction is optimized for point-like sources; extended galaxies like 200733 would require both a different aperture correction and a different background-subtraction strategy, to avoid self subtraction. From Z. Ji et al. (in prep.).

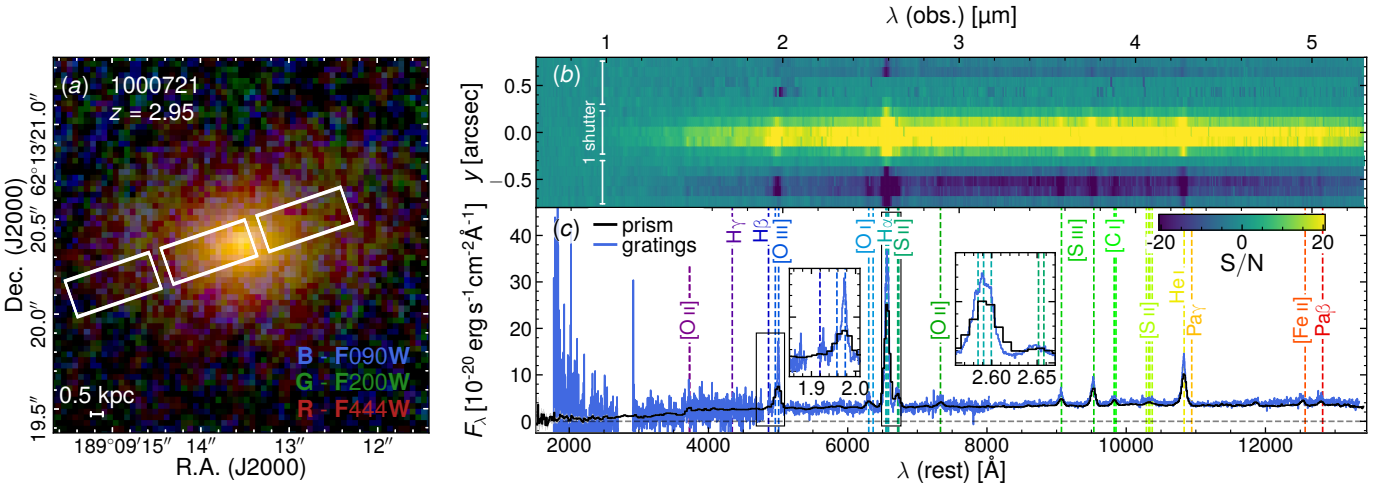


Figure 15. Example of a dust-reddened AGN host, with clear outflows (as seen in the broad component of forbidden [O III] $\lambda\lambda$ 4959,5007, [S II] $\lambda\lambda$ 6717,6730 and [S III] $\lambda\lambda$ 9069,9532), stellar continuum (there is evidence of a Balmer break) and high temperature (from the detection of several auroral lines, [O II] $\lambda\lambda$ 7319–7332 and [S II] $\lambda\lambda$ 10290–10373). The blue line in panel c is the (spliced) medium-resolution grating spectra (gaps are due to the gaps between the NIRSpc detectors). The black rectangles show details of the H β –[O III] $\lambda\lambda$ 4959,5007 and H α –[N II] $\lambda\lambda$ 6549,6584–[S II] $\lambda\lambda$ 6717,6730 emission-line regions. All other symbols are the same as Figure 14.

shift 2.5) and a possible dusty companion to the east (1080661, with photometric redshift 3.8, but this value is highly uncertain due to the dusty nature of this target). 1080660 itself has an evolved morphology, consisting of a bright central core and more extended emission along the north-east–south-west direction; the extended emission appears significantly redder than the core (green vs white in the false-colour image of panel a), suggest-

ing a possible central starburst, as seen in some local post-starburst galaxies (D’Eugenio et al. 2020) and, recently, in NIRCcam imaging (Wright et al. 2023). The spectrum (panel c) exhibits a clear Balmer break, H δ , H γ and H β absorption, and [O III] $\lambda\lambda$ 4959,5007 and H α + [N II] $\lambda\lambda$ 6549,6584 emission of relatively low equivalent width. There is no evidence for spatially extended nebular emission in the 2-d (panel c).

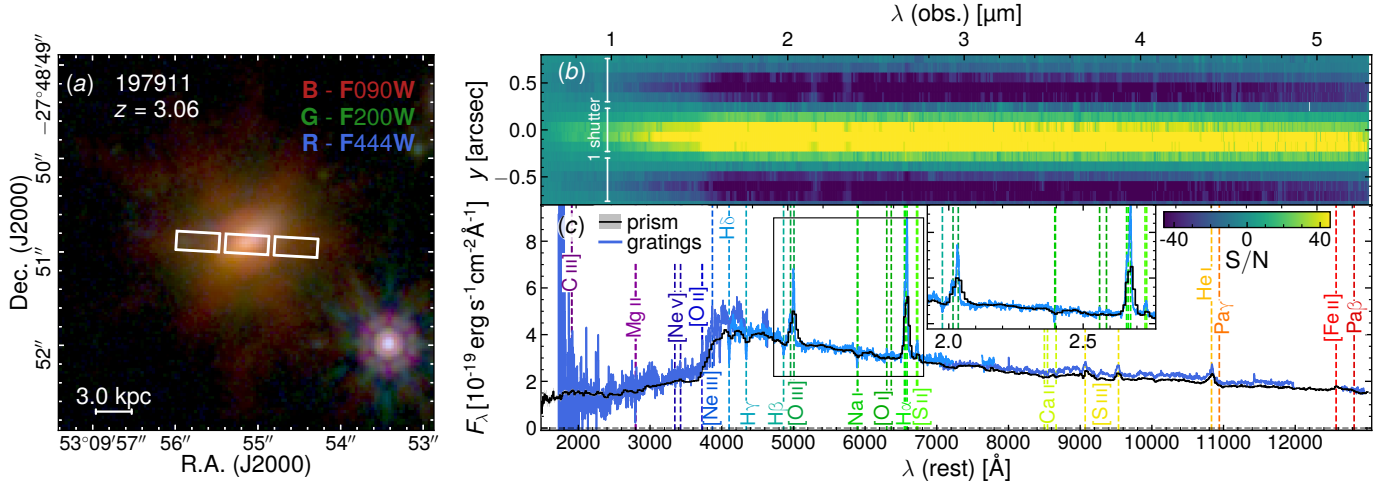


Figure 16. ‘Pablo’s Galaxy’, a UVJ-quiet galaxy at $z = 3$ hosting an X-ray and MIR AGN and multi-phase outflows. This system displays a rich set of stellar and ISM absorption lines (Mg II $\lambda\lambda 2796, 2803$ and Na I $\lambda\lambda 5890, 5896$, the latter tracing a fast neutral-gas outflow; D’Eugenio et al. 2023a). Emission lines trace both low-ionization gas [O II] $\lambda\lambda 3726, 3729$, [O I] $\lambda\lambda 6300, 6363$, [N II] $\lambda\lambda 6549, 6584$, [S II] $\lambda\lambda 6717, 6730$ – possibly due to shocked or stripped gas, as well as higher-ionization species ([Ne V] $\lambda\lambda 3346, 3426$). Note the flux-calibration offset between G140M (blue) and G235M (light blue: 10 per cent) and G235M and G395M (blue; 7 per cent). Like 200733 (Figure 14), Pablo’s galaxy is fairly extended, meaning the standard aperture correction and background subtraction are not optimal. From J. Scholtz et al. (in prep). All symbols are the same as Figure 14.

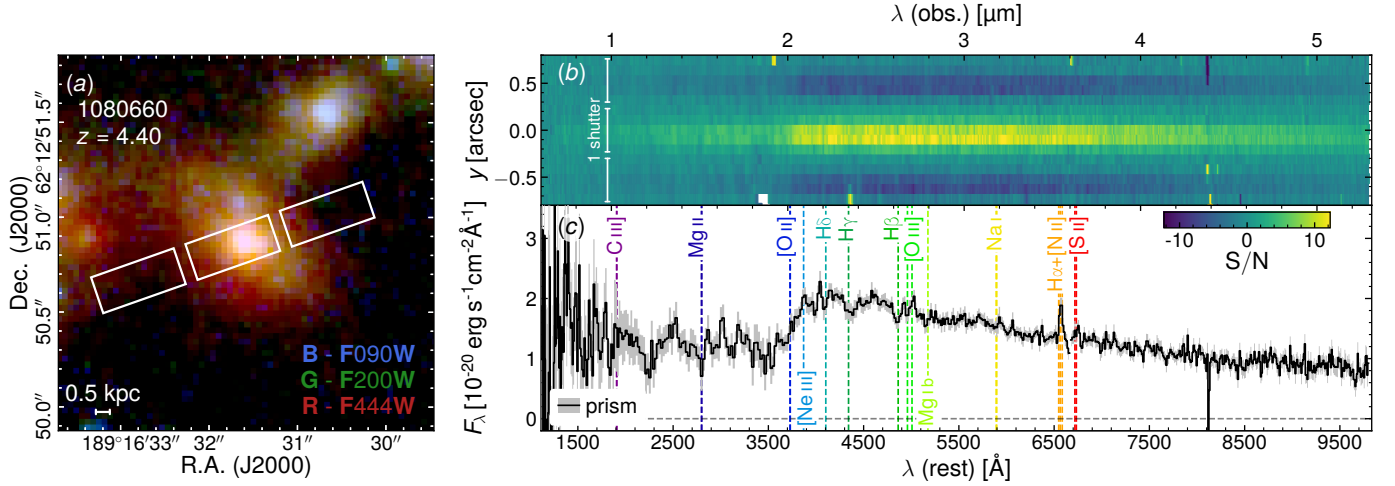


Figure 17. Example of a quiescent galaxy at $z = 4.4$, ID 1080660. This object displays a complex morphology with both a blue core (white in panel a) and a redder extended component (in green). The prominent Balmer break and flat rest-UV spectrum indicate this galaxy is an early quiescent system. We see clear emission from the H α + [N II] $\lambda\lambda 6549, 6584$ blended complex, from [O III] $\lambda\lambda 4959, 5007$, and from Mg II $\lambda\lambda 2796, 2803$, indicating AGN activity and, possibly, ongoing outflows, as seen in quiescent galaxies at lower redshifts. All symbols and panels are the same as Figure 14.

Figure 18 shows 1028761, a merger between a relatively un-obscured galaxy and a dusty galaxy at $z = 6.76$. This system displays high values of the emission-line ratios [O II] $\lambda\lambda 3726, 3729$ /[O III] $\lambda 5007$, [N II] $\lambda 6584$ /H α and [S II] $\lambda\lambda 6717, 6730$ /H α , characteristic of high-metallicity gas or shock-dominated emission.

In Figure 19 we show 99915, which displays a strong single emission line at $4.8 \mu\text{m}$. The line is also seen in the G395M grating spectrum, and in the NIRCcam grism spectrum (F. Sun et al., in prep.), which rules

out an artifact. The galaxy also shows a photometric drop between the NIRCcam F090W and F150W filters, which at face value rules out a solution where the emission line is H α . Identifying the line as either H β or [O III] $\lambda 5007$ would match the Ly α drop seen in NIRCcam, but is not without problems. If the line was H β , we would expect to observe H γ at about half the H β flux; similarly, the tentative solution at $z = 8.69$, which identifies the observed line with [O III] $\lambda 5007$, would require observing [O III] $\lambda 4959$ at about one third of the line flux.

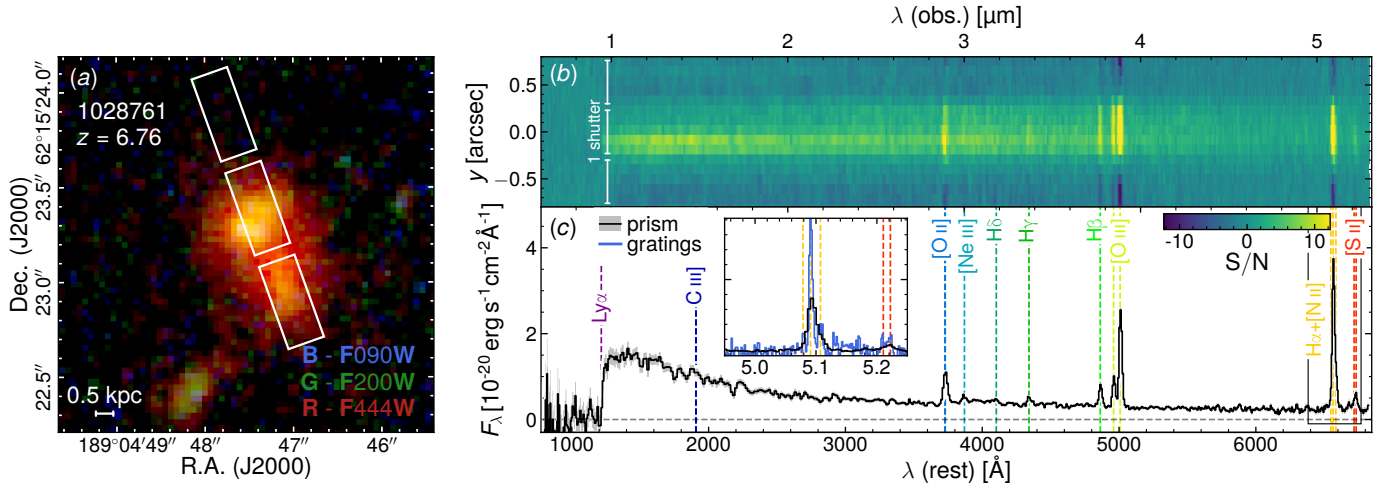


Figure 18. Example of a high-redshift galaxy with high metallicity and/or signatures of shocked gas, ID 1028761. The NIRSpec 2-d signal-to-noise map (panel b) clearly reveals spatially extended emission; a different background subtraction strategy is clearly required for this class of targets; in cases like this, using the provided emission-line fluxes may result in unphysical line ratios, or harder-to-identify bias. From A. Cameron et al. (in prep.). All symbols and panels are the same as Figure 14.

None of these accompanying lines (the putative $H\gamma$ nor $[O\text{ III}]\lambda 4959$) are seen either in prism, grating, or NIRCam grism, leaving this object as a tentative redshift determination.

Finally, in Figure 20 we show JADES-GS-z12-0 (Curtis-Lake et al. 2023; Robertson et al. 2023b), which at the time of this data release is the highest-redshift detection of a metal emission line (D’Eugenio et al. 2023b). The data included in this release consists separately of observations from PID 3215 and PID 1210. In this data release, we use the redshift from D’Eugenio et al. (2023b), based off clearly detected $C\text{ III}]\lambda\lambda 1907,1909$ emission. This value is lower than the redshift reported in our previous articles (Curtis-Lake et al. 2023, Robertson et al. 2023b, B23); the latter was measured from the wavelength of the $Ly\alpha$ drop, assuming only IGM absorption, and the discrepancy with the $C\text{ III}]\lambda\lambda 1907,1909$ redshift is explained by DLA (Damped $Ly\alpha$ absorption; e.g., Wolfe et al. 2005). Increasing evidence is building up that a substantial fraction of $z > 10$ galaxies may have DLA absorption (e.g., Heintz et al. 2023), which may bias photometric and $Ly\alpha$ -drop redshifts to higher values (e.g., D’Eugenio et al. 2023b; see especially Hainline et al. 2024.)

12. CONCLUSIONS

In this work, we presented new and updated JADES NIRCam and NIRSpec observations obtained up until October 2023 in the two GOODS fields. The spectra include both medium-depth and deep observations up to redshift $z \sim 13$, reaching the deepest unlensed spectroscopic observations to date (up to 45 hours on source). The sample size and data quality of the spectra are a testament to the success of the NIRSpec/MSA instru-

ment. The high success rate of the redshift identification validates the selection criteria, including the quality of NIRCam data, the accuracy of the photometric analysis, and the precision of the photometric redshift determination with EAZY and BEAGLE.

We release fully reduced and calibrated images and spectra, and present catalogs of photometry, photometric redshifts, spectroscopic redshifts, and emission-line fluxes. Insight from this large sample enabled us to pin down some remaining challenges in the data reduction: a mismatch in the redshift and flux-calibration between different dispersers, background subtraction and slit-loss corrections appropriate for extended sources, and residual wavelength calibration issues. Future calibration programs will certainly address these problems. An additional challenge is deriving an accurate selection function for correctly weighting each galaxy, which we will provide in the next data release.

In the future, significantly larger samples of the general galaxy population in the redshift and mass range probed by JADES would require a substantial investment of *JWST* time, or a revised observing strategy. Larger samples of specific classes of objects will still be crucial for understanding rare types, where JADES has only hinted at the potential (e.g., high-redshift quiescent galaxies, extremely reddened galaxies, little red dots, $z > 8$ $Ly\alpha$ emitters).

In the meantime, the current sample is the largest extragalactic sample with low- and medium-resolution spectroscopy spanning 0.6–5.3 μm ; the depth of the medium and deep spectra, and the synergy with medium- and wide-band imaging, enables for the first time a statistical study combining morphology and rest-

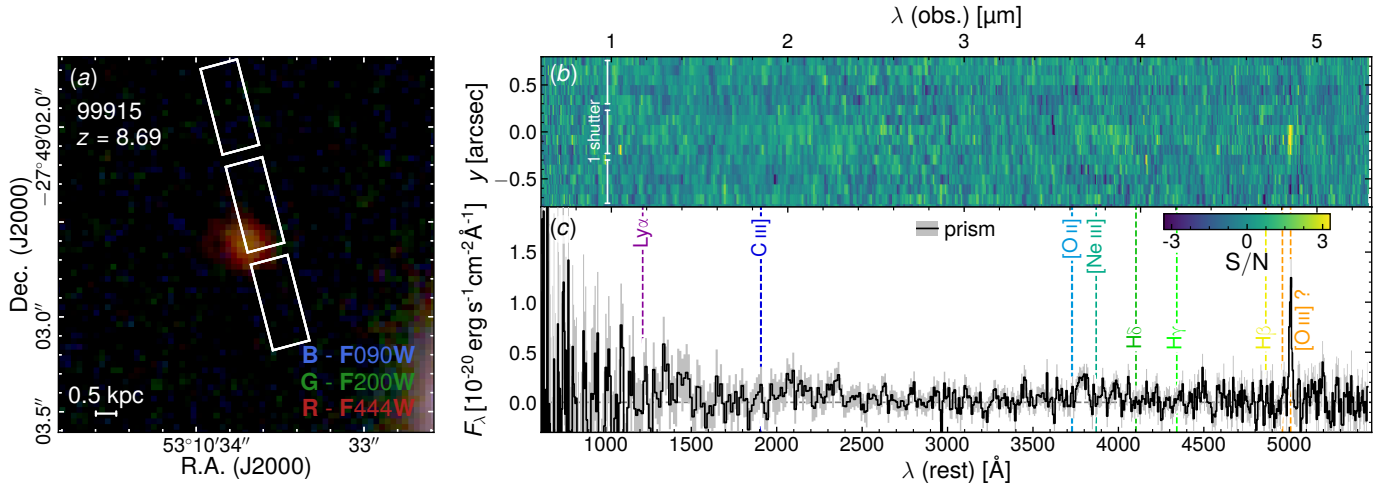


Figure 19. Example of a high-redshift galaxy with uncertain redshift, ID 36424. The clear emission line at 4.8 μm could be identified as $\text{H}\alpha$, but this would be inconsistent with the photometric break between F090W and F115W. A tentative identification of the line as $[\text{O III}]\lambda 5007$ is presented here; while consistent with the photometric break, this solution is itself problematic due to the missing $[\text{O III}]\lambda 4959$. We can rule out an artifact, because the line is also detected in our G395M spectrum and in the NIRCam grism (from FRESKO; Oesch et al. 2023a; see also F. Sun et al., in prep.). All symbols and panels are the same as Figure 14.

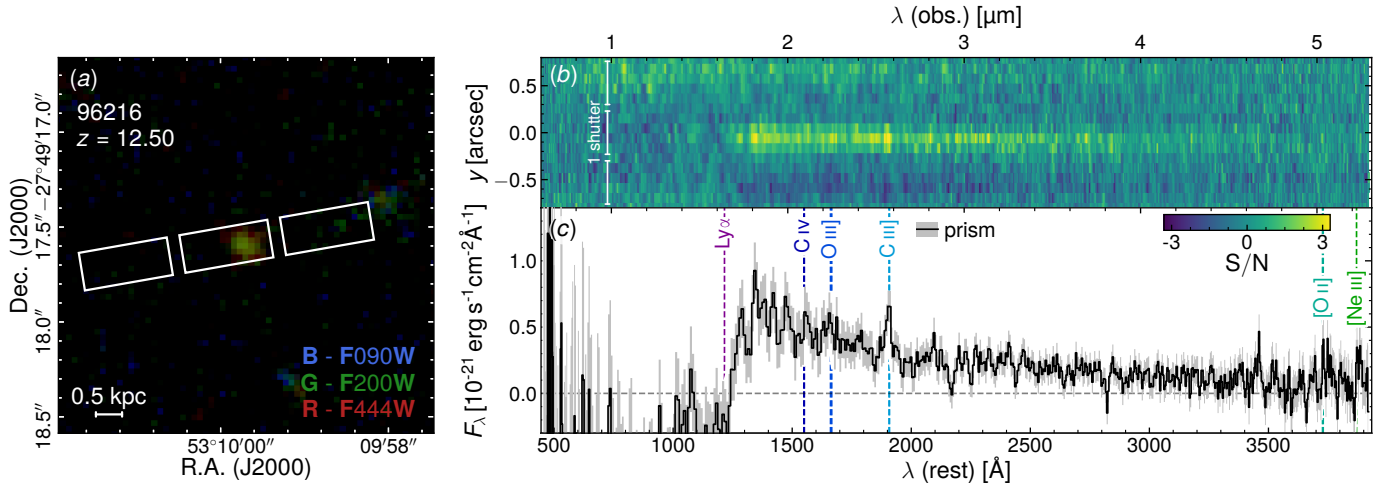


Figure 20. One of the highest-redshift sources in this data release, 96216 (JADES-GS-z12-0, Curtis-Lake et al. 2023; Robertson et al. 2023b; 2773, B23). This system shows the highest-redshift detection of metals to date (D’Eugenio et al. 2023b). All symbols and panels are the same as Figure 14.

frame optical spectroscopy of galaxies between the peak of the star-formation rate density and the first few hundred Myr after the Big Bang.

FDE, JS, RM, TJL, JW, WMB, XJ, IJ and CS acknowledge support by the Science and Technology Facilities Council (STFC), by the ERC through Advanced Grant 695671 “QUENCH”, and by the UKRI Frontier Research grant RISEandFALL. RM also acknowledges funding from a research professorship from the Royal Society. AJC, AJB, JC, AS and GCJ acknowledge funding from the “FirstGalaxies” Advanced Grant from the European Research Council (ERC) un-

der the European Union’s Horizon 2020 research and innovation programme (Grant agreement No. 789056) SC, EP and GV acknowledge support by European Union’s HE ERC Starting Grant No. 101040227 - WINGS. ECL acknowledges support of an STFC Webb Fellowship (ST/W001438/1). SA, BRP and MP acknowledge support from Grant PID2021-127718NB-I00 funded by the Spanish Ministry of Science and Innovation/State Agency of Research (MICIN/AEI/10.13039/501100011033). MP also acknowledges support from the Programa Atracción de Talento de la Comunidad de Madrid via grant 2018-T2/TIC-11715. CNAW, BER, BDJ, DJE, PAC, EE, MJR and FS ac-

knowledge JWST/NIRCam contract to the University of Arizona NAS5-02015. BER also acknowledges support from the JWST Program 3215. DJE is supported as a Simons Investigator. The Cosmic Dawn Center (DAWN) is funded by the Danish National Research Foundation under grant DNR140. ST acknowledges support by the Royal Society Research Grant G125142. HÜ gratefully acknowledges support by the Isaac Newton Trust and by the Kavli Foundation through a Newton-Kavli Junior Fellowship. This research is supported in part by the Australian Research Council Centre of Excellence for All Sky Astrophysics in 3 Dimensions (ASTRO 3D), through project number CE170100013. ALD thanks the University of Cambridge Harding Distinguished Postgraduate Scholars Programme and Technology Facilities Council (STFC) Center for Doctoral Training (CDT) in Data intensive science at the University of Cambridge (STFC grant number 2742605) for a PhD studentship. Funding for this research was provided by the Johns Hopkins University, Institute for Data Intensive Engineering and Science (IDIES). PGP-G acknowledges support from grant PID2022-139567NB-I00 funded by Spanish Ministerio de Ciencia e Innovación MCIN/AEI/10.13039/501100011033, FEDER, UE. DP acknowledges support by the Huo Family Foundation through a P.C. Ho PhD Studentship. MSS acknowledges support by the Science and Technology Facilities Council (STFC) grant ST/V506709/1. RS acknowledges support from a STFC Ernest Rutherford Fellowship (ST/S004831/1). NCV acknowledges support

from the Charles and Julia Henry Fund through the Henry Fellowship. The research of CCW is supported by NOIRLab, which is managed by the Association of Universities for Research in Astronomy (AURA) under a cooperative agreement with the National Science Foundation. This work was performed using resources provided by the Cambridge Service for Data Driven Discovery (CSD3) operated by the University of Cambridge Research Computing Service (www.csd3.cam.ac.uk), provided by Dell EMC and Intel using Tier-2 funding from the Engineering and Physical Sciences Research Council (capital grant EP/T022159/1), and DiRAC funding from the Science and Technology Facilities Council (www.dirac.ac.uk) The authors acknowledge use of the lux supercomputer at UC Santa Cruz, funded by NSF MRI grant AST 1828315. This study made use of the Prospero high performance computing facility at Liverpool John Moores University.

Facilities: *JWST* (NIRCam), *JWST* (NIRSpec/MSA), *HST* (ACS), *HST* (WFC3) [10.17909/8tdj-8n28](https://doi.org/10.17909/8tdj-8n28).

Software: `astropy` (Astropy Collaboration et al. 2013), `corner` (Foreman-Mackey 2016), `ds9` (Joye & Mandel 2003), `emcee` (Foreman-Mackey et al. 2013), `fitsmap` (Hausen & Robertson 2022), `fsps` (Conroy et al. 2009; Conroy & Gunn 2010), `ltsfit` (Cappellari et al. 2013), `matplotlib` (Hunter 2007), `numpy` (Harris et al. 2020), `ppxf` (Cappellari 2017, 2023), `scipy` (Jones et al. 2001), `smpplib` (Li 2023), and `topcat` (Taylor 2005).

APPENDIX

A. OBSERVATIONS AFFECTED BY MSA SHORT CIRCUITS

Some observations in this data release were affected by MSA short circuits, or ‘shorts’. For most programs, these were only a minority, and were excluded from the data reduction (e.g., PID 3215, Section 3.6). However, for PID 1180 shorts affected two thirds of the initial observations. The brightness of the shorts emission can vary drastically between occurrences: the brightest can render the entire integration unusable (Figure 21), while the faintest may contaminate only a few sources near the affected region of the field of view.

As we argued in Section 3.2, these shorts-contaminated data are still useful to measure redshifts, and are included in this data release (Figure 22).

There are three major ways in which shorts affect the quality of the data. First, shorts increase the background level, reducing the signal-to-noise of the observations. Second, the shorts’ background is tied to a given exposure, and, therefore can vary between different sky and nod positions; this causes our background subtraction to fail, because our strategy assumes the same background between different nods. Third, the combination of increased and varying background affects subsequent steps of the pipeline, which can cause excessive or insufficient outlier removal. Users are encouraged to treat these observations with caution, particularly for measurements using the spectral continuum. The flag `DR_flag` in the published tables identifies all spectra where there is a problem in the data reduction, or where the observations were affected by shorts (including when the actual contamination is low).

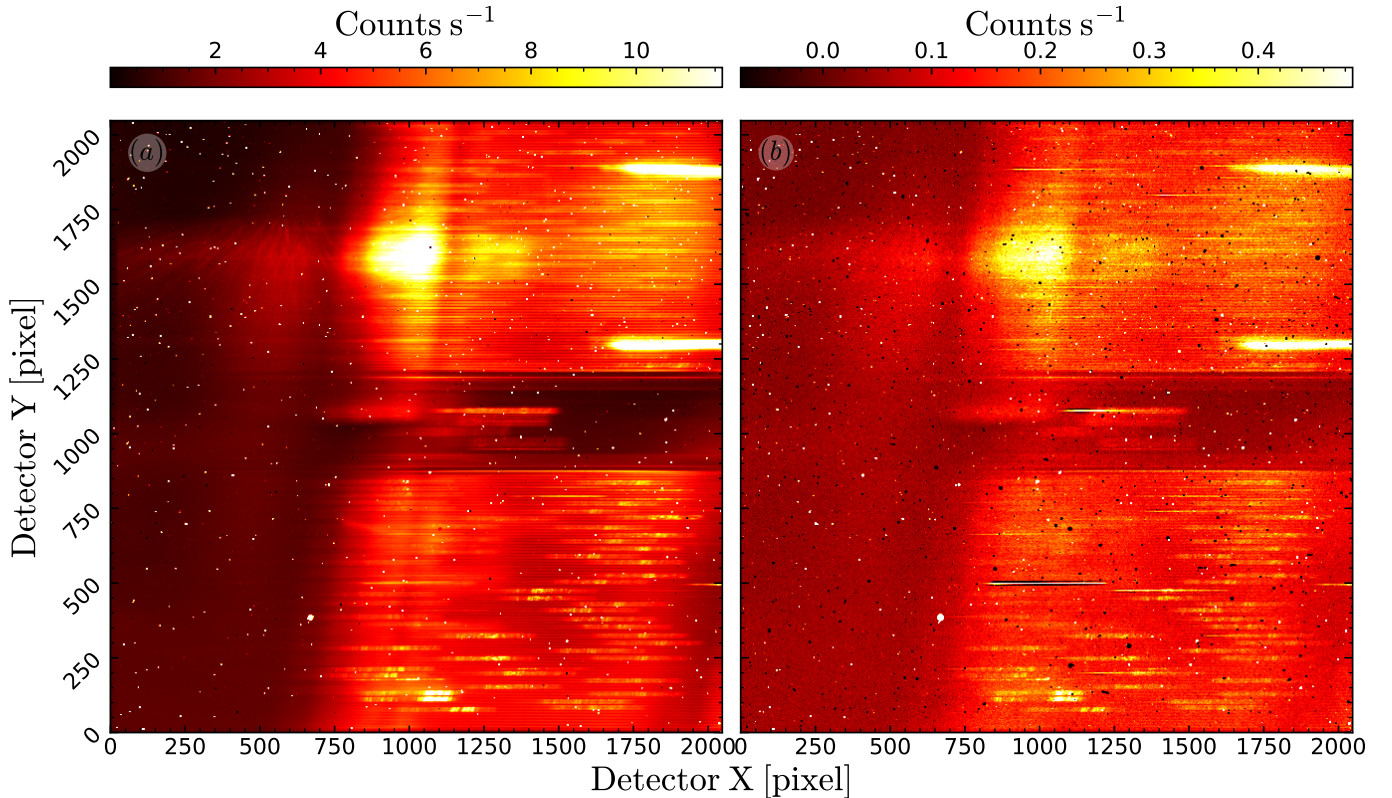


Figure 21. Imaging count-rate maps from NIRS1 detector NRS1 carried out during one of the visit of program PID 1180. Left and right panels illustrate the effect of the short circuits on the count-rate maps before (left) and after (right) background subtraction.

B. COMPARISON WITH DR1

In this section, we compare the measurements obtained by applying the algorithms used in this data release (DR3), to the data previously released in DR1 (B23). We remark that NIRS1 DR1 and DR3 use the same data reduction, hence the spectra are exactly the same as in B23. In Figure 23 we compare the flux (top rows) and uncertainties (bottom rows) between DR3 and DR1. We find excellent agreement for the overall flux measurements, even though some bright lines ($F > 10^{-18}$ erg s $^{-1}$ cm $^{-2}$, panel a) display highly significant differences.

Unlike for flux, the measurement uncertainties from DR3 and DR1 are different, with the present values 3 per cent smaller. We find a statistically significant trend with flux, suggesting the mismatch in the uncertainties is due to systematics at the bright end of the sample; adding 1 per cent systematic uncertainty to the flux measurements removes this correlation (gray points in panel d).

The agreement presented in Figure 23 varies from line to line; in Figure 24, as an example, we show H β . Here the DR3 fluxes are 4 per cent higher, with the discrepancy correlating with flux and decreasing with redshift, as expected from the continuum correction applied by PPXF.

A similar result is found for the medium-resolution gratings, where again we find excellent agreement in the overall flux (within 1 per cent), but smaller uncertainties (by 16 per cent).

C. FIELD DEPENDENCE OF THE PRISM WAVELENGTH CALIBRATION BIAS

In this appendix, we show that the bias in the wavelength calibration of the prism spectra has a residual dependence on the source position within the MSA. We calculate Δv for each galaxy (with the same definitions and cuts as in Section 9), then average Δv inside each of the four MSA quadrants. This reveals a bias only in quadrant 2 (hereafter: Q2), with a 4- σ detection. We then use the best-fit linear relation of Figure 13 to remove the wavelength bias trend with δx , and repeat the test. The results are shown in Figure 26; there is a clearly detected zero-point offset in $\langle \Delta v \rangle$, as expected from Figure 13. The offset is smallest in Q3 (2.5- σ significance) and highest in Q2 (8 σ), with intermediate values in Q1 and Q4 (3- to 4- σ significance). The diagonal direction from Q3 to Q2 is also the direction where the

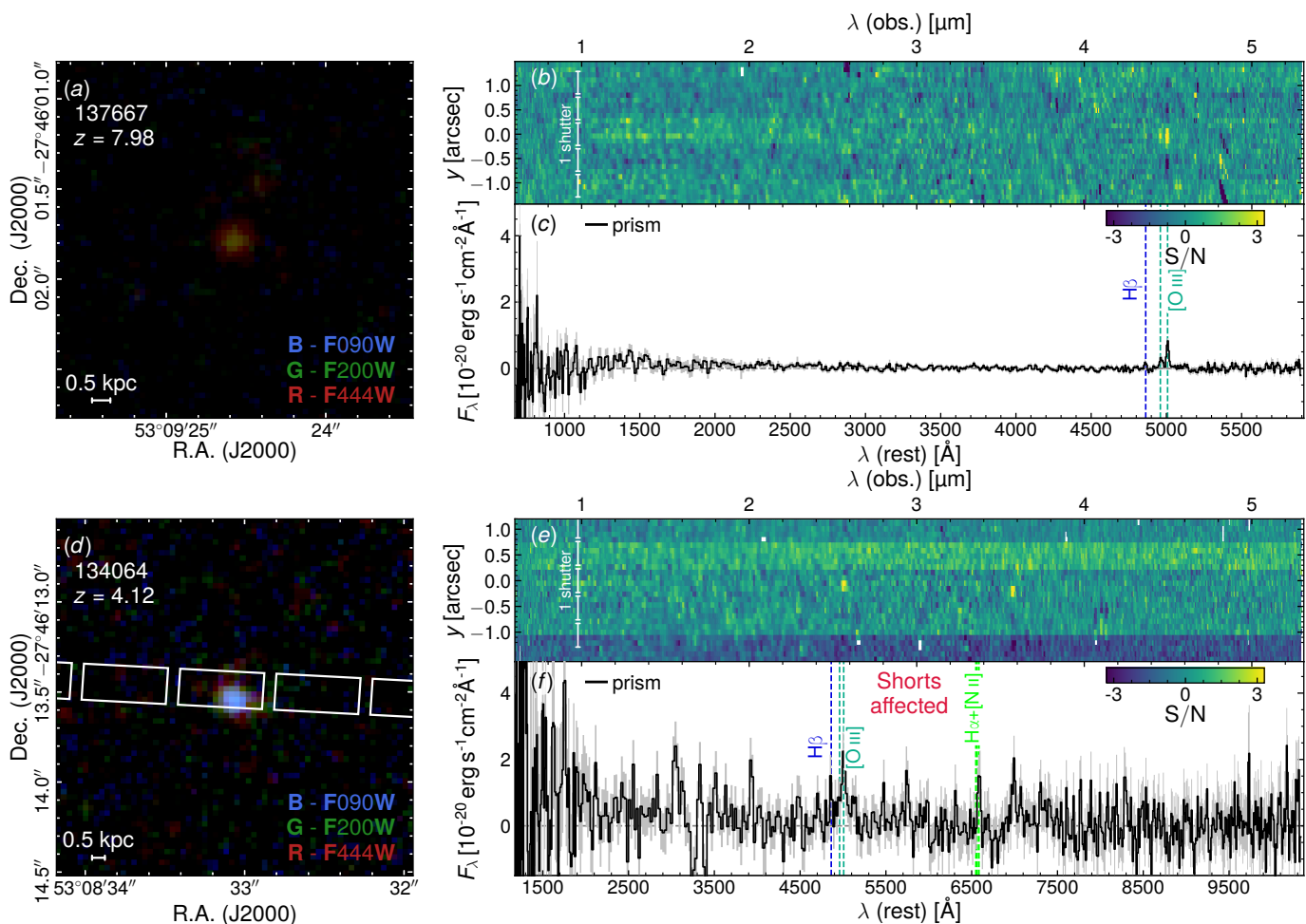


Figure 22. A selection of targets from program 1180, comparing a successful observation (panels a–c) and an observation affected by ‘shorts’ (panels d–l). The successful observation shows the expected signal-to-noise both in the 2-d map (panel b) and in the extracted 1-d spectrum (panel c). In contrast, panels (e), (h) and (k) show clear problems. Panel (e) shows different background levels between different integrations (captured at different nod positions, resulting in horizontal striping). Panels (h) and (k) have similar background to panel (b), but the shorts affect the data reduction pipeline in other ways. For 148429, the shorts are likely responsible for the excess of outliers in the region 1–2 μm; nevertheless, the data can still be used to measure the galaxy redshift. For 212327 (whose redshift is known from the medium-resolution grating), the shorts caused a mis-alignment of the already extended source; the resulting data is unusable.

field-dependent spectral resolution increases, suggesting that the observed bias could be due to insufficient correction of the wavelength bias due to intra-shutter source position.

REFERENCES

- Abazajian, K. N., Adelman-McCarthy, J. K., Agüeros, M. A., et al. 2009, *ApJS*, 182, 543, doi: [10.1088/0067-0049/182/2/543](https://doi.org/10.1088/0067-0049/182/2/543)
- Alexander, D. M., Bauer, F. E., Brandt, W. N., et al. 2003, *AJ*, 126, 539, doi: [10.1086/376473](https://doi.org/10.1086/376473)
- Alves de Oliveira, C., Birkmann, S. M., Böker, T., et al. 2018, in *Society of Photo-Optical Instrumentation Engineers (SPIE) Conference Series*, Vol. 10704, *Observatory Operations: Strategies, Processes, and Systems VII*, 107040Q, doi: [10.1117/12.2313839](https://doi.org/10.1117/12.2313839)
- Arrabal Haro, P., Dickinson, M., Finkelstein, S. L., et al. 2023, *ApJL*, 951, L22, doi: [10.3847/2041-8213/acdd54](https://doi.org/10.3847/2041-8213/acdd54)
- Ashby, M. L. N., Willner, S. P., Fazio, G. G., et al. 2013, *ApJ*, 769, 80, doi: [10.1088/0004-637X/769/1/80](https://doi.org/10.1088/0004-637X/769/1/80)

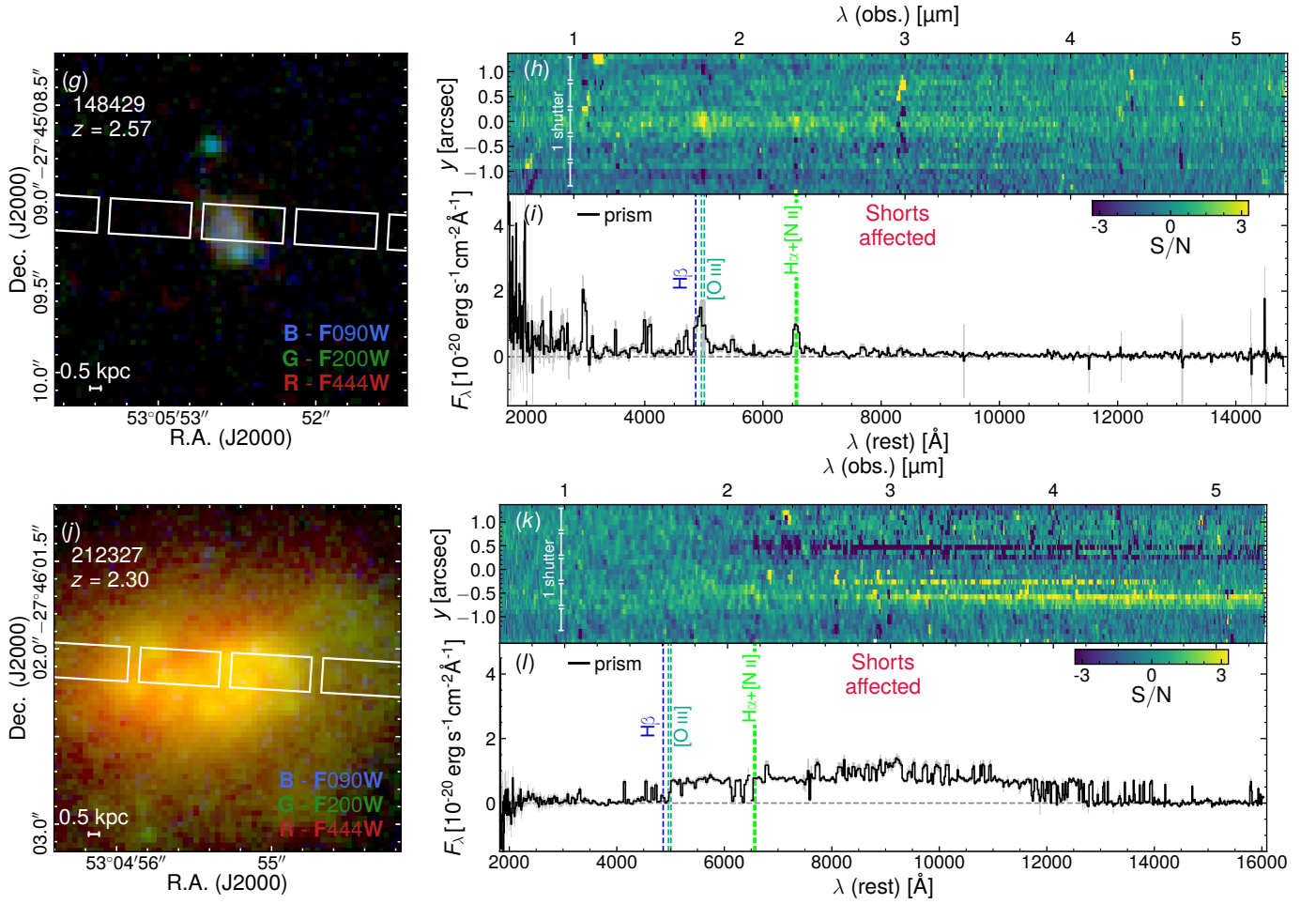


Figure 22. (continued).

Astropy Collaboration, Robitaille, T. P., Tollerud, E. J., et al. 2013, *A&A*, 558, A33, doi: [10.1051/0004-6361/201322068](https://doi.org/10.1051/0004-6361/201322068)

Baker, W. M., Maiolino, R., Bluck, A. F. L., et al. 2022, *MNRAS*, 510, 3622, doi: [10.1093/mnras/stab3672](https://doi.org/10.1093/mnras/stab3672)

Barger, A. J., Cowie, L. L., & Wang, W. H. 2008, *ApJ*, 689, 687, doi: [10.1086/592735](https://doi.org/10.1086/592735)

Barro, G., Pérez-González, P. G., Cava, A., et al. 2019, *ApJS*, 243, 22, doi: [10.3847/1538-4365/ab23f2](https://doi.org/10.3847/1538-4365/ab23f2)

Barsanti, S., Colless, M., D'Eugenio, F., et al. 2023, *MNRAS*, 526, 1613, doi: [10.1093/mnras/stad2728](https://doi.org/10.1093/mnras/stad2728)

Belli, S., Park, M., Davies, R. L., et al. 2023, arXiv e-prints, arXiv:2308.05795, doi: [10.48550/arXiv.2308.05795](https://doi.org/10.48550/arXiv.2308.05795)

Bezanson, R., Labbe, I., Whitaker, K. E., et al. 2022, arXiv e-prints, arXiv:2212.04026, doi: [10.48550/arXiv.2212.04026](https://doi.org/10.48550/arXiv.2212.04026)

Bluck, A. F. L., Maiolino, R., Brownson, S., et al. 2022, *A&A*, 659, A160, doi: [10.1051/0004-6361/202142643](https://doi.org/10.1051/0004-6361/202142643)

Bonaventura, N., Jakobsen, P., Ferruit, P., Arribas, S., & Giardino, G. 2023, *A&A*, 672, A40, doi: [10.1051/0004-6361/202245403](https://doi.org/10.1051/0004-6361/202245403)

Bouwens, R. J., Illingworth, G. D., Oesch, P. A., et al. 2015, *ApJ*, 803, 34, doi: [10.1088/0004-637X/803/1/34](https://doi.org/10.1088/0004-637X/803/1/34)

Bouwens, R. J., Oesch, P. A., Stefanon, M., et al. 2021, *AJ*, 162, 47, doi: [10.3847/1538-3881/abf83e](https://doi.org/10.3847/1538-3881/abf83e)

Brammer, G. 2023, doi: [10.5281/zenodo.7963066](https://doi.org/10.5281/zenodo.7963066)

Brammer, G. B., van Dokkum, P. G., & Coppi, P. 2008, *ApJ*, 686, 1503, doi: [10.1086/591786](https://doi.org/10.1086/591786)

Bunker, A. J., Stanway, E. R., Ellis, R. S., & McMahon, R. G. 2004, *MNRAS*, 355, 374, doi: [10.1111/j.1365-2966.2004.08326.x](https://doi.org/10.1111/j.1365-2966.2004.08326.x)

Bunker, A. J., Saxena, A., Cameron, A. J., et al. 2023a, *A&A*, 677, A88, doi: [10.1051/0004-6361/202346159](https://doi.org/10.1051/0004-6361/202346159)

Bunker, A. J., Cameron, A. J., Curtis-Lake, E., et al. 2023b, arXiv e-prints, arXiv:2306.02467, doi: [10.48550/arXiv.2306.02467](https://doi.org/10.48550/arXiv.2306.02467)

Caldwell, J. A. R., McIntosh, D. H., Rix, H.-W., et al. 2008, *ApJS*, 174, 136, doi: [10.1086/521080](https://doi.org/10.1086/521080)

Cameron, A. J., Katz, H., Witten, C., et al. 2023, arXiv e-prints, arXiv:2311.02051, doi: [10.48550/arXiv.2311.02051](https://doi.org/10.48550/arXiv.2311.02051)

All prism lines

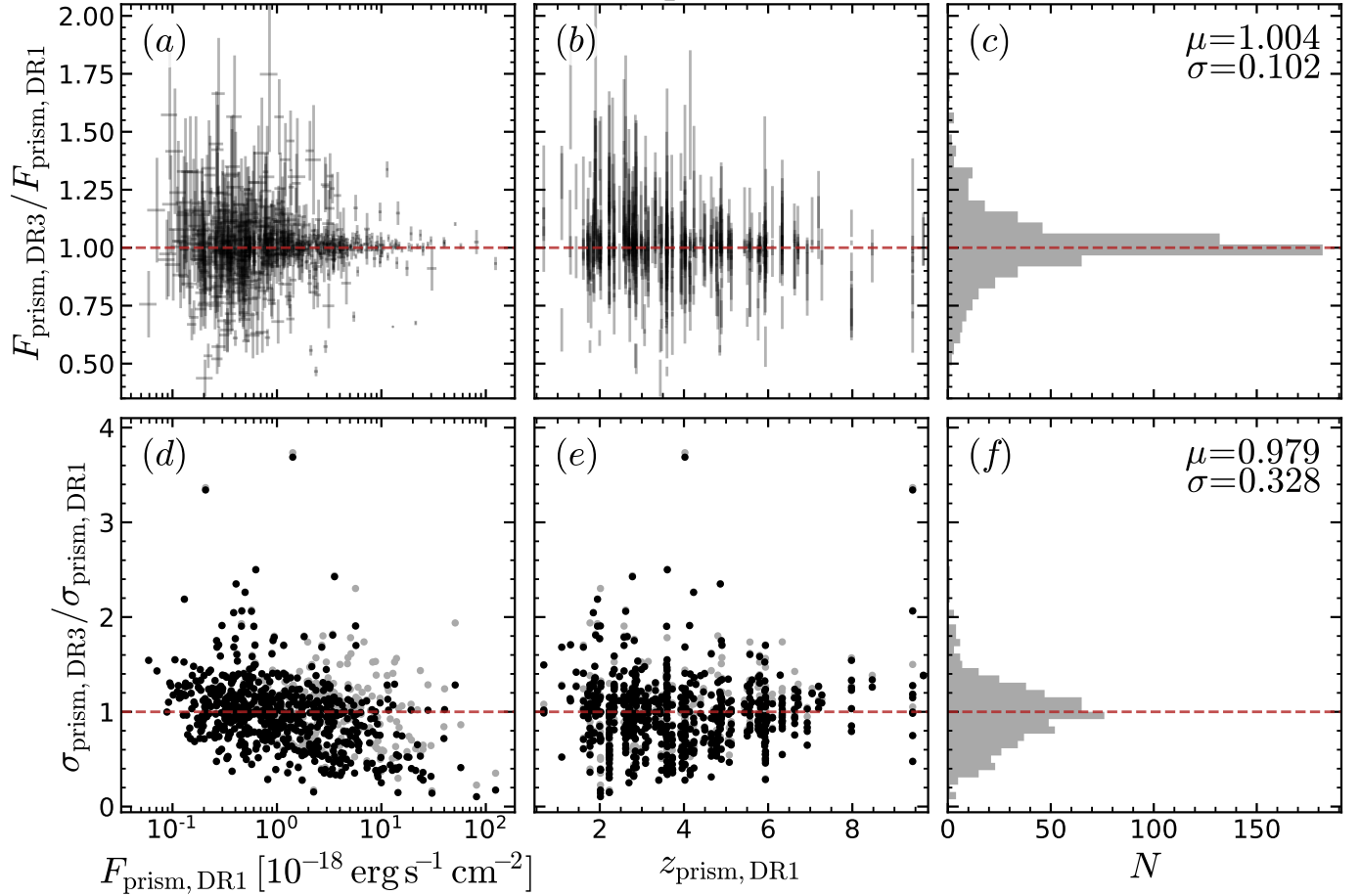


Figure 23. Comparison of the prism emission-line fluxes and their uncertainties between DR1 and DR3; the top row compares the fluxes, the bottom row compares the uncertainties. We find a statistically significant correlation between the ratio of uncertainties and flux (panel d), indicating that our PPXF implementation tends to underestimate the line noise in the high-S/N regime, relative to DR1. The gray points in the bottom panel illustrate the effect of adding 1 per cent relative uncertainties to the DR3 flux measurements.

Capak, P., Cowie, L. L., Hu, E. M., et al. 2004, *AJ*, 127, 180, doi: [10.1086/380611](https://doi.org/10.1086/380611)

Cappellari, M. 2017, *MNRAS*, 466, 798, doi: [10.1093/mnras/stw3020](https://doi.org/10.1093/mnras/stw3020)

—. 2023, *MNRAS*, 526, 3273, doi: [10.1093/mnras/stad2597](https://doi.org/10.1093/mnras/stad2597)

Cappellari, M., Scott, N., Alatalo, K., et al. 2013, *MNRAS*, 432, 1709, doi: [10.1093/mnras/stt562](https://doi.org/10.1093/mnras/stt562)

Carnall, A. C., McLure, R. J., Dunlop, J. S., et al. 2019, *MNRAS*, 490, 417, doi: [10.1093/mnras/stz2544](https://doi.org/10.1093/mnras/stz2544)

—. 2023, *Nature*, 619, 716, doi: [10.1038/s41586-023-06158-6](https://doi.org/10.1038/s41586-023-06158-6)

Chapin, E. L., Pope, A., Scott, D., et al. 2009, *MNRAS*, 398, 1793, doi: [10.1111/j.1365-2966.2009.15267.x](https://doi.org/10.1111/j.1365-2966.2009.15267.x)

Choi, J., Dotter, A., Conroy, C., et al. 2016, *ApJ*, 823, 102, doi: [10.3847/0004-637X/823/2/102](https://doi.org/10.3847/0004-637X/823/2/102)

Circosta, C., Vignali, C., Gilli, R., et al. 2019, *A&A*, 623, A172, doi: [10.1051/0004-6361/201834426](https://doi.org/10.1051/0004-6361/201834426)

Coe, D., Benítez, N., Sánchez, S. F., et al. 2006, *AJ*, 132, 926, doi: [10.1086/505530](https://doi.org/10.1086/505530)

Conroy, C., & Gunn, J. E. 2010, *FSPS: Flexible Stellar Population Synthesis*, Astrophysics Source Code Library, record ascl:1010.043. <http://ascl.net/1010.043>

Conroy, C., Gunn, J. E., & White, M. 2009, *ApJ*, 699, 486, doi: [10.1088/0004-637X/699/1/486](https://doi.org/10.1088/0004-637X/699/1/486)

Conroy, C., Naidu, R. P., Zaritsky, D., et al. 2019, *ApJ*, 887, 237, doi: [10.3847/1538-4357/ab5710](https://doi.org/10.3847/1538-4357/ab5710)

Cowie, L. L., Barger, A. J., Hsu, L. Y., et al. 2017, *ApJ*, 837, 139, doi: [10.3847/1538-4357/aa60bb](https://doi.org/10.3847/1538-4357/aa60bb)

Curti, M., D’Eugenio, F., Carniani, S., et al. 2023a, *MNRAS*, 518, 425, doi: [10.1093/mnras/stac2737](https://doi.org/10.1093/mnras/stac2737)

Curti, M., Maiolino, R., Curtis-Lake, E., et al. 2023b, *arXiv e-prints*, arXiv:2304.08516, doi: [10.48550/arXiv.2304.08516](https://doi.org/10.48550/arXiv.2304.08516)

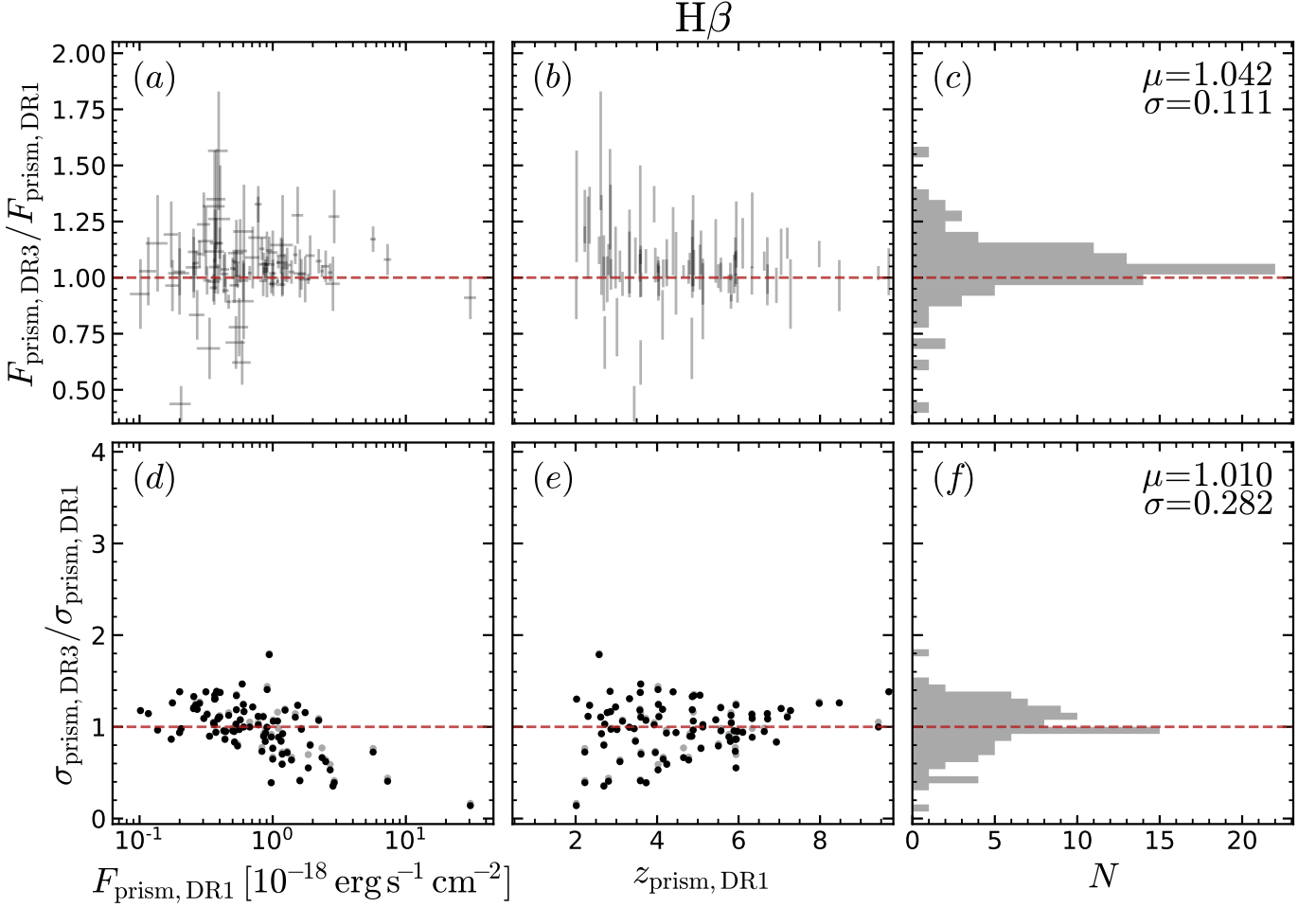


Figure 24. Comparison of the $H\beta$ flux measured from the prism between DR1 and DR3; the symbols are the same as in Figure 23. Below redshift $z = 2$, $H\beta$ is blended with $[O\text{III}]\lambda\lambda 4959,5007$ and is not reported in this figure. The $H\beta$ flux ratio between DR3 and DR1 is 1.04, while for all emission lines the ratio is 1.003.

Curtis-Lake, E., Carniani, S., Cameron, A., et al. 2023, Nature Astronomy, 7, 622,

doi: [10.1038/s41550-023-01918-w](https://doi.org/10.1038/s41550-023-01918-w)

Dalton, G., Trager, S. C., Abrams, D. C., et al. 2012, in Society of Photo-Optical Instrumentation Engineers (SPIE) Conference Series, Vol. 8446, Ground-based and Airborne Instrumentation for Astronomy IV, ed. I. S. McLean, S. K. Ramsay, & H. Takami, 84460P,

doi: [10.1117/12.925950](https://doi.org/10.1117/12.925950)

Davies, R. L., Belli, S., Park, M., et al. 2024, MNRAS, 528, 4976, doi: [10.1093/mnras/stae327](https://doi.org/10.1093/mnras/stae327)

de Jong, R. S., Agertz, O., Berbel, A. A., et al. 2019, The Messenger, 175, 3, doi: [10.18727/0722-6691/5117](https://doi.org/10.18727/0722-6691/5117)

DESI Collaboration, Aghamousa, A., Aguilar, J., et al. 2016, arXiv e-prints, arXiv:1611.00036.

<https://arxiv.org/abs/1611.00036>

D'Eugenio, F., van der Wel, A., Wu, P.-F., et al. 2020, MNRAS, 497, 389, doi: [10.1093/mnras/staa1937](https://doi.org/10.1093/mnras/staa1937)

D'Eugenio, F., Perez-Gonzalez, P., Maiolino, R., et al. 2023a, arXiv e-prints, arXiv:2308.06317,

doi: [10.48550/arXiv.2308.06317](https://doi.org/10.48550/arXiv.2308.06317)

D'Eugenio, F., Maiolino, R., Carniani, S., et al. 2023b, arXiv e-prints, arXiv:2311.09908,

doi: [10.48550/arXiv.2311.09908](https://doi.org/10.48550/arXiv.2311.09908)

Dorner, B. 2012, Theses, Université Claude Bernard - Lyon I. <https://theses.hal.science/tel-00738070>

Driver, S. P., Andrews, S. K., da Cunha, E., et al. 2018, MNRAS, 475, 2891, doi: [10.1093/mnras/stx2728](https://doi.org/10.1093/mnras/stx2728)

Eisenstein, D. J., Willott, C., Albers, S., et al. 2023a, arXiv e-prints, arXiv:2306.02465,

doi: [10.48550/arXiv.2306.02465](https://doi.org/10.48550/arXiv.2306.02465)

Eisenstein, D. J., Johnson, B. D., Robertson, B., et al. 2023b, arXiv e-prints, arXiv:2310.12340,

doi: [10.48550/arXiv.2310.12340](https://doi.org/10.48550/arXiv.2310.12340)

Eisenstein, D. J., Willott, C., Albers, S., et al. 2023c, arXiv e-prints, arXiv:2306.02465,

doi: [10.48550/arXiv.2306.02465](https://doi.org/10.48550/arXiv.2306.02465)

All medium-gratings lines

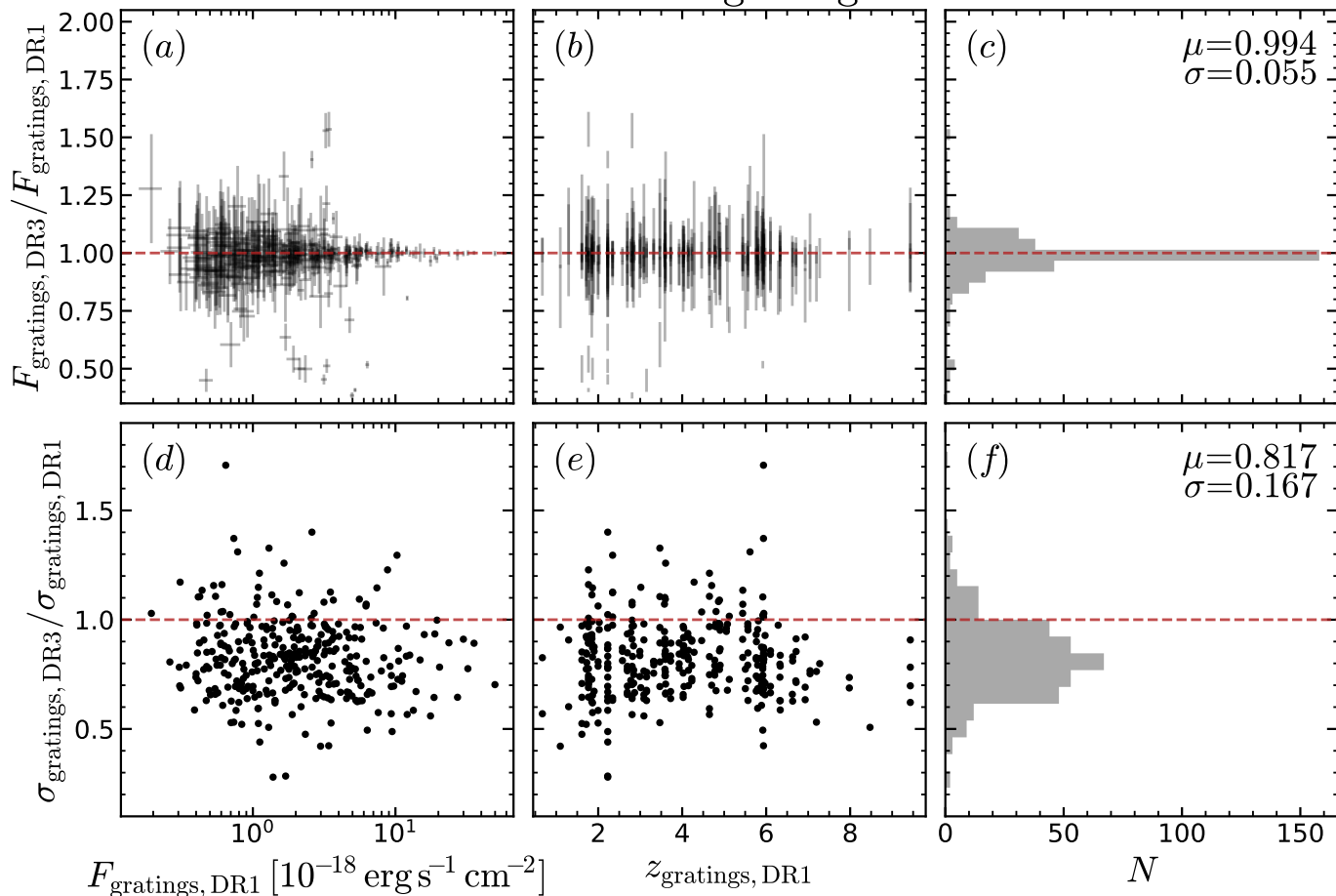


Figure 25. Comparison of the medium-resolution emission-line fluxes and their uncertainties between DR1 and DR3; the top row compares the fluxes, the bottom row compares the uncertainties. Fluxes are in excellent agreement, while we find the uncertainties to be smaller by 20 per cent, on average.

Ellis, R. S., McLure, R. J., Dunlop, J. S., et al. 2013, *ApJL*,

763, L7, doi: [10.1088/2041-8205/763/1/L7](https://doi.org/10.1088/2041-8205/763/1/L7)

Endsley, R., Stark, D. P., Whitler, L., et al. 2023, arXiv e-prints, arXiv:2306.05295,

doi: [10.48550/arXiv.2306.05295](https://doi.org/10.48550/arXiv.2306.05295)

Ferruit, P., Jakobsen, P., Giardino, G., et al. 2022, *A&A*, 661, A81, doi: [10.1051/0004-6361/202142673](https://doi.org/10.1051/0004-6361/202142673)

Finkelstein, S. L., Ryan, Russell E., J., Papovich, C., et al. 2015, *ApJ*, 810, 71, doi: [10.1088/0004-637X/810/1/71](https://doi.org/10.1088/0004-637X/810/1/71)

Foreman-Mackey, D. 2016, *The Journal of Open Source Software*, 1, 24, doi: [10.21105/joss.00024](https://doi.org/10.21105/joss.00024)

Foreman-Mackey, D., Hogg, D. W., Lang, D., & Goodman, J. 2013, *PASP*, 125, 306, doi: [10.1086/670067](https://doi.org/10.1086/670067)

Fujimoto, S., Arrabal Haro, P., Dickinson, M., et al. 2023, *ApJL*, 949, L25, doi: [10.3847/2041-8213/acd2d9](https://doi.org/10.3847/2041-8213/acd2d9)

Garilli, B., Le Fèvre, O., Guzzo, L., et al. 2008, *A&A*, 486, 683, doi: [10.1051/0004-6361:20078878](https://doi.org/10.1051/0004-6361:20078878)

Giavalisco, M., Ferguson, H. C., Koekemoer, A. M., et al. 2004, *ApJL*, 600, L93, doi: [10.1086/379232](https://doi.org/10.1086/379232)

Glazebrook, K., Nanayakkara, T., Schreiber, C., et al. 2023, arXiv e-prints, arXiv:2308.05606,

doi: [10.48550/arXiv.2308.05606](https://doi.org/10.48550/arXiv.2308.05606)

Goulding, A. D., Greene, J. E., Setton, D. J., et al. 2023, *ApJL*, 955, L24, doi: [10.3847/2041-8213/acf7c5](https://doi.org/10.3847/2041-8213/acf7c5)

Graves, G. J., & Faber, S. M. 2010, *ApJ*, 717, 803, doi: [10.1088/0004-637X/717/2/803](https://doi.org/10.1088/0004-637X/717/2/803)

Grogin, N. A., Kocevski, D. D., Faber, S. M., et al. 2011, *ApJS*, 197, 35, doi: [10.1088/0067-0049/197/2/35](https://doi.org/10.1088/0067-0049/197/2/35)

Guo, Y., Ferguson, H. C., Giavalisco, M., et al. 2013, *ApJS*, 207, 24, doi: [10.1088/0067-0049/207/2/24](https://doi.org/10.1088/0067-0049/207/2/24)

Hainline, K. N., Johnson, B. D., Robertson, B., et al. 2023, arXiv e-prints, arXiv:2306.02468,

doi: [10.48550/arXiv.2306.02468](https://doi.org/10.48550/arXiv.2306.02468)

Hainline, K. N., D'Eugenio, F., Jakobsen, P., et al. 2024, arXiv e-prints, arXiv:2404.04325.

<https://arxiv.org/abs/2404.04325>

Harikane, Y., Ouchi, M., Ono, Y., et al. 2016, *ApJ*, 821, 123, doi: [10.3847/0004-637X/821/2/123](https://doi.org/10.3847/0004-637X/821/2/123)

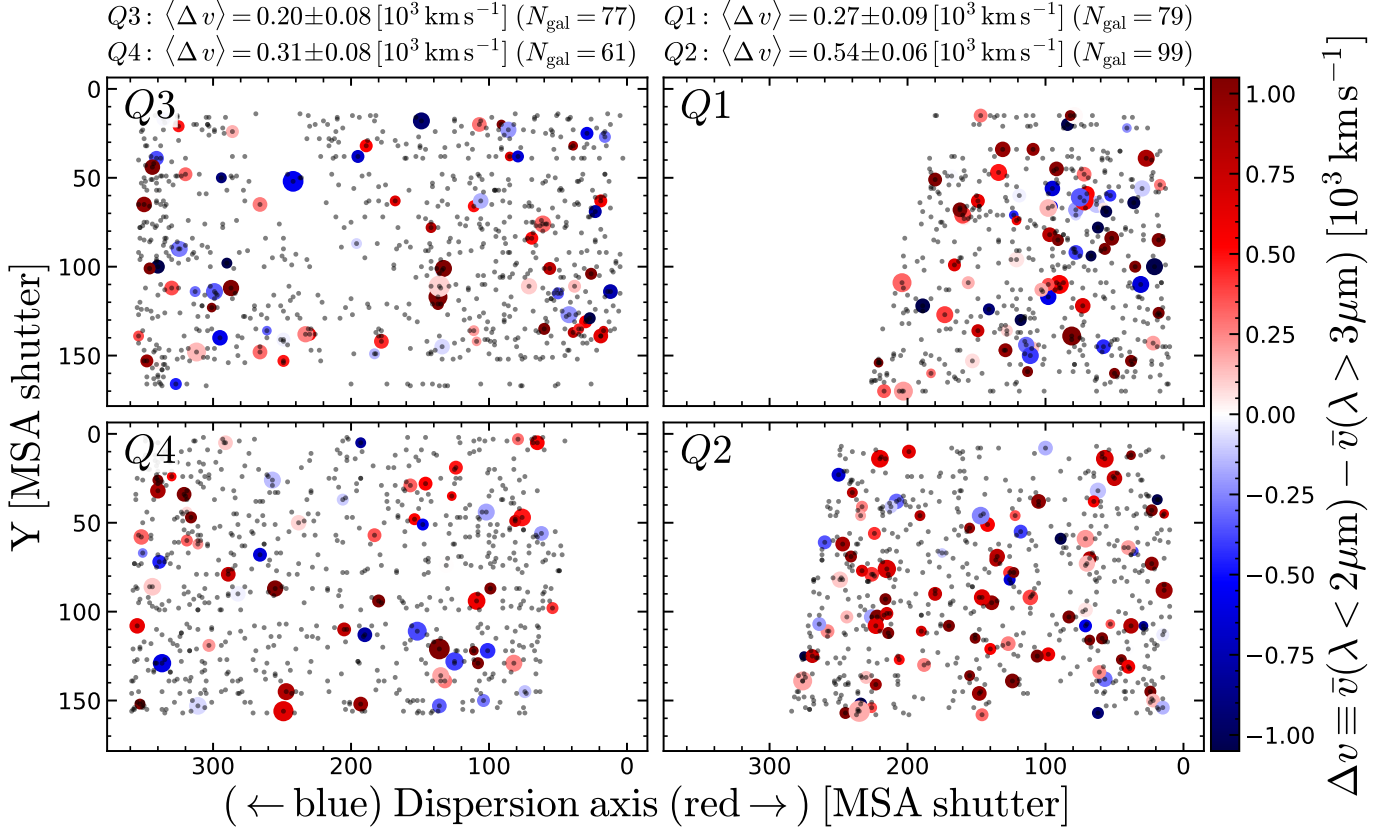


Figure 26. Wavelength solution bias Δv as a function of location on the MSA; the four rectangles are the four MSA quadrants Q1–Q4, with the location of the sample galaxies marked by small gray dots. The large dots represent galaxies with more than four emission lines detected at $S/N > 5$, for which we could calculate the velocity offset between lines observed at wavelengths $1 - 2 \mu\text{m}$ and lines observed at $3 - 5.3 \mu\text{m}$. Δv has been corrected empirically for residual intra-shutter wavelength bias (Section 9). $\langle \Delta v \rangle$ is the average of Δv inside each of the quadrants, illustrating a trend of increasing bias diagonally from Q3 to Q2.

Harris, C. R., Millman, K. J., van der Walt, S. J., et al. 2020, *Nature*, 585, 357, doi: [10.1038/s41586-020-2649-2](https://doi.org/10.1038/s41586-020-2649-2)

Hausen, R., & Robertson, B. E. 2022, *Astronomy and Computing*, 39, 100586, doi: [10.1016/j.ascom.2022.100586](https://doi.org/10.1016/j.ascom.2022.100586)

Heintz, K. E., De Cia, A., Thöne, C. C., et al. 2023, arXiv e-prints, arXiv:2308.14812, doi: [10.48550/arXiv.2308.14812](https://doi.org/10.48550/arXiv.2308.14812)

Herenz, E. C., Urrutia, T., Wisotzki, L., et al. 2017, *A&A*, 606, A12, doi: [10.1051/0004-6361/201731055](https://doi.org/10.1051/0004-6361/201731055)

Hunter, J. D. 2007, *Computing in Science and Engineering*, 9, 90, doi: [10.1109/MCSE.2007.55](https://doi.org/10.1109/MCSE.2007.55)

Inami, H., Bacon, R., Brinchmann, J., et al. 2017, *A&A*, 608, A2, doi: [10.1051/0004-6361/201731195](https://doi.org/10.1051/0004-6361/201731195)

Jakobsen, P., Ferruit, P., Alves de Oliveira, C., et al. 2022, *A&A*, 661, A80, doi: [10.1051/0004-6361/202142663](https://doi.org/10.1051/0004-6361/202142663)

Ji, Z., Williams, C. C., Tacchella, S., et al. 2023, arXiv e-prints, arXiv:2305.18518, doi: [10.48550/arXiv.2305.18518](https://doi.org/10.48550/arXiv.2305.18518)

Jones, E., Oliphant, T., Peterson, P., et al. 2001, *SciPy: Open source scientific tools for Python*. <http://www.scipy.org/>

Joye, W. A., & Mandel, E. 2003, in *Astronomical Society of the Pacific Conference Series*, Vol. 295, *Astronomical Data Analysis Software and Systems XII*, ed. H. E. Payne, R. I. Jedrzejewski, & R. N. Hook, 489

Kauffmann, G., Heckman, T. M., White, S. D. M., et al. 2003a, *MNRAS*, 341, 33, doi: [10.1046/j.1365-8711.2003.06291.x](https://doi.org/10.1046/j.1365-8711.2003.06291.x)

—. 2003b, *MNRAS*, 341, 54, doi: [10.1046/j.1365-8711.2003.06292.x](https://doi.org/10.1046/j.1365-8711.2003.06292.x)

Kocevski, D. D., Onoue, M., Inayoshi, K., et al. 2023, *ApJL*, 954, L4, doi: [10.3847/2041-8213/ace5a0](https://doi.org/10.3847/2041-8213/ace5a0)

Koekemoer, A. M., Faber, S. M., Ferguson, H. C., et al. 2011, *ApJS*, 197, 36, doi: [10.1088/0067-0049/197/2/36](https://doi.org/10.1088/0067-0049/197/2/36)

Kokorev, V., Brammer, G., Fujimoto, S., et al. 2022, *ApJS*, 263, 38, doi: [10.3847/1538-4365/ac9909](https://doi.org/10.3847/1538-4365/ac9909)

Kriek, M., Shapley, A. E., Reddy, N. A., et al. 2015, *ApJS*, 218, 15, doi: [10.1088/0067-0049/218/2/15](https://doi.org/10.1088/0067-0049/218/2/15)

Kurk, J., Cimatti, A., Daddi, E., et al. 2013, *A&A*, 549, A63, doi: [10.1051/0004-6361/201117847](https://doi.org/10.1051/0004-6361/201117847)

- Leja, J., Carnall, A. C., Johnson, B. D., Conroy, C., & Speagle, J. S. 2019, *ApJ*, 876, 3, doi: [10.3847/1538-4357/ab133c](https://doi.org/10.3847/1538-4357/ab133c)
- Li, J. 2023, *AstroJacobLi/smplotlib: v0.0.8, v0.0.8*, Zenodo, doi: [10.5281/zenodo.7966831](https://doi.org/10.5281/zenodo.7966831)
- Looser, T. J., D'Eugenio, F., Maiolino, R., et al. 2023a, arXiv e-prints, arXiv:2302.14155, doi: [10.48550/arXiv.2302.14155](https://doi.org/10.48550/arXiv.2302.14155)
- . 2023b, arXiv e-prints, arXiv:2306.02470, doi: [10.48550/arXiv.2306.02470](https://doi.org/10.48550/arXiv.2306.02470)
- Lorenzoni, S., Bunker, A. J., Wilkins, S. M., et al. 2013, *MNRAS*, 429, 150, doi: [10.1093/mnras/sts325](https://doi.org/10.1093/mnras/sts325)
- . 2011, *MNRAS*, 414, 1455, doi: [10.1111/j.1365-2966.2011.18479.x](https://doi.org/10.1111/j.1365-2966.2011.18479.x)
- Luo, B., Brandt, W. N., Xue, Y. Q., et al. 2017, *ApJS*, 228, 2, doi: [10.3847/1538-4365/228/1/2](https://doi.org/10.3847/1538-4365/228/1/2)
- Magnelli, B., Popesso, P., Berta, S., et al. 2013, *A&A*, 553, A132, doi: [10.1051/0004-6361/201321371](https://doi.org/10.1051/0004-6361/201321371)
- Maiolino, R., Cirasuolo, M., Afonso, J., et al. 2020, *The Messenger*, 180, 24, doi: [10.18727/0722-6691/5197](https://doi.org/10.18727/0722-6691/5197)
- Maiolino, R., Scholtz, J., Witstok, J., et al. 2023a, arXiv e-prints, arXiv:2305.12492, doi: [10.48550/arXiv.2305.12492](https://doi.org/10.48550/arXiv.2305.12492)
- Maiolino, R., Uebler, H., Perna, M., et al. 2023b, arXiv e-prints, arXiv:2306.00953, doi: [10.48550/arXiv.2306.00953](https://doi.org/10.48550/arXiv.2306.00953)
- Maseda, M. V., van der Wel, A., Rix, H.-W., et al. 2018, *ApJ*, 854, 29, doi: [10.3847/1538-4357/aaa76e](https://doi.org/10.3847/1538-4357/aaa76e)
- Maseda, M. V., de Graaff, A., Franx, M., et al. 2024, arXiv e-prints, arXiv:2403.05506, doi: [10.48550/arXiv.2403.05506](https://doi.org/10.48550/arXiv.2403.05506)
- McLure, R. J., Dunlop, J. S., Bowler, R. A. A., et al. 2013, *MNRAS*, 432, 2696, doi: [10.1093/mnras/stt627](https://doi.org/10.1093/mnras/stt627)
- Momcheva, I. G., Brammer, G. B., van Dokkum, P. G., et al. 2016, *ApJS*, 225, 27, doi: [10.3847/0067-0049/225/2/27](https://doi.org/10.3847/0067-0049/225/2/27)
- Morris, A. M., Kocevski, D. D., Trump, J. R., et al. 2015, *AJ*, 149, 178, doi: [10.1088/0004-6256/149/6/178](https://doi.org/10.1088/0004-6256/149/6/178)
- Morrison, G. E., Owen, F. N., Dickinson, M., Ivison, R. J., & Ibar, E. 2010, *ApJS*, 188, 178, doi: [10.1088/0067-0049/188/1/178](https://doi.org/10.1088/0067-0049/188/1/178)
- Mullaney, J. R., Pannella, M., Daddi, E., et al. 2012, *MNRAS*, 419, 95, doi: [10.1111/j.1365-2966.2011.19675.x](https://doi.org/10.1111/j.1365-2966.2011.19675.x)
- Murphy, E. J., Momjian, E., Condon, J. J., et al. 2017, *ApJ*, 839, 35, doi: [10.3847/1538-4357/aa62fd](https://doi.org/10.3847/1538-4357/aa62fd)
- Nakajima, K., Ouchi, M., Isobe, Y., et al. 2023, arXiv e-prints, arXiv:2301.12825, doi: [10.48550/arXiv.2301.12825](https://doi.org/10.48550/arXiv.2301.12825)
- Nanayakkara, T., Glazebrook, K., Jacobs, C., et al. 2022, arXiv e-prints, arXiv:2212.11638, <https://arxiv.org/abs/2212.11638>
- Newman, J. A., Cooper, M. C., Davis, M., et al. 2013, *ApJS*, 208, 5, doi: [10.1088/0067-0049/208/1/5](https://doi.org/10.1088/0067-0049/208/1/5)
- Oesch, P. A., Bouwens, R. J., Illingworth, G. D., et al. 2010, *ApJL*, 709, L16, doi: [10.1088/2041-8205/709/1/L16](https://doi.org/10.1088/2041-8205/709/1/L16)
- . 2013, *ApJ*, 773, 75, doi: [10.1088/0004-637X/773/1/75](https://doi.org/10.1088/0004-637X/773/1/75)
- . 2014, *ApJ*, 786, 108, doi: [10.1088/0004-637X/786/2/108](https://doi.org/10.1088/0004-637X/786/2/108)
- Oesch, P. A., Brammer, G., van Dokkum, P. G., et al. 2016, *ApJ*, 819, 129, doi: [10.3847/0004-637X/819/2/129](https://doi.org/10.3847/0004-637X/819/2/129)
- Oesch, P. A., Brammer, G., Naidu, R. P., et al. 2023a, *MNRAS*, 525, 2864, doi: [10.1093/mnras/stad2411](https://doi.org/10.1093/mnras/stad2411)
- . 2023b, *MNRAS*, 525, 2864, doi: [10.1093/mnras/stad2411](https://doi.org/10.1093/mnras/stad2411)
- Oke, J. B., & Gunn, J. E. 1983, *ApJ*, 266, 713, doi: [10.1086/160817](https://doi.org/10.1086/160817)
- Peng, Y.-j., Lilly, S. J., Kovač, K., et al. 2010, *ApJ*, 721, 193, doi: [10.1088/0004-637X/721/1/193](https://doi.org/10.1088/0004-637X/721/1/193)
- Pentericci, L., McLure, R. J., Garilli, B., et al. 2018a, *A&A*, 616, A174, doi: [10.1051/0004-6361/201833047](https://doi.org/10.1051/0004-6361/201833047)
- Pentericci, L., Vanzella, E., Castellano, M., et al. 2018b, *A&A*, 619, A147, doi: [10.1051/0004-6361/201732465](https://doi.org/10.1051/0004-6361/201732465)
- Rafelski, M., Teplitz, H. I., Gardner, J. P., et al. 2015, *AJ*, 150, 31, doi: [10.1088/0004-6256/150/1/31](https://doi.org/10.1088/0004-6256/150/1/31)
- Rawle, T. D., Giardino, G., Franz, D. E., et al. 2022, in *Society of Photo-Optical Instrumentation Engineers (SPIE) Conference Series*, Vol. 12180, *Space Telescopes and Instrumentation 2022: Optical, Infrared, and Millimeter Wave*, ed. L. E. Coyle, S. Matsuura, & M. D. Perrin, 121803R, doi: [10.1117/12.2629231](https://doi.org/10.1117/12.2629231)
- Reddy, N. A., Steidel, C. C., Erb, D. K., Shapley, A. E., & Pettini, M. 2006, *ApJ*, 653, 1004, doi: [10.1086/508851](https://doi.org/10.1086/508851)
- Rieke, M., Robertson, B., Tacchella, S., et al. 2023a, arXiv e-prints, arXiv:2306.02466, doi: [10.48550/arXiv.2306.02466](https://doi.org/10.48550/arXiv.2306.02466)
- . 2023b, arXiv e-prints, arXiv:2306.02466, doi: [10.48550/arXiv.2306.02466](https://doi.org/10.48550/arXiv.2306.02466)
- Robertson, B., Johnson, B. D., Tacchella, S., et al. 2023a, arXiv e-prints, arXiv:2312.10033, doi: [10.48550/arXiv.2312.10033](https://doi.org/10.48550/arXiv.2312.10033)
- Robertson, B. E., Tacchella, S., Johnson, B. D., et al. 2023b, *Nature Astronomy*, 7, 611, doi: [10.1038/s41550-023-01921-1](https://doi.org/10.1038/s41550-023-01921-1)
- Rousseeuw, P. J., & Driessen, K. 2006, *Data Min. Knowl. Discov.*, 12, 29, doi: [10.1007/s10618-005-0024-4](https://doi.org/10.1007/s10618-005-0024-4)
- Salpeter, E. E. 1955, *ApJ*, 121, 161, doi: [10.1086/145971](https://doi.org/10.1086/145971)
- Schenker, M. A., Robertson, B. E., Ellis, R. S., et al. 2013, *ApJ*, 768, 196, doi: [10.1088/0004-637X/768/2/196](https://doi.org/10.1088/0004-637X/768/2/196)

- Shapley, A. E., Sanders, R., Berg, D., et al. 2021, The AURORA Survey: First Direct Metallicity Calibrations at High Redshift, JWST Proposal. Cycle 1, ID. #1914
- Skelton, R. E., Whitaker, K. E., Momcheva, I. G., et al. 2014, *ApJS*, 214, 24, doi: [10.1088/0067-0049/214/2/24](https://doi.org/10.1088/0067-0049/214/2/24)
- Stark, D. P., Ellis, R. S., & Ouchi, M. 2011, *ApJL*, 728, L2, doi: [10.1088/2041-8205/728/1/L2](https://doi.org/10.1088/2041-8205/728/1/L2)
- Stark, D. P., Schenker, M. A., Ellis, R., et al. 2013, *ApJ*, 763, 129, doi: [10.1088/0004-637X/763/2/129](https://doi.org/10.1088/0004-637X/763/2/129)
- Stott, J. P., Swinbank, A. M., Johnson, H. L., et al. 2016, *MNRAS*, 457, 1888, doi: [10.1093/mnras/stw129](https://doi.org/10.1093/mnras/stw129)
- Strait, V., Brammer, G., Muzzin, A., et al. 2023, *ApJL*, 949, L23, doi: [10.3847/2041-8213/acd457](https://doi.org/10.3847/2041-8213/acd457)
- Sun, F., Egami, E., Pirzkal, N., et al. 2023, *ApJ*, 953, 53, doi: [10.3847/1538-4357/acd53c](https://doi.org/10.3847/1538-4357/acd53c)
- Tamura, N., Takato, N., Shimono, A., et al. 2016, in Society of Photo-Optical Instrumentation Engineers (SPIE) Conference Series, Vol. 9908, Ground-based and Airborne Instrumentation for Astronomy VI, ed. C. J. Evans, L. Simard, & H. Takami, 99081M, doi: [10.1117/12.2232103](https://doi.org/10.1117/12.2232103)
- Tasca, L. A. M., Le Fèvre, O., Ribeiro, B., et al. 2017, *A&A*, 600, A110, doi: [10.1051/0004-6361/201527963](https://doi.org/10.1051/0004-6361/201527963)
- Taylor, M. B. 2005, in Astronomical Society of the Pacific Conference Series, Vol. 347, Astronomical Data Analysis Software and Systems XIV, ed. P. Shopbell, M. Britton, & R. Ebert, 29
- Treu, T., Ellis, R. S., Liao, T. X., & van Dokkum, P. G. 2005, *ApJL*, 622, L5, doi: [10.1086/429374](https://doi.org/10.1086/429374)
- Treu, T., Roberts-Borsani, G., Bradac, M., et al. 2022, *ApJ*, 935, 110, doi: [10.3847/1538-4357/ac8158](https://doi.org/10.3847/1538-4357/ac8158)
- U, V., Hemmati, S., Darvish, B., et al. 2015, *ApJ*, 815, 57, doi: [10.1088/0004-637X/815/1/57](https://doi.org/10.1088/0004-637X/815/1/57)
- Übler, H., Maiolino, R., Curtis-Lake, E., et al. 2023, *A&A*, 677, A145, doi: [10.1051/0004-6361/202346137](https://doi.org/10.1051/0004-6361/202346137)
- Umeda, H., Ouchi, M., Nakajima, K., et al. 2023, arXiv e-prints, arXiv:2306.00487, doi: [10.48550/arXiv.2306.00487](https://doi.org/10.48550/arXiv.2306.00487)
- Walmsley, M., Géron, T., Kruk, S., et al. 2023, *MNRAS*, 526, 4768, doi: [10.1093/mnras/stad2919](https://doi.org/10.1093/mnras/stad2919)
- Wang, B., Fujimoto, S., Labbe, I., et al. 2023, arXiv e-prints, arXiv:2308.03745, doi: [10.48550/arXiv.2308.03745](https://doi.org/10.48550/arXiv.2308.03745)
- Whitaker, K. E., Ashas, M., Illingworth, G., et al. 2019, *ApJS*, 244, 16, doi: [10.3847/1538-4365/ab3853](https://doi.org/10.3847/1538-4365/ab3853)
- Williams, R. E., Blacker, B., Dickinson, M., et al. 1996, *AJ*, 112, 1335, doi: [10.1086/118105](https://doi.org/10.1086/118105)
- Williams, R. J., Quadri, R. F., Franx, M., van Dokkum, P., & Labbé, I. 2009, *ApJ*, 691, 1879, doi: [10.1088/0004-637X/691/2/1879](https://doi.org/10.1088/0004-637X/691/2/1879)
- Wirth, G. D., Willmer, C. N. A., Amico, P., et al. 2004, *AJ*, 127, 3121, doi: [10.1086/420999](https://doi.org/10.1086/420999)
- Wisnioski, E., Förster Schreiber, N. M., Wuyts, S., et al. 2015, *ApJ*, 799, 209, doi: [10.1088/0004-637X/799/2/209](https://doi.org/10.1088/0004-637X/799/2/209)
- Wolfe, A. M., Gawiser, E., & Prochaska, J. X. 2005, *ARA&A*, 43, 861, doi: [10.1146/annurev.astro.42.053102.133950](https://doi.org/10.1146/annurev.astro.42.053102.133950)
- Wright, L., Whitaker, K. E., Weaver, J. R., et al. 2023, arXiv e-prints, arXiv:2311.05394, doi: [10.48550/arXiv.2311.05394](https://doi.org/10.48550/arXiv.2311.05394)
- Xue, Y. Q., Luo, B., Brandt, W. N., et al. 2016, The Astrophysical Journal Supplement Series, 224, 15, doi: [10.3847/0067-0049/224/2/15](https://doi.org/10.3847/0067-0049/224/2/15)
- Yan, H., & Windhorst, R. A. 2004, *ApJL*, 612, L93, doi: [10.1086/424690](https://doi.org/10.1086/424690)
- Yan, H.-J., Windhorst, R. A., Hathi, N. P., et al. 2010, *Research in Astronomy and Astrophysics*, 10, 867, doi: [10.1088/1674-4527/10/9/003](https://doi.org/10.1088/1674-4527/10/9/003)